

České vysoké učení technické v Praze
Fakulta jaderná a fyzikálně inženýrská

Katedra fyziky
Obor: Fyzika a technika termojaderné fúze



Studium metody rozprostření tepelného toku na
divertoru tokamaku pomocí rychlého rozmítání
magnetického pole

DIPLOMOVÁ PRÁCE

Vypracoval: Bc. Richard Duban
Vedoucí práce: Mgr. Jan Horáček, Ph.D.
Rok: 2017

Sem príde zadanie Diplomovej práce

Prohlášení

Prohlašuji, že jsem svou diplomovou práci vypracoval samostatně a použil jsem pouze podklady (literaturu, projekty, SW ant....) uvedené v příloženém seznamu.

Nemám závažný důvod proti použití tohoto školního díla ve smyslu § 60 Zákona. č. 121/2000 Sb., o právu autorském, o právech souvisejících s právem autorským a o změně některých zákonů (autorský zákon).

V Praze dne

.....
podpis

Acknowledgement:

I would like to thank my supervisor Mgr. Jan Horáček, Phd. for his willingness, time and patience while supervising this thesis. I would also like to thank Geoffrey Cunningham, Martin Imříšek, Josef Havlíček, Václav Sedmidubský, Petr Vondráček and others in COMPASS team.

Richard Duban

Název práce: Studium metody rozprostření tepelného toku na divertoru tokamaku pomocí rychlého rozmítání magnetického pole

Autor: Bc. Richard Duban

Obor: Fyzika a technika termojaderné fúze

Druh práce: Diplomová práce

Vedoucí práce: Mgr. Jan Horáček, Ph.D., Ústav fyziky plazmatu, AV ČR, v.v.i.

Abstrakt: Aby se zabránilo tavení kovových povrchů divertorových desek na velkých fúzních reaktorech lokalizovanými tepelnými toky, studujeme novou techniku rozprostření tepelného toku ELMů pomocí harmonického rozmítání strike pointu divertorových desek cívkou v divertoru. Provedli jsme 2D dynamickou simulaci tepelné vodivosti divertorových desek na tokamaku DEMO s využitím skutečných infračervených dat velkých tepelných toků ELMů na desky divertoru na JET-u. Tepelný tok je přeškálován na EU DEMO reaktor ($B = 6$ T, $I_p = 21$ MA, $R = 9$ m). Pro docílení faktoru zeslabení povrchové teploty $f_{SUP} = 4$ je potřeba rozmítat s amplitudou \times frequency = 7 cm \times 2 kHz. Koncept je založen na jedné cívce s 100 kg hmotností a 29 kW ohmického výkonu v každém divertorovém segmentu, kterých je celkem 54. Rozmítání je spuštěno signálem tepelného toku na divertor. Dynamická simulace ve FIESTA kódu vyžaduje 54 kondenzátorů nabitých na 1.5 kV, každý v RLC obvodu se střídavým proudem s amplitudou 130 kA pro každý ELM po dobu 4 ms (s čekací dobou 50 ms). Síly $I \times B_t$ by způsobovali vibrace cívky s amplitudou ~ 1 mm s frekvencí ELMů (20 Hz). Tato technika se zdá být vhodná pro velké tokamaky. Abychom viděli efekt pohybu strike pointu divertorových deskách, je prezentován návrh pro rozmítanou cívku pro tokamak COMPASS.

Klíčová slova: DEMO, tokamak, ELM, tepelný tok, divertor, faktor zeslabení.

Title: Study of New Technique for Distribution of Tokamak Divertor Plasma Heat Flux by Fast Swept Magnetic Coil

Author: Bc. Richard Duban

Abstract: In order to avoid metal surface melting of divertor targets of big fusion reactors by localized ELM heat loads, we study a new technique of spreading the heat flux by harmonic divertor strike point sweeping using a dedicated divertor coil. We ran 2D dynamic heat conduction simulation of DEMO tokamak divertor targets using real infra-red data of large ELM heat fluxes on JET divertor target. The heat flux is rescaled for EU DEMO reactor ($B = 6$ T, $I_p = 21$ MA, $R = 9$ m). Aiming for the surface temperature suppression factor $f_{SUP} = 4$, this requires sweeping with amplitude \times frequency = 7 cm \times 2 kHz. The concept is based on one coil with 100 kg of mass and 29 kW of ohmic power in each divertor segment, 54 in total. Sweeping is triggered by analog divertor heat flux signal. Dedicated dynamic FIESTA simulation scenario requires 54 capacitive energy storages at 1.5 kV discharged into 54 divertor coils, each in RLC circuit with AC current with 130 kA amplitude for each ELM event for 4 ms (with waiting time 50ms). The $I \times B_t$ forces would yield into coil vibrations with amplitude ~ 1 mm at the ELM frequency (20 Hz). This technique seems to be feasible for big tokamaks. In order to see the effect of the strike point movement, design of the swept coil for COMPASS tokamak is presented.

Key words: DEMO, tokamak, ELM, heat flux, divertor, suppression factor.

Contents

Preface	7
1 Edge localized modes	9
1.1 Edge localized modes	9
1.2 ELM types	10
1.3 Power deposition on divertor targets and main chamber wall	11
1.3.1 Energy deposited on inner/outer target	11
1.3.2 ELM characteristic time scales	12
1.4 Outer target heat fluxes and power decay length scaling	12
1.4.1 Scaling of λ_q	13
1.5 ELM divertor heat load scaling	14
1.6 DEMO Type-I ELMs	15
2 ELM mitigation techniques	16
2.1 ELM mitigation requirements in ITER	16
2.1.1 Primary ELM mitigation requirements in ITER	16
2.1.2 Secondary ELM mitigation requirements in ITER	17
2.2 ELM mitigation using cryogenic deuterium pellets	17
2.3 ELM suppression and mitigation using RMP fields	18
2.4 ELM suppression and mitigation by slow swept heat flux loads on divertor targets	21
3 ELM suppression and mitigation by fast swept magnetic coil on DEMO divertor targets	25
3.1 Sweeping frequency	25
3.2 Definition of the suppression factor	26
3.3 Coil setup	26
3.3.1 Twin coil configuration	26
3.3.2 Split coil configuration	27
3.4 Simulation of the strike-point sweeping in DEMO tokamak	27
3.5 2D heat conduction simulation	28
3.6 Coil electrical scheme and triggering	30
3.7 Skin effect	31
3.8 Coil inductance	32
3.8.1 Measurement of coil inductance in multiple coil setups	33
3.9 Energy in coils	34
3.9.1 Twin coil configuration	35
3.9.2 Split coil configuration	35
3.10 Capacitor energy storage	35
3.11 Circuit quality	35
3.11.1 Twin coil configuration	35
3.11.2 Split coil configuration	36
3.12 Neutronic analysis	36
3.12.1 Nuclear heating	36
3.12.2 Irradiation damage	36
3.13 Electromagnetic force analysis	37
3.13.1 Mechanical vibrations	37

3.13.2	Vertical displacement events	37
3.14	Coil design	38
3.14.1	One turn Litz wire with cooling channel inside	39
3.14.2	Four Litz wires each with cooling channel inside	39
3.14.3	Nine Litz wires each with cooling channel inside	39
3.15	Comparison of coil designs	40
3.16	Scaling of suppression factor f_{SUP}	41
4	Feasibility study of ELM suppression and mitigation on COMPASS divertor targets	43
4.1	RLC circuit	43
4.2	COMPASS ELM parameters	45
4.3	Suppression factor estimation	46
5	Feasibility study of ELM suppression and mitigation on COMPASS-Upgrade divertor targets	47
5.1	Simulation of the strike-point sweeping in COMPASS-Upgrade tokamak	48
5.2	RLC circuit	48
5.3	COMPASS-Upgrade ELM parameters	49
5.4	Suppression factor estimation	49
6	Alternative concept of ELM suppression and mitigation by toroidally localized fast swept C-shaped coil	50
6.1	DEMO C-coil suppression factor estimation	50
6.2	DEMO C-coil parameters	51
6.2.1	Optimizing DEMO C-coil parameters	52
6.3	Magnetic field lines tracking on COMPASS tokamak	53
6.3.1	C-coils magnetic field	53
6.3.2	Magnetic field lines tracking	53
6.4	Design of C-shaped swept magnetic coil on COMPASS tokamak	54
	Conclusion	56

Preface

Humanity needs new energy sources. Energy consumption is growing and is expected to continue to grow in the future. Despite the fact that fossils are exhaustible, have huge impact on environment and probably also on climate change, their consumption rate is still increasing. Growth of fossils consumption is rising mainly in developing countries. Renewable energy sources like wind, solar, geothermal etc. has no capacity to fully cover the world energy consumption despite their positive growth rate. Water energy sources are limited. Nuclear fission has substantial part in the world energy production. Its resources are exhaustible and its share in the world energy production is rather constant. This is partly due to public fear of nuclear energy. Great potential in the future has nuclear fusion. Nuclear fusion is clean, safe and inexhaustible energy source. Nuclear fusion would take place in reactor called tokamak. Today's tokamaks are not able to produce more energy, than they consume. The first tokamak producing substantial amount of energy will be ITER. ITER is being build in Southern France and its operation is planned to start in 2025. The next step in fusion research will be DEMO tokamak as the demonstration power plant.

Today's tokamaks have many problems, which will need to be resolved in the future. One of the biggest issues of ITER-class tokamaks and beyond is suppression or mitigation of large heat fluxes on the first wall and divertor. In DEMO tokamak, energy bursts called Edge localized modes exceed material limit on divertor by a factor of ~ 20 . Therefore it is crucial to find methods to mitigate or suppress these energy bursts. On the one hand, there are many ELM mitigation methods using different approaches. On the other hand, even their combination will not probably be enough to suppress such energy bursts. One of several mitigation techniques is spreading the power in space and time using fast swept magnetic coil, so called fast sweeping. Slow sweeping approach has already been done in JET tokamak [3, 4, 5] and simulated in [6] both with positive results. Fast sweeping, whose analysis is the main goal of this thesis, has not been done yet.

This thesis is composed of six chapters organized as following. First chapter contains basics of Edge localized modes and their scaling to ITER and DEMO. First goal of this thesis is an overview of Edge localized modes mitigation techniques, which are described in the second chapter. Second goal is the study of the concept of Edge localized modes suppression and mitigation by sweeping the strike-point in space and time. Third goal is the simulation of the swept strike point and its interpretation. Third chapter contains study of all aspects of this concept alongside with the simulation of the swept strike point on DEMO divertor targets in FIESTA code and heat conduction simulation in MATLAB. Fourth goal is a small laboratory experiment to confirm some simulation results. Results of the experiment and discussion on feasibility of the swept magnetic coil for tokamak COMPASS are contained in the fourth chapter. Fifth chapter contains the simulation of the swept strike point on tokamak COMPASS-Upgrade. An alternative technique for the swept strike point is studied in the last chapter. Last goal of this thesis is a technical design of the swept magnetic coil for COMPASS tokamak, which is described in the last chapter.

Chapter 1

Edge localized modes

1.1 Edge localized modes

Edge localized mode (ELM) is the large plasma burst ejecting energy and particles towards the divertor or the first-wall. ELMs occur in the high confinement mode called H-mode. The H-mode operation with ELMs will be reference inductive operational scenario for ITER.

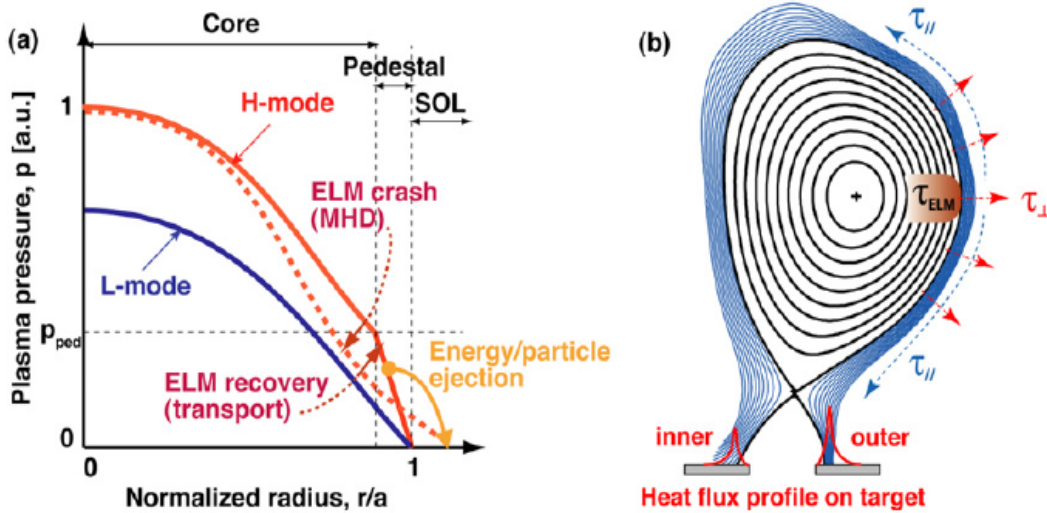


Figure 1.1: (a) Schematic profiles of the pressure profile in L-mode and H-mode before and after ELM crash. ELM crash, ejecting plasma towards SOL and recovery is denoted by arrows. (b) Poloidal cross-section shape of tokamak plasma and ELM formation (τ_{ELM}) and perpendicular (τ_{\perp}) and parallel (τ_{\parallel}) propagation towards divertor/first-wall [1].

Schematic profiles of an edge transport barrier in the plasma pressure can be seen in fig. 1.1 (a). A steep pressure gradient in the plasma edge region at normalized radius of $r/a \sim 0.9-1.0$ is called pedestal. Formation of the pedestal is the main characteristic of the H-mode and does not occur in the L-mode. The pedestal height p_{ped} affects energy confinement and overall plasma performance [1].

ELMs occur when the pedestal pressure reaches its limit by MHD instability. After the plasma energy and the particle ejection into the SOL, it recovers through a transport process. ELMs affect the plasma boundary region ($r/a \geq 0.7-0.8$). Periodic ELMs has a potential to control plasma density and impurity accumulation to the core plasma, but its energy and particles can limit the divertor or first-wall lifetime. According to estimation in [1], heat peak flux to the divertor can reduce the lifetime of the divertor to several hundred shots in ITER.

ELM energy and particle fluxes come dominantly from the outer midplane region as can be seen in fig. 1.1 (b). ELMs have complex movements in radial, poloidal and toroidal direction with a typical duration of $\tau_{ELM} \sim 100-200\mu s$ [1]. The ELM plasma moves at a few km/s near the separatrix perpendicularly to the SOL. ELMs also flow parallel to the magnetic field lines with the ion transport transit time τ_{\parallel}^{ELM} from the pedestal to the divertor, which is defined as the ratio of the connection length to the ion sound speed.

1.2 ELM types

There are a few types of ELMs. They are characterized mainly by a frequency of their occurrence, an ELM frequency f_{ELM} . A typical waveform of a power scan in JT-60U NBI heating plasma is illustrated in fig. 1.2(a) [1]. The input power P_{NBI} is increased in steps starting with the value slightly above the threshold power for an L-H transition. In this phase the plasma is in the Type-III ELM regime. Type-III ELMs are characterized by the ELM frequency f_{ELM} of a few hundreds Hz and a smaller divertor radiation D_{α}^{div} amplitude. At higher input power after a short ELM-free period, Type-I ELM regime starts characterized by the lower ELM frequency with the larger D_{α}^{div} amplitude.

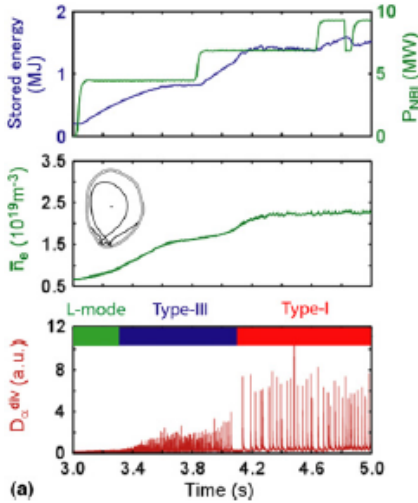


Figure 1.2: (a) Typical waveform of a power scan in JT-60U neutral beam injection heating plasma, line-averaged density and D_{α}^{div} amplitude. [1].

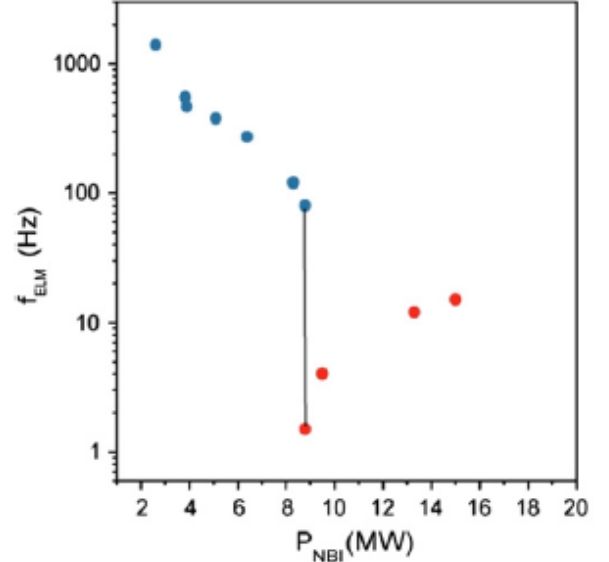


Figure 1.3: ELM frequency f_{ELM} versus heating power P_{NBI} . Type-III ELMs (blue), Type-I ELMs (red) [1].

$$P_{SEP} = P_{heat} - dW_p/dt - P_{rad} \quad (1.1)$$

Since ELMs cause big problems for the plasma-facing materials, advanced H-modes without ELMs like e.g. I-mode, QH-mode, EDA-mode are also studied, however with yet not enough success. High magnetic field is required for those modes, not available on most tokamaks with the exception of Alcator C-mod, which was shut down in 2016. Czech project COMPASS-Upgrade aims to reach those modes thanks to the planned high magnetic field (5 Tesla).

It is possible to categorize ELMs by their power dependences [24]. A dependence of the ELM frequency on the power can be seen in fig. 1.3. In the Type-III ELM H-mode, f_{ELM} decreases with the increasing input power as $df_{ELM}/dP_{SEP} < 0$. On the contrary, in the H-modes with Type-I ELMs, f_{ELM} increases with increasing input power as $df_{ELM}/dP_{SEP} > 0$. P_{SEP} is the heating power crossing the separatrix defined by equation 1.1. P_{heat} is the total input heating power, W_p is plasma stored energy and P_{rad} is radiation loss power.

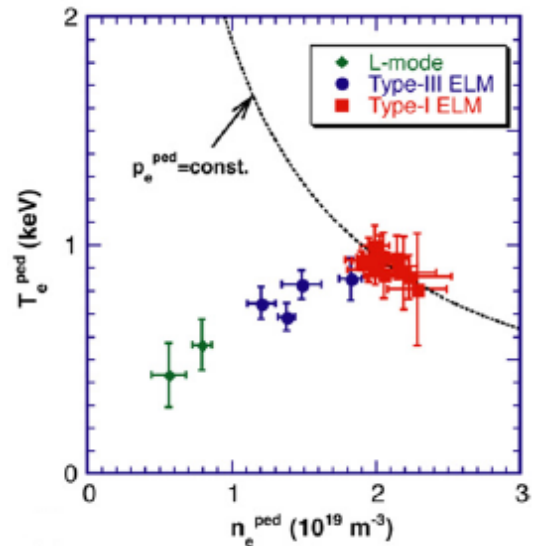


Figure 1.4: $n - T$ diagram at the plasma edge region at around $r/a \sim 0.9$ for L-mode, H-mode with Type-III ELMs and H-mode with Type-I ELMs.

Plasma confinement also depends on the ELM regime. As can be seen in fig. 1.4, pedestal density, temperature and pressure at the plasma edge region at around $r/a \sim 0.9$ are higher in the H-mode, than in the L-mode. In the H-mode, these plasma parameters are higher in the Type-I ELM regime, than in the Type-III ELM regime. Type-I ELMs seem to be an ideal instability. Global plasma confinement also depends on the ELM regime [1].

1.3 Power deposition on divertor targets and main chamber wall

The energy deposited on the inner/outer target, a power deposition rise time τ_{rise} and a fraction of the energy deposited within the τ_{rise} are critical ELM parameters for expectation for the ITER [1]. These parameters are described in the following subsections.

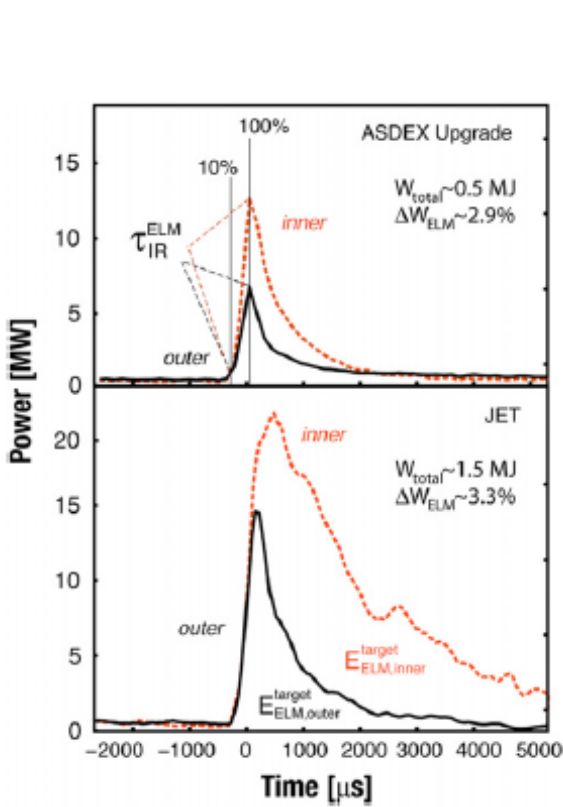


Figure 1.5: Temporal evolution of the power deposition during an ELM event onto the divertor target plates in JET and ASDEX-Upgrade. [1].

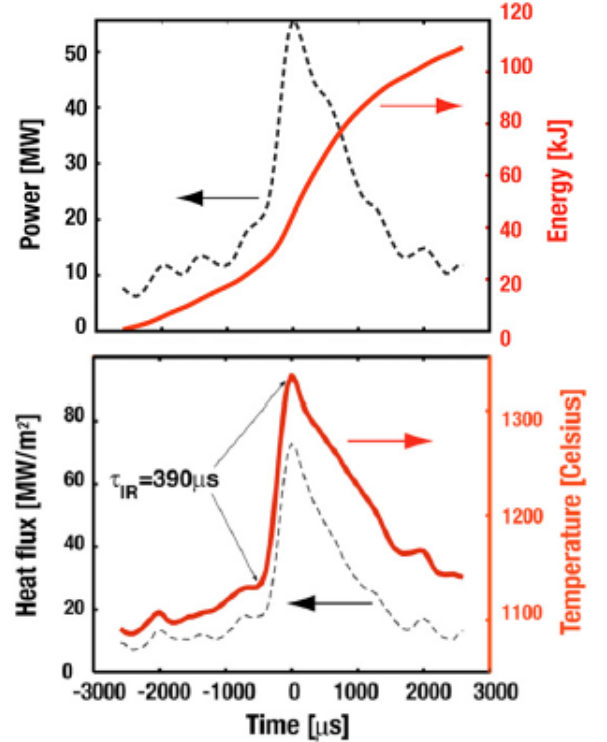


Figure 1.6: Lower: The maximum of the temperature and the heat flux density for an averaged ELM. ELM rise time $\tau_{rise} \sim 390 \mu s$. Upper: The power and the integrated energy of an averaged ELM for the outer divertor target tile on JET tokamak [1].

1.3.1 Energy deposited on inner/outer target

The temporal evolution of the power deposition during an ELM onto the divertor target plates on ASDEX-Upgrade and JET Tokamaks is shown in fig. 1.5. The temporal evolution onto inner and outer targets has similar character, but differs in the scale. The relative ELM size, the ratio of the ELM energy to the pedestal energy $\Delta W_{ELM}/W_{ped}$, is about 10% in both machines. The total deposited ELM energy onto the inner target $E_{ELM}^{inner-target}$ is larger than energy deposited onto the outer target $E_{ELM}^{outer-target}$. This is observed in [1] despite the fact that power load between ELMs coming dominantly from the low field site is mostly deposited on the outboard divertor target. This phenomenon is not understood yet.

1.3.2 ELM characteristic time scales

Upper fig. 1.6 shows an ELM power and an integrated energy of an averaged ELM for the outer divertor target tile on JET. Bottom fig. 1.6 shows a temperature and a heat flux of an ELM for the outer divertor target tile. The Heat flux is calculated from the temperature rise. According to [1], the target temperature and the heat flux density increase on timescales of $\tau_{rise} \sim 390 \mu s$. τ_{rise} , also called the ELM rise time, is an ELM power deposition time. An ELM decay time τ_{decay} characterize an exponential decay of the ELM heat flux. It is the difference between the time of maximum heat flux and the time when heat flux decays on $1/e$ of its original value. Since τ_{decay} is always much higher than τ_{rise} , τ_{decay} is usually called an ELM time τ_{ELM} . According to [1], τ_{ELM} on ITER is estimated to have values $\sim 400 \pm 150 \mu s$. Power and integrated energy of an ELM for the outer divertor target tile on JET is shown in upper fig. 1.6. During the ELM power deposition time τ_{rise} is deposited only a fraction of the target load energy. The rest of the energy arrives after the maximum power load. Target does not reach maximum temperature immediately after the ELM crash as is measured in fig. bottom fig. 1.6. In this case, temperature is maximal immediately after the ELM crash probably due to some dust layer on the target.

$$\Delta T = \frac{2q_n}{k} \sqrt{\frac{\kappa t}{\pi}} \quad (1.2)$$

According to [32], a temperature in time is given by an analytical equation 1.2. $\kappa = k/(\rho C_p)$, where k , ρ and C_p are material conductivity, density and specific heat. Time until target reaches maximum temperature after the ELM crash is comparable to τ_{decay} .

1.4 Outer target heat fluxes and power decay length scaling

$$q(\bar{s}) = q_0 \exp\left(\left(\frac{S}{2\lambda_q}\right)^2 - \frac{\bar{s}}{\lambda_q}\right) \times \text{erfc}\left(\frac{S}{2\lambda_q} - \frac{\bar{s}}{\lambda_q}\right) + q_{BG} \quad (1.3)$$

In order to suppress large heat loads, not only a detailed knowledge of temporal profiles, but also a knowledge of spatial heat load profiles is crucial. One of the main characteristics of a spatial heat load profile is a power decay length λ_q . The power decay length λ_q is the constant characterizing exponential decay of the heat load and determining a power exhaust on the targets. Target heat flux profile measured by a thermography is possible to be represented as a convolution of an exponential function with the decay λ_q and a gaussian of width S . A gaussian function of width S characterize radial diffusion in the divertor. This has been derived in the inter-ELM H-mode with fully attached divertor on JET and ASDEX Upgrade tokamaks in [22].

$$q(\bar{s}) = q_0 \exp\left(-\frac{\bar{s}}{\lambda_q}\right) \quad (1.4)$$

Assuming s to be a target coordinate and a strike line position on the target s_0 , the heat load profile at the divertor $q(\bar{s})$ can be estimated by equation 1.4. $\bar{s} = s - s_0$.

Perpendicular heat diffusion into the private-flux-region can be adjusted by the Gaussian width S . This can be interpreted as a diffusion into the private flux region and a traveling towards the target at the same time. An approximate heat flux profile can be expressed by a convolution of the exponential profile with a gaussian function with the width S , if flux expansion f_x is neglected. Such a heat flux profile is given by equation 1.3, derived in [22].

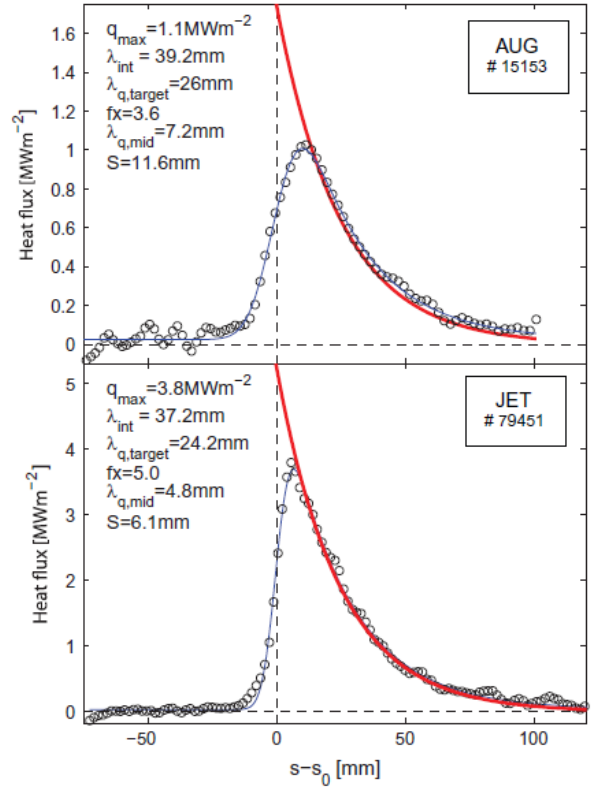


Figure 1.7: Heat flux profiles measured on the outer divertor target and fits using Eq. 1.3 [22].

Two measured and fitted heat flux profiles from JET and AUG tokamaks can be seen on fig. 1.7. From eq. 1.3 follows an integral power decay width λ_{int} and its dependence on λ_q .

Dependence of a power deposited on the divertor target and a peak heat load is related by eq. 1.5, which is important parameter for ITER power handling capabilities derived in [22].

$$\lambda_{int} = \frac{\int (q(s) - q_{BG}) ds}{q_{max}} = \lambda_q + 1.64S \quad (1.5)$$

1.4.1 Scaling of λ_q

For ELM suppression and mitigation, knowledge of the dependence of ELM parameters like λ_q and ELM heat load on basic machine parameters is crucial. Following sections contains scaling of λ_q and ELM heat load.

A parametric dependency of the L-mode power decay length on toroidal magnetic field B_t , cylindrical safety factor q_{cyl} (for JET only), safety factor q_{95} , power crossing the separatrix P_{SOL} and major radius R is derived using least square fitting. From 15 hydrogen and 7 deuterium JET plasmas and 13 deuterium AUG plasmas is derived scaling law for L-mode $\lambda_{q,L-mode}$ given by equation 1.6.

$$\lambda_{q,L-mode} = (1.44 \pm 0.67) \cdot B_T^{-0.80 \pm 0.32} \cdot q_{95}^{1.14 \pm 0.67} \cdot P_{SOL}^{0.22 \pm 0.10} \cdot R^{-0.03 \pm 0.28} \quad (1.6)$$

Since λ_q has no statistically significant dependence on the plasma density, it is not included into the fit parameters. Dependence of λ_q on R is negligible. λ_q has nearly linear dependence on safety factor. For comparison of inter-ELM decay length $\lambda_{q,H-mode}$ in H-mode plasmas, an H-mode scaling law is presented in equation 1.7.

$$\lambda_{q,H-mode} = 0.73 \cdot B_T^{-0.78} \cdot q_{cyl}^{1.20} \cdot P_{SOL}^{0.10 \pm 0.10} \cdot R^{0.02} \quad (1.7)$$

Main difference between scaling laws in the L-mode and the H-mode is that $\lambda_{q,H-mode}$ is 2–3 times larger than $\lambda_{q,L-mode}$. This is probably due to higher radial transport in the L-mode than in the H-mode plasma, SOL and divertor. These two scalings derived in [22] are valid for inter-ELM λ_q only.

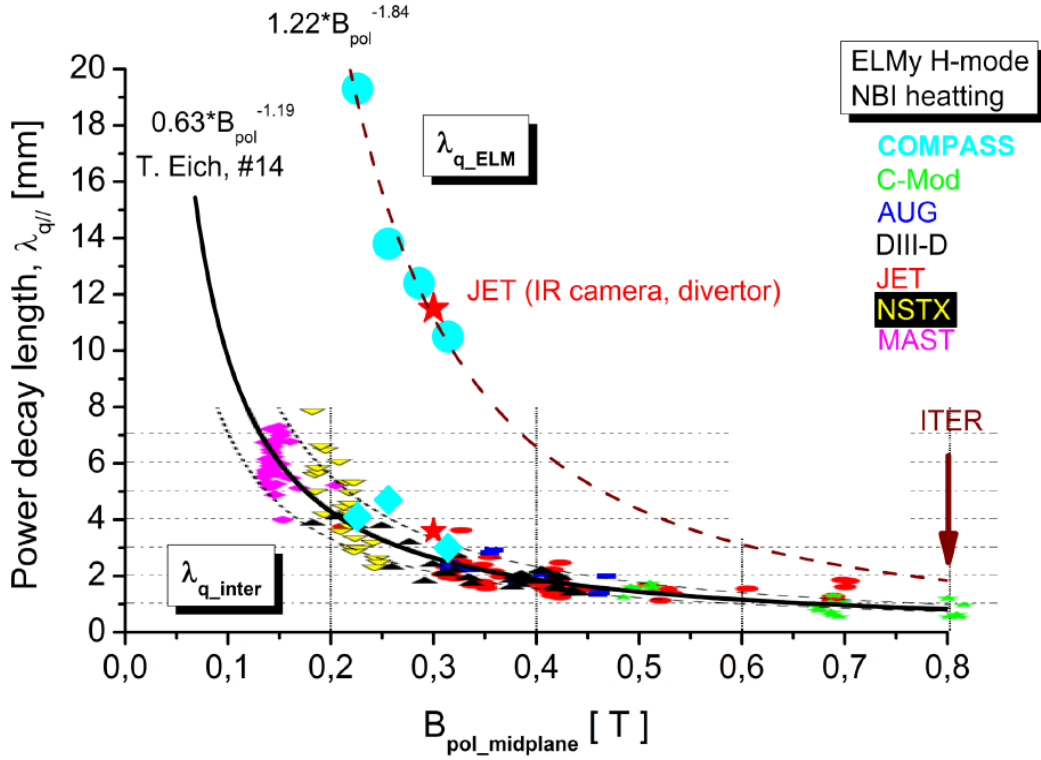


Figure 1.8: Poloidal magnetic field at the outer midplane versus inter-ELM power decay length λ_{q_inter} (black curve) and ELM power decay length λ_{q_ELM} (black dashed curve) [23].

λ_q has the most statistically significant dependence on poloidal magnetic field. Fig. 1.8 shows dependence of inter-ELM power decay length λ_{q_inter} (black curve) and ELM power decay length λ_{q_ELM} (black dashed

curve) on poloidal magnetic field on midplane $B_{pol_midplane}$ measured in the H-mode in multiple machines.

$$\lambda_{q_inter} \sim 0.63 \cdot B_{pol_midplane}^{-1.19} \quad (1.8)$$

The same dependence as 1.7 of inter-ELM λ_{q_inter} and ELM λ_{q_ELM} on $B_{pol_midplane}$ can be also expressed by equations 1.8 and 1.9 respectively according to [23].

$$\lambda_{q_inter} \sim 1.22 \cdot B_{pol_midplane}^{-1.84} \quad (1.9)$$

Ratio of inter-ELM power decay length λ_{q_inter} and ELM power decay length λ_{q_ELM} is called ELM broadening.

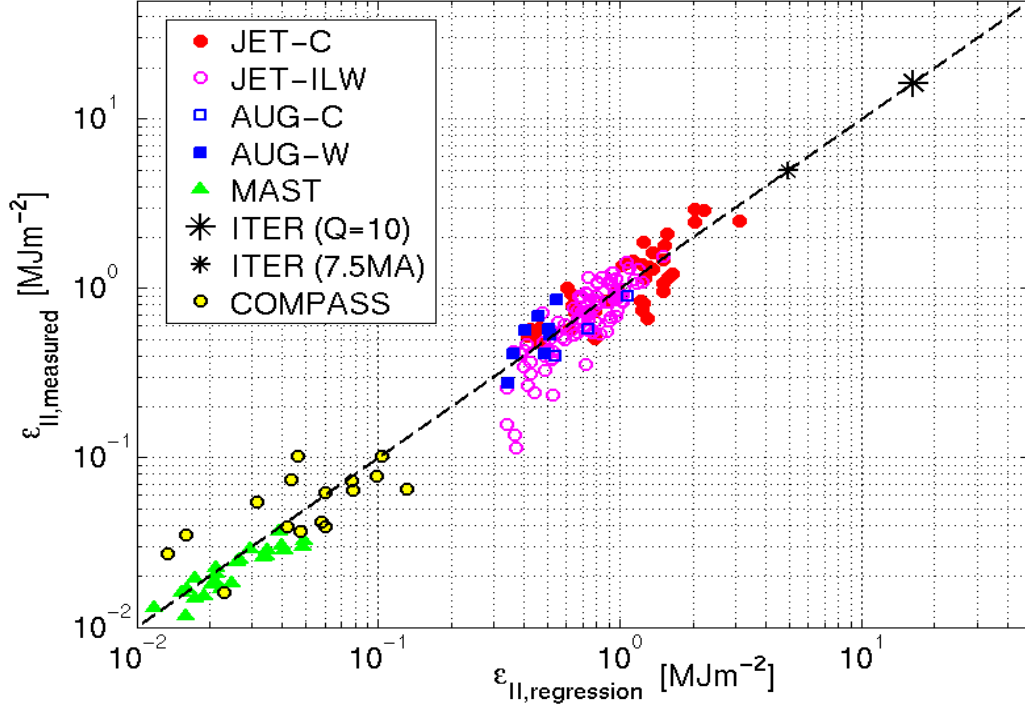


Figure 1.9: Regression of the outer divertor parallel ELM energy density in multiple machines as parameterized in equation 1.10. Parallel peak ELM energy resulting from this scaling is in the range of 10–30 MJ/m² for ITER Q=10 operation and 2.5–7.5 MJ/m² for operation at 7.5 MA and 2.65 T [30].

1.5 ELM divertor heat load scaling

Recent measurements in [30] of the ELM energy density on multiple machines reveals an approximately linear dependence of the peak ELM energy density with a pedestal top electron pressure, a minor radius and a square root dependence of a relative ELM energy loss. Since ITER is foreseen to be operated in the type-I ELMy H-mode, an extrapolation of ELM heat loads is important for a definition of an operational range of future devices and a need for ELM mitigation techniques.

$$\epsilon_{||} = 0.28 \pm 0.14 \frac{MJ}{m^2} \times n_{e,ped,top}^{0.75 \pm 0.15} \times T_{e,ped,top}^{0.98 \pm 0.1} \times \Delta E_{ELM}^{0.52 \pm 0.16} \times R_{geo}^{1 \pm 0.4} \quad (1.10)$$

Equation 1.10 is a result of a scaling of the parallel ELM heat load with a top pedestal density $n_{e,ped,top}$, a top pedestal electron temperature $T_{e,ped,top}$, the ratio of the ELM energy size to the total plasma energy $\Delta_{ELM} = E_{ELM}/W_{plasma}$ and a geometrical major radius R_{geo} . A comparison of the measured data on multiple machines and the scaling using equation 1.10 is shown in fig. 1.9. Parallel peak ELM energy resulting from this scaling is in the range of 10–30 MJ/m² for ITER Q=10 operation and 2.5–7.5 MJ/m² for operation at 7.5 MA and 2.65 T.

Using simple model for ELM energy density can be scaling law 1.10 rewritten into an expression for the ELM energy density given by equation 1.11.

$$\epsilon_{\parallel} \cong 6\pi p_e R_{geo} q_{cyl} \quad (1.11)$$

The classic number for the ELM divertor heat load is typically quoted to be 0.5 MJ/m². This number is valid in case of fully axisymmetric divertor target plates. According to [30], if the castellation of the ITER divertor and finite ion orbit effect causing edge melting is taken into account, material limit is reduced from 0.5 MJ/m² to 1.15 MJ/m².

1.6 DEMO Type-I ELMs

Characteristics of DEMO ELMs can be scaled using data from large-scale tokamaks and those extrapolated for ITER. There are two versions of DEMO, DEMO1 based on near future technology and advanced steady-state DEMO2. Thermal energy for unmitigated ELMs in DEMO1/2 is expected in the range $\sim 80/160$ MJ. A maximum of the ELM energy loads due to in/out asymmetry should be on inboard divertor about 50/110 MJ and in outboard divertor 40/80 MJ. It can be assumed, that the shape of ELM power loading at the mid-plane in DEMO will be the same as in ITER. The same assumption can be done about ELM decay phase being twice the rising phase. According to [33], the energy density load to the out-inboard divertor plates could be in the range of 15–20 MJ/m² in DEMO1. Energy deposition time is estimated to have values about ~ 0.6 ms and decay time ~ 1.2 ms. In the whole thesis, DEMO1 is meant when DEMO version is not specified.

The Type-I ELM frequency scales as $f_{ELM} \sim (\tau_E^{-1/7})$, where τ_E is energy confinement time. The confinement time for DEMO ELMy H-mode has value ~ 6.47 s, which is $\sim 1.8 \times$ confinement time for ITER. ELM frequency in DEMO is than about 0.8 Hz which is slightly lower than in ITER ~ 1 -2 Hz.

For ELM mitigation can be used the same techniques as in ITER. Amplitude could be reduced ~ 33 times, which leads into ELM energy 0.6 MJ/m². Because of the product of amplitude and frequency is constant, ELMs with such an energy would have frequency $f_{ELM} \sim 26$ Hz.

It is expected that unmitigated ELMs will erode tungsten armor leading to surface melting and melt splashing. The heat load of single giant ELMs result in melting and evaporation according to [33].

Chapter 2

ELM mitigation techniques

Large array of suppression and mitigation techniques have been developed due to the urgency of the ELM issue for ITER-class tokamaks and beyond. (1) The application of edge Resonant Magnetic Perturbation (RMP) fields, (2) ELM pacing with small, high frequency, frozen deuterium pellets, (3) operation in naturally occurring quiescent H-mode plasmas and I-mode regimes, (4) impurity seeding, (5) the use of small periodic vertical equilibrium displacements, (6) the injection of supersonic molecular beams, (7) the application of low recycling wall materials like lithium coatings, (8) the application of small toroidal ripple fields and (10) operations in naturally occurring small ELM regimes which include Enhanced D_α H-mode, grassy ELMs, the High Recycling Steady H-mode, Type-II ELMs, Type V ELMs and snow flake divertor configurations. Into the ITER baseline plan was included pellet pacing and edge RMP fields [2]. These two techniques are described in following sections alongside with ELM mitigation requirements in ITER. Last section contains simulation of ELM suppression and mitigation by swept heat flux loads on divertor targets.

2.1 ELM mitigation requirements in ITER

2.1.1 Primary ELM mitigation requirements in ITER

The number of ELMs that are expected in ITER before the divertor must be replaced is a function of the ELM energy ΔW_{ELM} , the ELM energy impulse time Δt_{ELM} and the properties of the divertor target plates material, as shown in Fig. 2.1 [8]. Main requirement for ELM control systems is reducing of ΔW_{ELM} together with maintaining high core density H-mode plasmas, low impurity fraction and low electron pedestal collisionalities. Results from experiments exposing divertor target components to large transient energy impulses similar to those expected during an ELM in ITER reduce maximum acceptable ELM impulse energy density in ITER to $\varepsilon_{ELM} = 0.5$ MJ/m², assuming $\Delta t_{ELM} \geq 250\text{--}500\mu\text{s}$ [9, 10, 11]. For 15 MA $Q_{DT} = 10$ plasmas, referred to as scenario 2 inductive H-modes, with $R = 6.2$ m, $a = 2.0$ m, $I_p = 15$ MA, $B_T = 5.3$ T, an H-mode factor $H_{98(y,2)} = 1.0$, an internal inductance $l_i = 0.8$, an elongation $\kappa = 1.7\text{--}1.85$, a normalized plasmas pressure $\beta_N = 1.8$ and a fusion burn duration $\tau_{burn} = 300\text{--}500$ s, this yields ELM maximum energy $\Delta W_{ELM} \approx 0.7$ MJ. Surface area of the ELM interaction with the divertor targets $A_{ELM} = 1.4$ m² can be assumed. As can be seen in Fig. 2.2, the acceptable level of ΔW_{ELM} depends strongly on I_p and A_{ELM} . Acceptable values of ΔW_{ELM} reside in the regions below the solid lines for tungsten divertor target plates. $A_{ss} = 1.4$ m² is the steady-state heat flux area between ELMs. It is expected that A_{ELM} increases with the size of the ELMs from A_{ss} to $3A_{ss}$

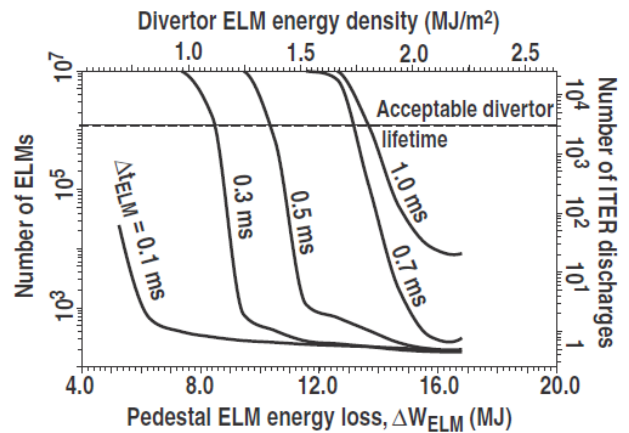


Figure 2.1: Number of Type-I ELMs full length ITER discharges resulting in the complete erosion of the tungsten divertor in ITER vs. ΔW_{ELM} and the deposition time Δt_{ELM} of the ELM energy impulse. [8].

and to $6A_{ss}$. The scaling of the heat flux area with ELM size is not known at this time leading to additional uncertainty in the requirements of ΔW_{ELM} in ITER. The expectation is that acceptable ΔW_{ELM} will increase with A_{ELM} , which yields ε_{ELM} constant. In comparison with wolfram divertor, Be walls show an inverted dependence on I_p . Because of the plasma contact with the main chamber plasma facing components, the power loading limit on the Be walls has been established at 50% of the melting threshold [2].

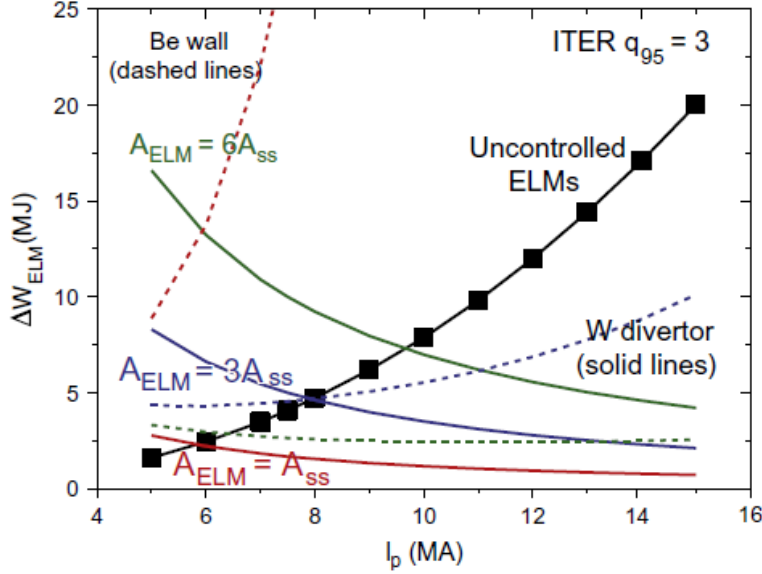


Figure 2.2: Scaling of ΔW_{ELM} with the ITER plasma current in $q_{95} = 3$ discharges. The upper limit for acceptable ELM energy impulses with tungsten divertor plates assuming ELM surface interactions area of $A_{SS} = 1.4 \text{ m}^2$ (red), $3A_{SS}$ (blue) and $6A_{SS}$ (green) is represented by solid lines. Dashed lines represent upper limits for ΔW_{ELM} on the beryllium walls for three values of A_{SS} . [11].

2.1.2 Secondary ELM mitigation requirements in ITER

The primary requirements pose a significant challenge for ELM control systems. There are a variety of secondary requirements that must also be met. The first of these is the ability to mitigate ELMs during I_p ramps at the beginning and the end of each discharge, because of the necessity to operate in an H-mode during I_p rampup and rampdown phases. Another requirement is the need to mitigate or suppress the first ELM following the H-mode transition. The first ELM following the H-mode transition and the associated ELM-free period results in a particularly large ΔW_{ELM} that may lead to a substantially enhanced erosion rate or melting [2].

2.2 ELM mitigation using cryogenic deuterium pellets

Periodic injecting of cryogenic deuterium pellets at a frequency significantly exceeding the expected natural ELM frequency $f_{N_ELM} = 1\text{--}2 \text{ Hz}$ in ITER is one of the main strategies planned for limiting the maximum ΔW_{ELM} in ITER. This method is called pellet pacing [12]. From a database of ΔW_{ELM} of naturally occurring ELMs in several tokamaks is found following empirical formula 2.1.

$$\Delta W_{ELM} = 0.2 \times W_{plasma} \left(\frac{\tau_{ELM}}{\tau_E} \right) \quad (2.1)$$

W_{plasma} is plasma stored energy, τ_{ELM} is the period of ELM cycle and τ_E is the energy confinement time [13]. Based on Eq. 2.1, with $W_{plasma} = 300 \text{ MJ}$, $\tau_E = 3 \text{ s}$ and $\Delta W_{ELM} = 20 \text{ MJ}$, to reach $\Delta W_{ELM} = 0.7 \text{ MJ}$, $\tau_{ELM} = 1/f_{N_ELM}$ must be decreased from 500–1000 ms to 15–30 ms. Pellet pacing results from mid-sized tokamaks have shown over-fueling of the plasma as the result of naturally high ELM frequency which sets restrictions on pellet frequencies.

Pellet pacing studies in ASDEX-Upgrade have demonstrated synchronization of ELMs with the pellet frequency when pellet frequency reaches $1.5f_{N_ELM}$, $\sim 45 \text{ Hz}$ [14]. Synchronization remained as pellet frequency

increased up to value of $2.5f_{N_ELM}$, ~ 80 Hz. Results from these experiments also showed modest reduction in confinement, $W_{plasma} \sim f_{ELM}^{-0.16}$ and found that ΔW_{ELM} scales for pellet paced ELMs like for natural ELMs. Ability to reduce τ_{ELM} simultaneously with maintaining good values of τ_E was demonstrated in DIII-D tokamak [15]. An example of a discharge with injected 1.8 mm D₂ pellets, containing 2×10^{20} atoms per pellet, into a plasma with $f_{N_ELM} = 5$ Hz is shown in Fig. 2.3. Pellets were injected at 14 Hz, $2.8f_{N_ELM}$. Resulting ELMs had a frequency of 25 Hz, that is a factor of 5 increase in f_{N_ELM} in comparison with reference discharge. That indicates the presence of natural ELMs not synchronized with the pellets. This could be a result of a change in the pedestal conditions from an increase in the edge neutral density [15]. Decrease of the toroidal rotation velocity at the top of the pedestal from 55 km/s without pellet pacing to 35 km/s during pellet pacing was also found. This reduction in toroidal rotation needs to be better understood. The key constraint on this approach is emphasized by these results, which is that the pedestal should remain unchanged under optimized pellet pacing conditions [2].

Pellet pacing results from JET, ASDEX-Upgrade and DIII-D have provided strong support for the premise that ELMs can be triggered up to relatively high frequencies by pellets after a threshold frequency is achieved [16, 14, 15]. Uncertainties in the physics and the technology needed to scale this approach to ITER conditions still need to be resolved. There are some technological challenges of injecting D₂ pellets at a frequency within the range of 30–60 Hz in ITER. For example the ability to produce reliable and well controlled pellet sizes over extended periods is a significant cryo-engineering challenge [2].

Numerical models of the instability driven by the local pressure perturbation triggered by the pellets are used for a detailed physics understanding. According to nonlinear jorek MHD code [17], shallow pellets produce a large density perturbation that expands at the local sound speed along the magnetic field lines. The MHD instability triggering the ELM is caused by the pressure inside the expanding plasmoid exceeding background plasma pressure [18]. Simulations are required to help resolve some uncertainties related to the requirements on the pellet size, penetration depth and particle throughput needed to specify a detailed design of the pellet pacing system for ITER. Determination of the minimum pellet size and velocity required to trigger ELMs is important [2].

2.3 ELM suppression and mitigation using RMP fields

RMP fields, non-axisymmetric magnetic fields, provide an effective mechanism for the controlling macroscopic dynamics of the plasma in tokamaks and stellarators. Small RMP fields can be used to suppress or mitigate ELMs by controlling the pedestal plasma in H-modes [2].

The most important effects of RMP fields are changes in the plasma density, turbulence and neutral particle dynamics, which are crucial for ELM mitigation and suppression. First RMP experiments on the TEXT tokamak showed that the ability to modify the exchange of neutrals and ions between the plasma facing components and the edge plasma is a very effective way of controlling the performance of the tokamak. RMP driven improved particle confinement regime was discovered in the JIPP T-IIU, Tore Supra, COMPASS-C and TEXTOR tokamaks and in the Wendelstein 7-AS stellarator and the LHD heliotron. RMP fields can result in the destabilization of small ELMs in naturally occurring ELM-free H-modes with an uncontrolled density rise. This is an operational space known as the RMP ELM mitigation regime where small ELMs with high frequency are driven by the RMP field. The inclusion of ELM control coils inside the ITER vacuum vessel was triggered by the discovery of the ELM suppression, in which ELMs were completely eliminated by the RMP fields in DIII-D tokamak H-modes [2].

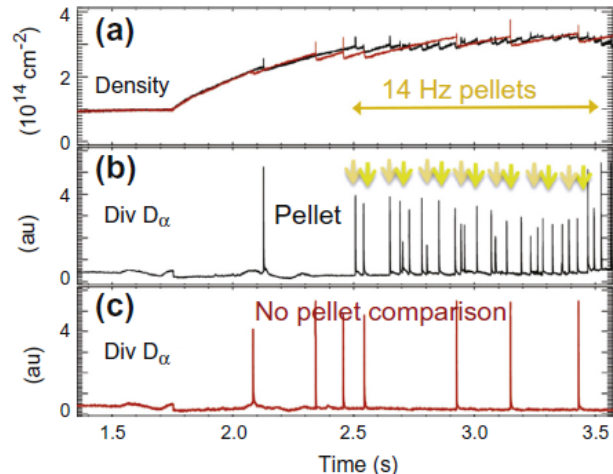


Figure 2.3: ELM response to 1.8 mm D₂ pellets injected into a DIII-D H-mode plasma. (a) Plasma density and the time interval over which the 14 Hz pellets were injected, (b) divertor D_α recycling showing 25 Hz ELMs triggered by the pellets and (c) natural ELMs in a similar discharge with no pellets. [15]

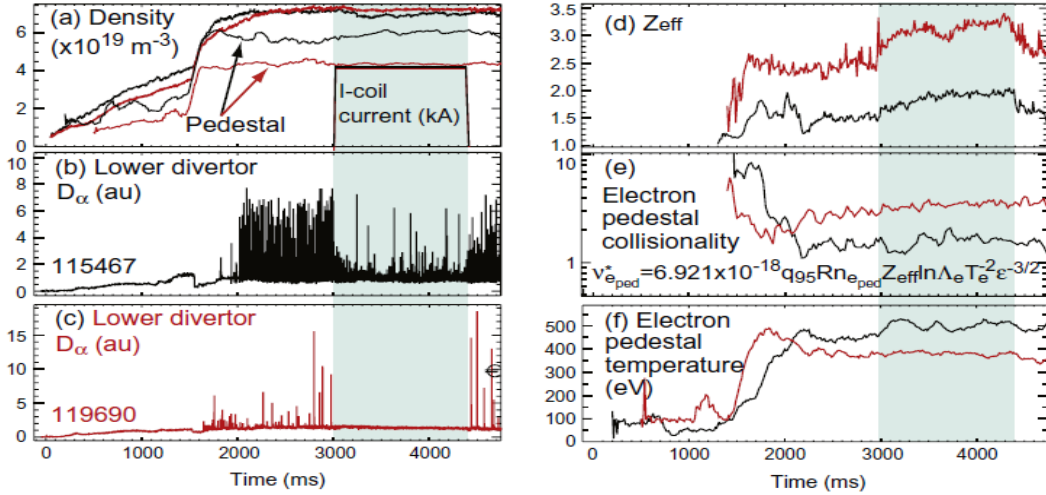


Figure 2.4: Comparison of RMP plasma response in two similar DIII-D plasmas with slightly different shapes where (a) the pedestal and line average density, (b) the divertor recycling in 115467, (c) the divertor recycling in 119690, (d) the edge Z_{eff} , (e) the electron pedestal ν_e^* and (f) the electron pedestal temperature are seen to be quite different from the beginning of the discharges. [2].

ELMs in JET with $n = 2$ and MAST with $n = 3$ were mitigated as well as high-density ELMs on ASDEX-Upgrade with $n = 2$ fields. Some of the properties seen in the original DIII-D experiments were reproduced while others were not. The key to the success of ELM suppression in DIII-D and ELM mitigation in ASDEX-Upgrade, JET, MAST, and DIII-D is the ability of the RMP to keep steady-state density and impurity control over a wide range of pedestal parameters [2].

Two high-density ELM suppressions/mitigations in DIII-D can be seen in fig. 2.4. In two shots, the response to an equivalent RMP pulse is shown in plasmas with slightly different shapes. During the RMP phase line average density n_e is not significantly reduced. Effective particle charge number Z_{eff} is slightly increased during the RMP, but there is no big change in τ_E , H factor or W_{plasma} . Except increase in the lower triangularity $\delta_L = 0.601$ in 119690 to $\delta_L = 0.728$ in 115467, a significant difference in these two discharges is a 38 % increase in the L-mode D_α neutral particle recycling with an average L-mode gas fueling rate of 5.71 kPa L/s during 119690, compared to 7.57 kPa L/s during the L-mode phase in 115467. This shows the importance of understanding the neutral particle sources and sinks during RMP ELM control experiments and the effects of changing wall conditions [2].

Analysis of the global particle balance in discharges similar to those in fig. 2.4 have shown that the effective particle confinement time ($\tau_p^* = \tau_p^*/1 - R$, where R is the recycling coefficient) increases with increasing ν_e^* . High-density (high electron collisionality ν_e^*) ELM suppression discharges have increased pedestal density fluctuations. The interaction of the higher neutral density with the pedestal plasma increases the turbulence and changes dynamics to a more intermittent type of transport with high ν_e^* . ELM energy is dissipated by an increase in the intermittent transport driven by recycling and higher neutral densities [2].

In DIII-D low collisionality discharges ($\nu_e^* = 0.1-0.04$), ELM suppression is obtained reproducibly over a

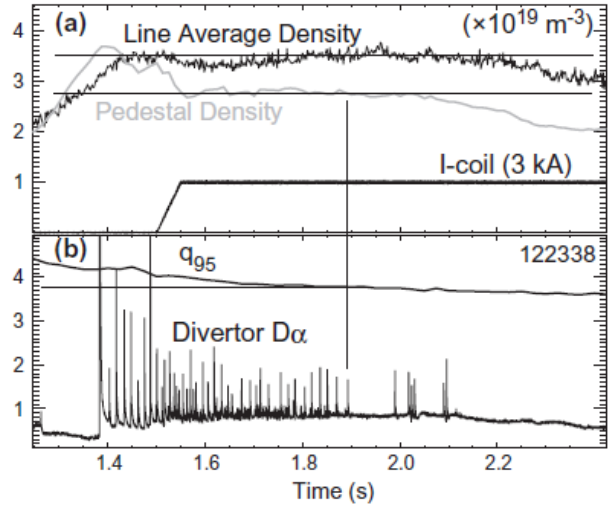


Figure 2.5: Evolution of the line-average and pedestal density vs. time before and during the application of the RMP field from the DIII-D I-coil and (b) changes in the ELMs due to the RMP field as q_{95} crosses the upper boundary of resonant window for ELM suppression located at $q_{95} = 3.7$. [2].

wide range of pedestal and core confinement regimes but it is also found that the response of the pedestal density and neutral particle dynamics is sensitive to δ_L and the geometry of the divertor. Neutral particle recycling is an important player in the significantly different density response and confinement changes. Changes in the toroidal rotation during ELM suppression and mitigation are not well understood and behave differently on different machines [2].

Fig. 2.5a shows the evolution of the line-average density and the pedestal density before and during the application of the I-coil RMP field in lower single null $\delta_L = 0.37$ DIII-D plasma. After being constant, the pedestal density drops immediately when the RMP field is applied. Fig. 2.5b shows ELM suppression as q_{95} approached the resonant window. The ELMs are mitigated by the RMP field, while $q_{95} > 3.7$ and then suppressed after $t = 2.1$ s. Fig. 2.6 shows the density profiles averaged over three time windows for the discharge shown in Fig. 2.5. RMP field reduces the pedestal density and increases the core plasma density. The central ion temperature and density rise probably due to formation of an internal ion transport like barrier [2].

The ability to minimize the reduction in the line-average and pedestal density by changing the I-coil current after ELM suppression was demonstrated in ISS plasmas with $\delta_L = 0.7$. As can be seen in Fig. 2.7, periodical flipping by 60° of the $n = 3$ RMP field causes the line-average density to drop and the ELM frequency to increase. Line-average density slowly increases after ELM suppression. The change in the I-coil current represents a toroidal phase flip of the RMP field by 60° . The toroidal rotation at the top of the pedestal soars to ~ 100 km/s with the phase change, but the density continues to increase on a slower time scale. Each time after the RMP field passes through zero, a single ELM is triggered. The line-average density before turning on the RMP field can be achieved by repeating these phase flips every 0.2 s [2].

These results suggest a scenario in which the plasma response to the RMP field depends on the dynamics of the plasma when the RMP field is first applied and on the nonlinear evolution of the pedestal following the initial application of the RMP. As can be seen in fig. 2.7, I-coil current switch is an effective mechanism for providing momentum input to the plasma on a short time scale [2].

The ability to change the properties of the perturbation field for different plasma shapes and operating conditions is an important attribute of the RMP ELM control approach. ELM mitigation or suppression was obtained in every operating scenario in DIII-D as well as in other machines such as JET, MAST, ASDEX-Upgrade and KSTAR despite of each having very different RMP coil designs and perturbation spectra [2].

In ITER the ELM coils are designed to control the amplitude and phase of the perturbation field, which is important feature for implementing real-time feedback control algorithms. Steady-state divertor heat flux during ELM suppression or mitigation will be smoothed out by 5 Hz toroidal rotation of the RMP fields [2].

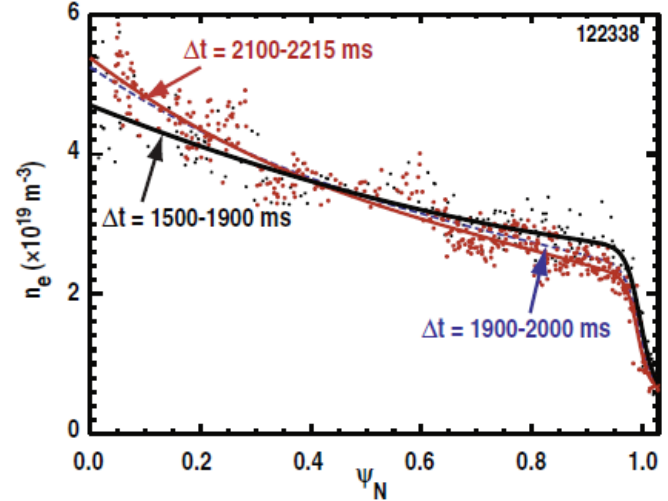


Figure 2.6: Changes in the electron density profile measured with a Thomson scattering system on DIII-D before the introduction of an $n = 3$ RMP field averaged over $t = 1500$ – 1900 ms, during the ELM mitigated phase of the RMP pulse $t = 1900$ – 2000 ms and during the ELM suppressed phase of the RMP pulse $t = 2100$ – 2215 ms for the discharge shown in Fig. 2.5. [2].

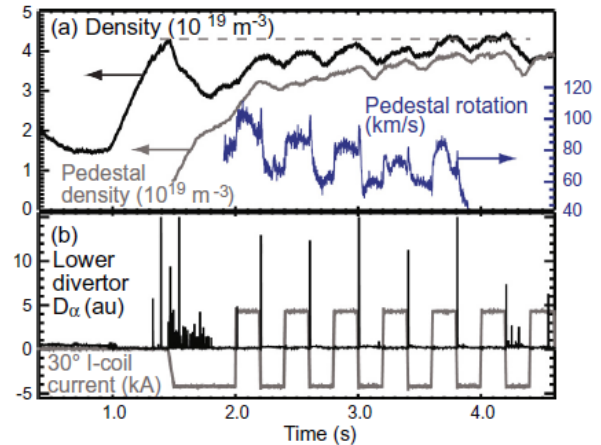


Figure 2.7: (a) Pedestal toroidal rotation, line-average and pedestal density response to an $n = 360^\circ$ toroidal RMP field phase flip and (b) lower divertor D_{α} emission and RMP coil current as a function of time during $n = 3$ toroidal phase flips in DIII-D discharge 147170. [2].

2.4 ELM suppression and mitigation by slow swept heat flux loads on divertor targets

Sweeping the position of the strike-point periodically in space and time in order to spread the energy load over a wider width is an additional possibility to mitigate ELMs. The strike-point sweeping concept has been already carried out in the JET experiments [3, 4, 5]. This technique could be used as a steady state system for decreasing the thermal load on divertor targets during normal operation or as a supplementary technique in case a sudden increase of the thermal load. Numerical simulations are being performed to study the impact of various parameters on the thermal response of a target under sweeping operation. Furthermore, to study the feasibility of the sweeping technique, overall analyses are needed. This includes power source, operational amplitude and frequency of sweeping, influence on plasma stability and quality of the confinement, power dissipation in the surrounding coils and local temperature rise [6].

The aim of this section is studying cyclic heat flux loads applied in sweeping modes and their thermal and structure-mechanical responses of a water-cooled tungsten mono-block. The reduction of peak temperature and maximum heat flux to the heat sink and structural risk caused by the thermal fatigue of the heat sink are principal [6].

Fig. 2.8 displays expected footprint of the heat flux power on the outer target based on the latest predictions [7]. As can be seen in Fig. 2.9, the footprint of the heat flux power is swept at the surface of the divertor targets parallel to the cooling tube. Divertor target is composed of small square tungsten blocks connected by a cooling tube. Between each two blocks there is ~ 3 mm gap. The sweeping amplitude is defined as the distance between two outermost maximums of the heat flux footprints. Sweeping amplitude and the sweeping frequency determine the maximum temperature position during sweeping. The difference between the maximum temperatures of the targets and of the selected mono-block divertor is less than 100° for loading conditions studied in this section based on a rough estimation from a 2D finite element (FE) simulation [6].

Fig. 2.11 shows the geometry, the FE mesh and the constituent materials for the model of water-cooled tungsten mono-block duplex structure. Structure consists of a tungsten armor block and a copper alloy cooling tube. During sweeping, the maximum temperature occurs at the left edge of the mono-block. In the stationary case, the heat flux peak is positioned at the middle line between the left and right edges of the top surface [6].

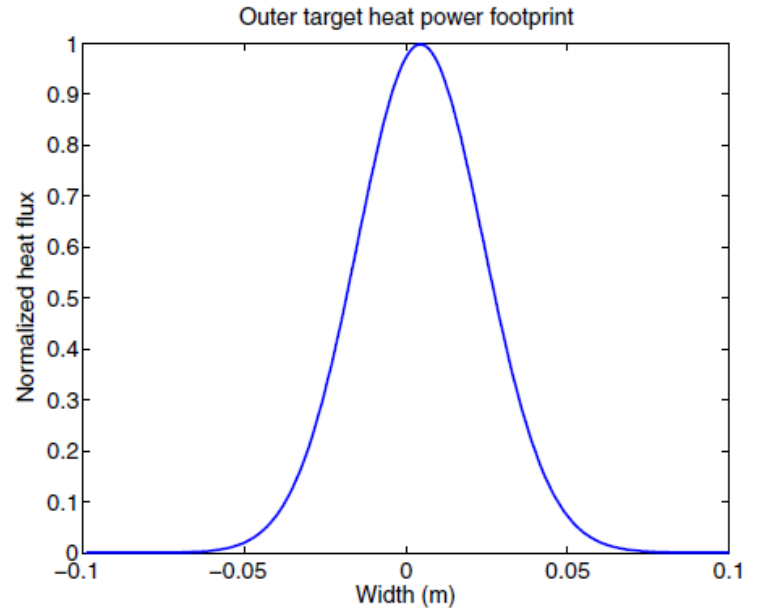


Figure 2.8: The assumed footprint of the head flux power on the outer target is according to the latest prediction for DEMO based on [7].

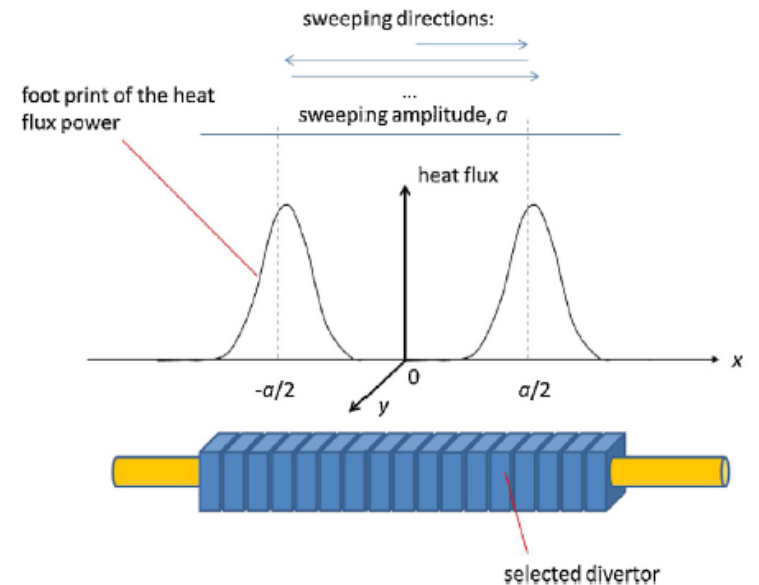


Figure 2.9: Schematic drawing of sweeping the footprint of the heat flux power [6].

Peak heat flux density (MW/m ²)	15			20			30			
	Sweeping frequency (Hz)	0°	0.5	1	0°	0.5	1	0°	0.5	1
Sweeping amplitude (cm)										
5	25.4 [302]	20.6 [297]	18.2 [295]	-	-	24.8 [300]	-	-	-	-
20		8.6 [262]	6.0 [243]		11.3 [280]	7.8 [257]		19.0 [295]	11.6 [281]	

Figure 2.10: Table with local maximum heat flux density (MW/m²) at the inner wall of the cooling tube (at node3) [6].

In this section are applied peak heat flux densities of 15 MW/m², 20 MW/m² and 30 MW/m². The sweeping amplitudes of 5 cm and 20 cm are chosen. The sweeping frequency varies from 1 Hz to 0.5 Hz. To investigate also steady state sweeping control regime, two more simulations considering 10 MW/m² and 4 Hz are studied [6].

Fig. 2.11 shows the heat transfer coefficient between the inner wall of the cooling tube and the coolant water [20, 21].

Critical heat flux

Fig. 2.10 contains the table of the heat flux densities at copper alloy-water interface (node 3). The coolant loses heat removal capability when the heat flux to the coolant is above the critical value (25.3 MW/m²), which is not included in the simulations. The maximum heat flux density to the coolant can be reduced by a factor of 4 for the combination of sweeping amplitude and frequency 20 cm and 1 Hz. Damage induced by a sudden increase of the heat flux density is decreased due to reduction in loading time by sweeping [6].

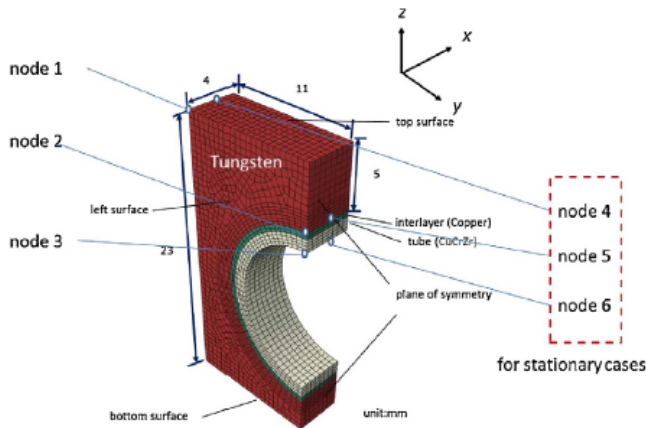


Figure 2.11: The FE mesh of the mono-block divertor model. Due to symmetry only the half of the structure was considered [6].

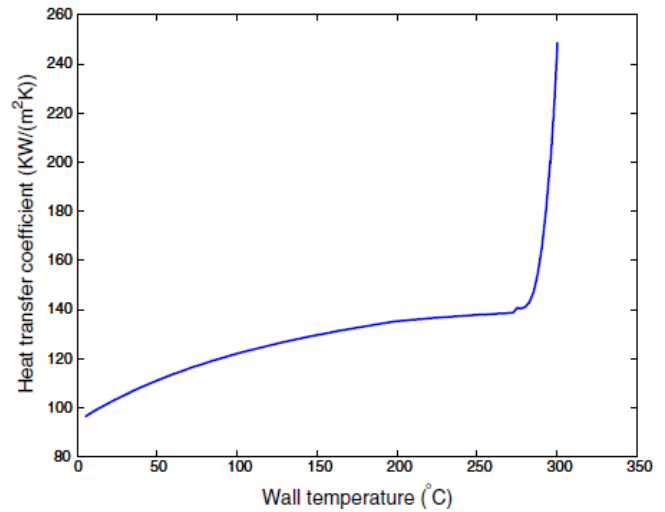


Figure 2.12: Heat transfer coefficient between the inner wall of the heat sink tube and the coolant water. The coolant water velocity is 12 m/s. Pressure of the coolant water is 5 MPa. The temperature of the coolant water is 200° [6].

Temperature

A characteristic temperature distribution of the divertor mono-block under high heat flux can be seen in Fig. 2.13. Temperature and heat flux density at node 1 as a function of time for a peak heat flux density 15 MW/m² with sweeping frequency and amplitude 1 Hz and 5 cm respectively is shown in fig. 2.14. The peak temperature

$\sim 1000^\circ$ is set after the second peak of the heat flux density. A thermal cycle with average temperature $\sim 800^\circ$ is saturated after a few seconds [6].

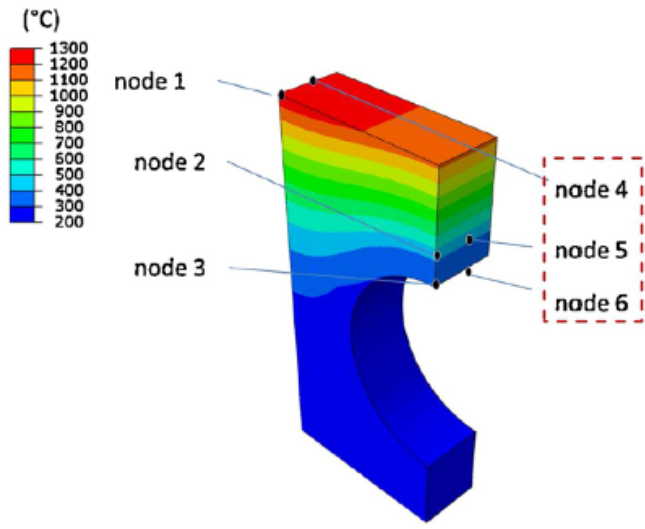


Figure 2.13: Temperature distribution for a stationary heat flux of 15 MW/m^2 with reference nodes [6].

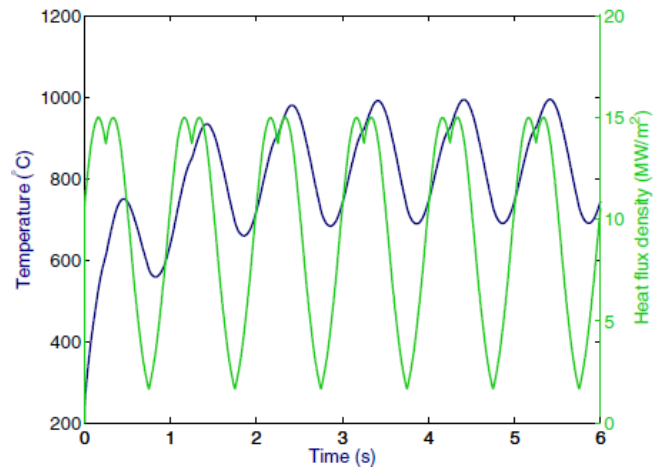


Figure 2.14: Temperature and heat flux density at node 1 as a function of time for a peak heat flux density 15 MW/m^2 with sweeping frequency of 1 Hz and sweeping amplitude of 5 cm [6].

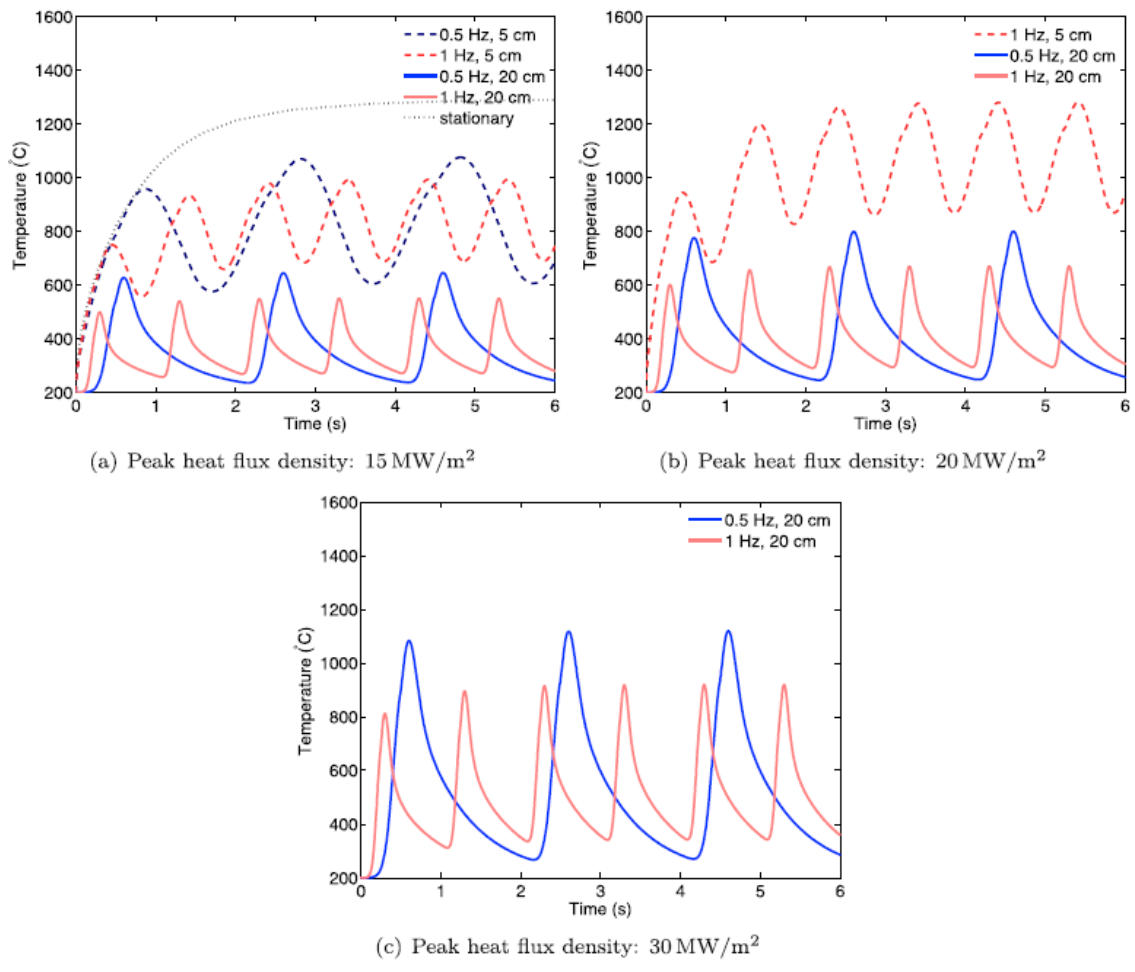


Figure 2.15: Temperature at node 1 as a function of time for different peak heat flux densities [6].

The temperature as a function of time at node 1 for three different peak heat flux densities 15 MW/m^2 , 20 MW/m^2 , 30 MW/m^2 can be seen in Fig. 2.15. The temperature is much lower for sweeping amplitude of 20 cm than 5 cm. The peak temperature declines with increasing sweeping frequency. The temperature variation and loading time in each thermal cycle are lower with higher sweeping frequency and lead to more load cycles of the divertor [6].

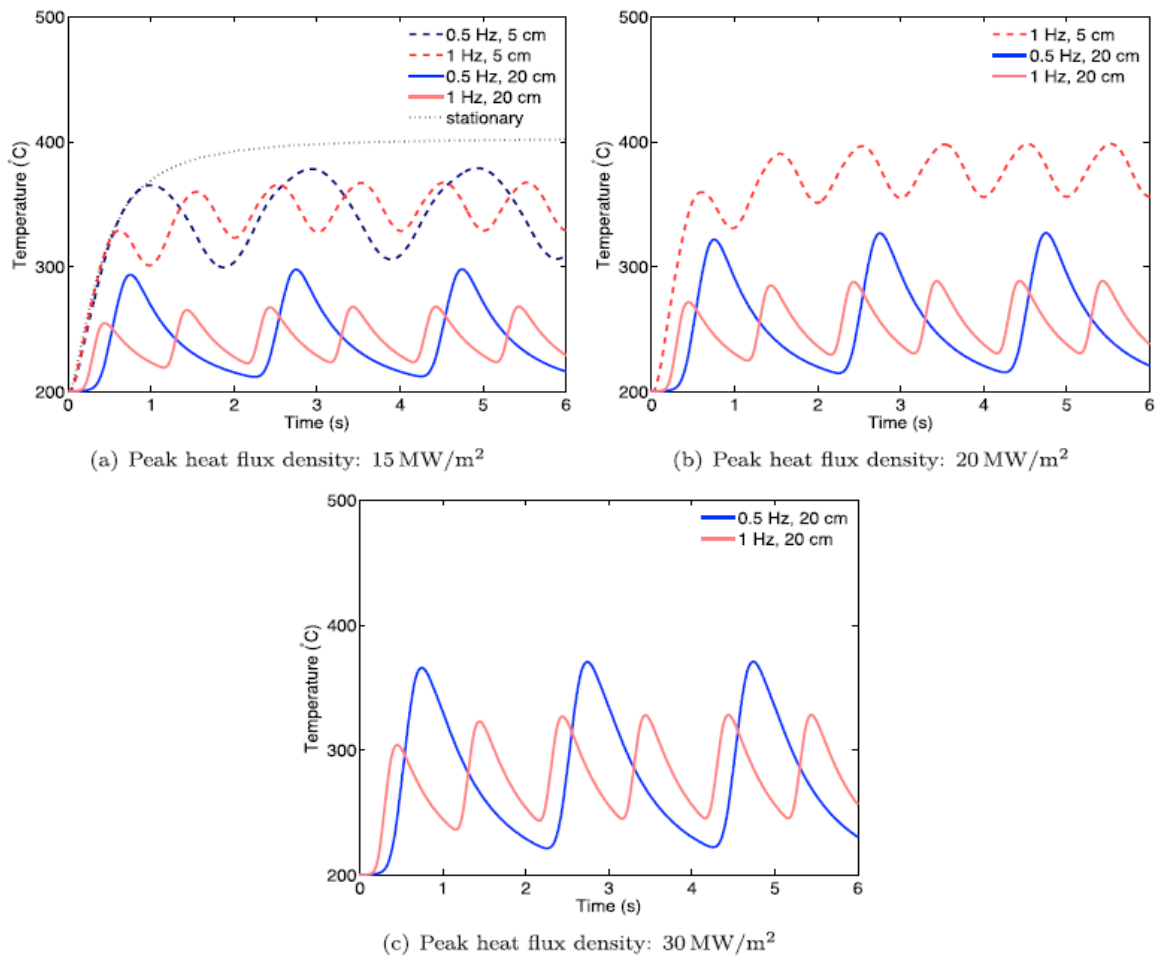


Figure 2.16: Temperature at node 2 as a function of time for different peak heat flux densities [6].

At node 2 for heat flux densities 15 MW/m^2 , 20 MW/m^2 , 30 MW/m^2 , the temperature dependence on the sweeping amplitude and frequency is similar as can be seen in fig. 2.16. uba

Summary

With increasing the sweeping amplitude or frequency, the maximum temperature and heat flux to the coolant decrease. Using optimal combination of sweeping amplitude and frequency, even the extreme heat flux load of 30 MW/m^2 is acceptable. Exceeding of the critical heat flux or armor melting point can be avoided. Using appropriate sweeping frequency and amplitude, this technique seems to be suitable as a steady state control scheme. Influence of the sweeping on the close surrounding by eddy currents induction or local equilibrium violation need also to be taken into account, but is not yet clear.

Chapter 3

ELM suppression and mitigation by fast swept magnetic coil on DEMO divertor targets

The concept of the ELM suppression and mitigation by sweeping the strike-point in space and time was briefly discussed in section 2.3. This chapter is dedicated to study the feasibility of this concept for future DEMO tokamak. Following sections contains description of coil set up, simulation of swept strike point and other aspects of this concept.

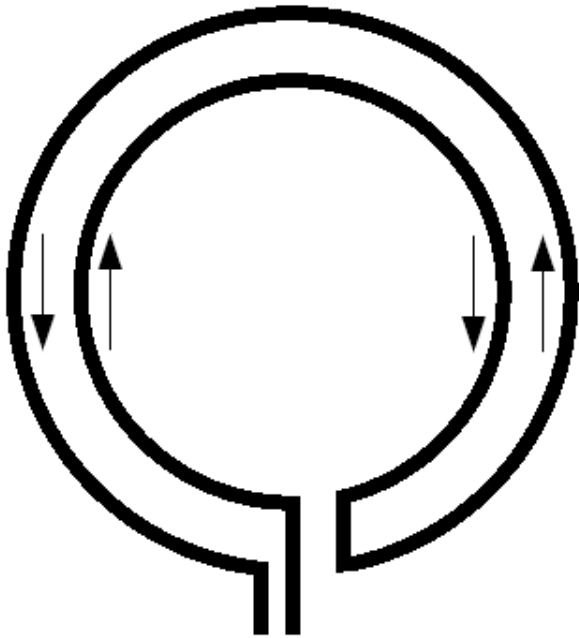


Figure 3.1: Twin coil located under the divertor cassettes and direction of a current running through the coils depicted by arrows.

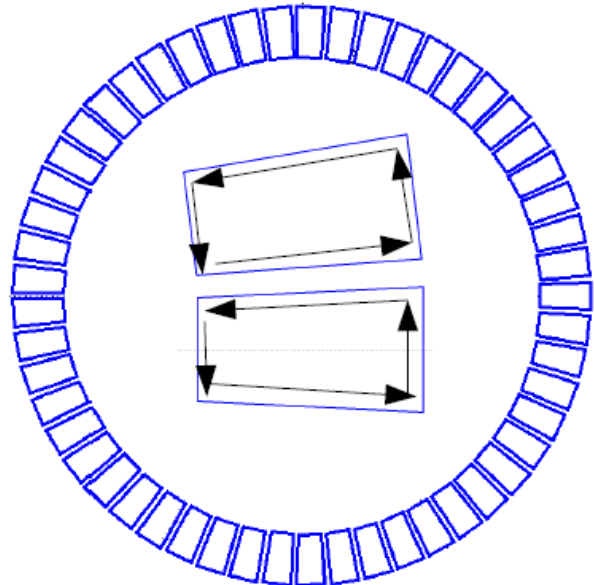


Figure 3.2: View from the top on 54 divertor cassettes and direction of a current running through the coils depicted by arrows.

3.1 Sweeping frequency

One of the key variables of the swept coil concept is a sweeping frequency f_{sweep} . f_{sweep} is a frequency of the strike point movement. Several coil configurations has been studied. All of them uses the same sweeping frequency $f_{sweep} = 2$ kHz. The reason for f_{sweep} to have such high value is that the ELM time in ITER has value $\tau_{ELM} \sim 0.4$ ms and in DEMO $\tau_{ELM} \sim 0.6$ ms. During τ_{ELM} , most of the ELM energy is deposited

on the divertor target. In order to suppress the heat loads with heat flux density $\varepsilon_{ELM} = 0.5 \text{ MJ/m}^2$, which is maximum acceptable power density in ITER, period of one sweep T_{sweep} needs to be lower or equal than τ_{ELM} . If T_{sweep} is higher than τ_{ELM} , even one unmitigated ELM has enough energy to exceed wolfram melting threshold. According to FIESTA, sweeping frequency $f_{sweep} = 2 \text{ kHz}$ is much higher than the DEMO vessel self-frequency $f_D = 9 \text{ Hz}$. Regardless of f_{sweep} value, coil generate eddy currents in the vacuum vessel. These currents attenuate magnetic field generated by the coil. If the coil was outside the vessel, coils magnetic field inside the vessel would be too weak for sweeping to be effective. Therefore coil needs be inside the vacuum vessel. Coil configurations with coils outside the vacuum vessel are not studied despite some advantages over the in vessel configurations.

3.2 Definition of the suppression factor

A suppression factor f_{SUP} is related with the ratio of the unmitigated ELM power density to the mitigated power density. Feasibility of the sweeping concept is dependent on its suppression factor. In our case, we define suppression factor f_{SUP} as a maximum of a ratio of a temperature of the non-swept strike point to the swept strike point during the sweeping. In this thesis, we try to achieve f_{SUP} high enough to avoid a recrystallization of the divertor target, which requires f_{SUP} to be $f_{SUP} = 4$.

3.3 Coil setup

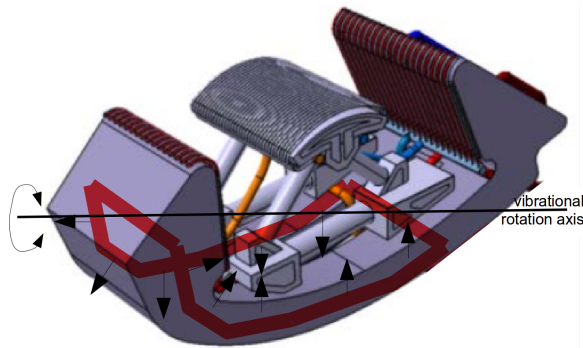


Figure 3.3: DEMO divertor cassette and 3D visualization of one coil inside the divertor cassette. Arrows depict $I \times B_t$ forces acting on coil.

3.3.1 Twin coil configuration

From an engineering point of view, the simplest coil configuration would be one coil with two opposite turns located under the divertor as can be seen in fig. 3.1. This configuration, called the twin coil configuration, has several advantages. First of them is its simplicity and toroidal symmetry. Second advantage is that the whole length of a coil actively sweeps the strike point. Therefore there are no useless parts except of coils connection. Coil under the divertor would be well shielded against the neutron flow. Disadvantage is that coil could not be removable. According to the simulation, current frequency $f_{sweep} = 2 \text{ kHz}$ and current amplitude $I_{sweep} = 130 \text{ kA}$ in twin coil, which are parameters needed for surface temperature suppression factor $f_{SUP} = 4$, would in coil with inductance $57.3 \mu\text{H}$ require 80 kV voltage. These is quite unrealistic requirement for power source. In order to decrease coils voltage, coil can be split into 54 segments, which is number of divertor cassettes that will be present in DEMO. This approach is studied in the following section.

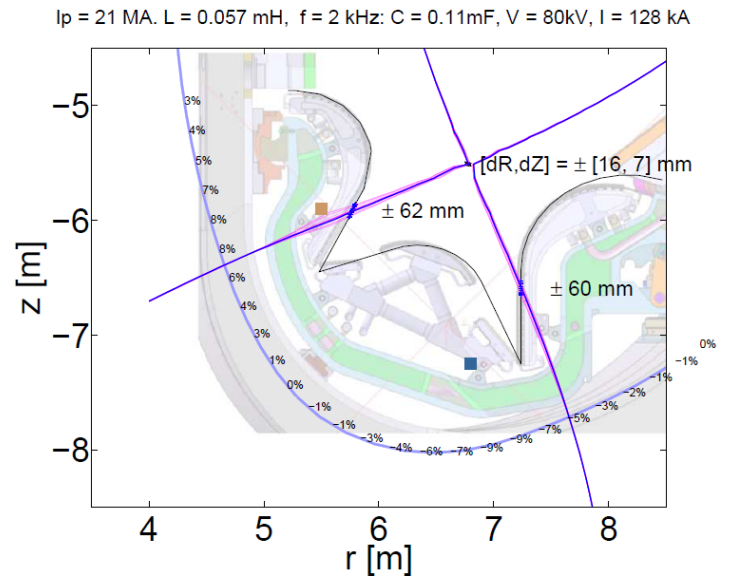


Figure 3.4: Dynamic FIESTA strike point sweeping simulation of the DEMO divertor including vessel currents [34].

3.3.2 Split coil configuration

Configuration composed of 54 divertor coils, so called split coil configuration, can be seen in the view from the top in fig. 3.2. By splitting the twin coil into 54 divertor coils, it is possible to decrease voltage and inductance by a factor of ~ 54 to acceptable levels of 1.5 kV and 1 μH for each divertor segment, while keeping coil current amplitude I_{sweep} constant. A dependence of coils inductance on the configuration and dimensions will be discussed more in 3.8. We suppose, that temperature suppression factor f_{SUP} for one twin coil with 80 kV voltage is the same as for 54 separated coils with 1.5 kV voltage each. Another advantage of splitting the coil into divertor cassettes is that coils are removable along with the cassettes. Divertor cassette with 3D visualization of the coil inside can be seen in fig. 3.3. This approach has also some disadvantages compared to one twin coil. For sweeping, radial parts of coils are obsolete because only toroidal parts has effect on the strike point movement in radial direction. Because of this, total coil length is ~ 3.8 times larger, which leads to higher ohmic losses and higher total mass. Radial parts not only make a coil longer, they are affected by large magnetic forces due to toroidal magnetic field, which will be more discussed in the section 3.13.1. By merging coils with divertor cassettes, coils will be closer to the plasma center, thus neutron irradiation will be higher in comparison with one twin coil under the divertor. This will be discussed in section 3.12.

Twin coil and split coil configuration are two basic coil setups studied in this chapter.

3.4 Simulation of the strike-point sweeping in DEMO tokamak

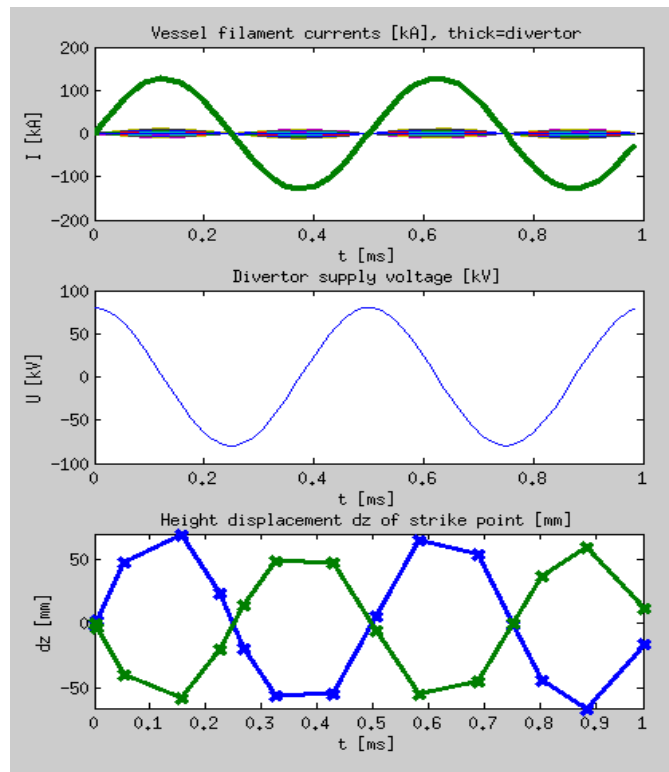


Figure 3.5: Result of the simulation of DEMO divertor in FIESTA [34]. Top: Twin coil current I_{sweep} (green) and vessel filament currents in vs. time t . Middle: Divertor supply voltage V_{sweep} vs. time t . Bottom: Height displacement dz of both strike points vs. time t .

The simulation of the swept strike point in FIESTA code is presented. In FIESTA, only toroidally symmetric configurations can be simulated, so simulation uses twin coil configuration. We assume, that splitting the coils and lowering voltage applied to each coil would have the same effect on strike point if split coils were on the same location. Therefore results are valid also for split coil configuration despite it is not directly simulated.

Result of dynamic fiesta strike point simulation is shown in fig. 3.4. Vessel shape used in simulation is shape of the COMPASS tokamak vessel rescaled for DEMO dimensions ($R_0 = 9$ m, $I_p = 21$ MA, $B_0 = 6$ T). Toroidal plasma current $I_p = 21$ MA, coil inductance $L = 57.3$ μH , alternating current frequency $f_{sweep} = 2$ kHz, coil

voltage $V_{sweep} = 80$ kV, coil current amplitude $I_{sweep} = \pm 127$ kA are parameters used in the simulation. For one twin coil mass $M = 1.4$ tons and coil resistivity $R_{\Omega} = 0.6$ m Ω . These parameters lead into ohmic losses $P_{\Omega} \sim 5$ MW. In split configuration, total mass $M = 5.3$ tons and mass of one divertor segment $m = 100$ kg. Each divertor segment would have resistivity $R_{\Omega} = 42$ $\mu\Omega$ and ohmic losses $P_{\Omega} = 29$ kW. One way to decrease P_{Ω} is by sweeping only during the ELM event for $2 \times \tau_{ELM} = \tau_{sweep} = 4$ ms. Time between two sweeps depends on ELM frequency. For $f_{ELM} = 20$ Hz this yields to waiting time 50 ms and ohmic losses $P_{\Omega} = 27$ kW for one divertor segment. Strike point position varies in time. Coordinates dR and dZ show its maximal spatial displacement $[dR, dZ] = \pm [16, 7]$ mm. Position of the divertor sweeping coil is shown by two squares in the divertor cassette. ITER divertor cassette is added just for illustration. Sweep amplitudes are $\lambda_S = 63$ mm for inner target and $\lambda_S = 64$ mm for outer target. Sweep amplitude is the length of an area on outer/inner target that is crossed with LCFS during whole sweeping period. Alternating divertor supply voltage can be seen in middle picture of fig. 3.5. Height displacement of both strike points can be seen in bottom picture in fig. 3.5. λ_S is higher when coil is closer to the X-point, but coil can not be too close because of neutron irradiation that will be present in DEMO. Precise location of coils will be dependent on DEMO divertor cassettes. Currents in

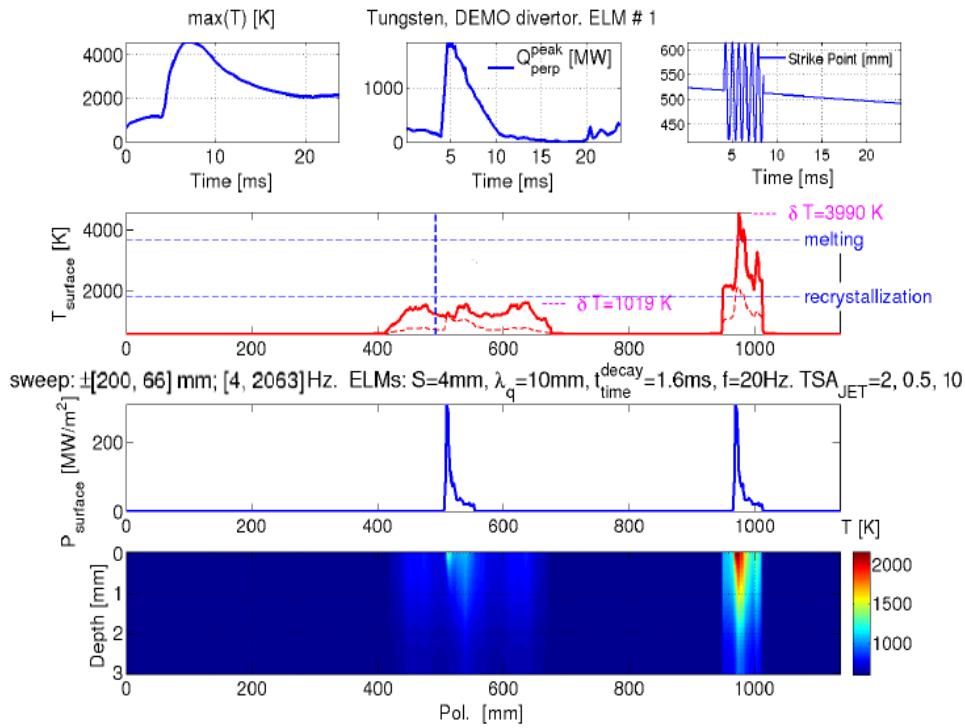


Figure 3.6: Heat conduction in DEMO tungsten divertor target. Top: Time evolutions: Left: surface temperature of non-swept strike point; Middle: Peak heat flux; Right: the swept strike point position. After 1 ELM, below is the actual surface temperature, heat flux and the in-depth temperature profile.

vessel generated by the coil are shown by percents in fig. 3.4. Their values mean percents of actual current in divertor coil. Currents in vessel including twin coil current (green) can be also seen in upper picture in fig. 3.5. Integral of these induced currents reaches values ~ 50 %. Advantage is that these currents attenuate magnetic field generated by coil, which is nearly zero around vessel. They damp $\sim 20\%$ of the strike point amplitude for given coil voltage. Field generated by coil has negligible effect on total plasma equilibrium. Furthermore currents in vessel slightly increase current in coil by few percent by common induction. Effect of sweeping on heat conduction and target temperature is discussed in next section.

3.5 2D heat conduction simulation

$$\tau_{ELM} = L_{\parallel} / c_{si} = L_{\parallel} / \sqrt{k_B T_e / m_i} \quad (3.1)$$

2D dynamic heat conduction simulation in MATLAB using real infrared data of large ELM fluxes on tokamak JET divertor target is presented. In order to simulate expected conditions on DEMO tokamak, this heat flux

needs to be rescaled in time and space to DEMO as such:

1. According to scaling in [26], we squeeze the radial power decay length λ_{int} down to 1/2 since $\lambda_{int}^{DEMO}/\lambda_{int}^{JET} \sim B_{pol}^{JET}/B_{pol}^{DEMO} \sim 1/2$.
2. According to [27], the time-scale τ_{ELM} is determined principally by the ion free-streaming time c_{si} by equation 3.1, where L_{\parallel} is connection length, k_B is Boltzman constant, m_i is ion mass and T_e is pedestal electron temperature. Therefore the time scale can be roughly estimated to be longer by factor of $\tau_{ELM}^{DEMO}/\tau_{ELM}^{JET} = L_{\parallel}^{DEMO}/L_{\parallel}^{JET} \times (T_{pedestal}^{JET}/T_{pedestal}^{DEMO})^{1/2} \sim (3:1) \times (1:6)^{1/2} = 1.2$.

Results of simulation of dynamic heat penetration after one ELM event are shown in fig. 3.6. Comparison between the swept strike point (left) and the not swept strike point (right) is presented. Upper left picture shows surface temperature vs. time of non-swept strike point. Upper middle picture shows peak heat flux vs. time. Temporal evolution of the swept strike point position is shown in upper right picture. Third picture from the bottom shows surface temperature distribution of swept and non swept strike points. Red solid line represents maximum temperature obtained in given location throughout whole ELM event. Dashed red line represents actual temperature. Two blue horizontal dashed lines correspond to recrystallization T_{rec} and melting T_{melt} temperatures. Swept strike point reaches $4\times$ lower surface temperature than non swept strike point. Non swept strike point temperature exceeds T_{melt} just after one ELM event. This would lead to wolfram melting and evaporation which is not included in the model, so wolfram exceeds T_{melt} without actual melting. Inclusion of wolfram melting into the model is not important, since it is essential to show that without sweeping wolfram exceeds T_{melt} , which alone is unacceptable. In contrast, swept strike point after one ELM event does not even exceed T_{rec} . Not only maximum wolfram surface temperature is important. Temperature gradients and cyclic stress are also crucial for divertor targets life time. Spatial surface power density is shown in second picture

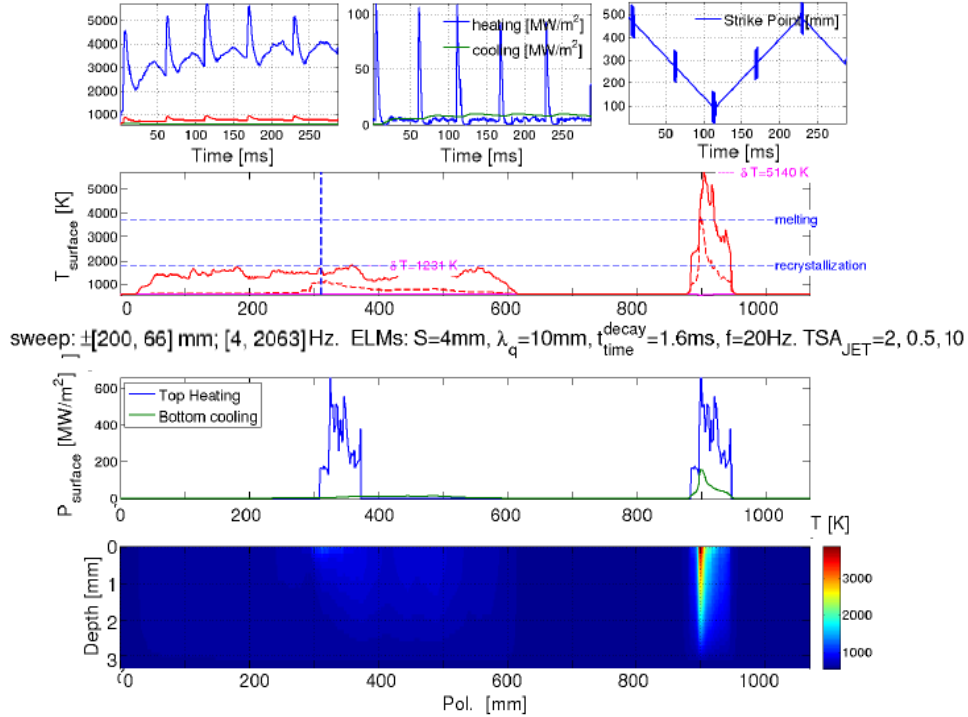


Figure 3.7: Heat conduction in DEMO tungsten divertor target. Top: Time evolutions: Left: surface temperature of non-swept strike point; Middle: Peak heat flux; Right: the swept strike point position. After multiple ELMs, below is the actual surface temperature, heat flux and the in-depth temperature profile.

from the bottom. It is the same for both the swept and the non swept strike point. Picture in the bottom shows 2D heat penetration into the divertor target for the swept strike point (left) and the non swept strike point (right). This configuration is toroidally symmetric, so only poloidal and radial coordinates are taken into account. Fig. 3.7 shows results of simulation of dynamic heat penetration after multiple ELM events. Upper left picture shows surface temperature vs. time of the non-swept strike point (blue) and the swept strike point (red).

Upper middle picture shows peak heat flux power density (blue) and cooling power density (green) vs. time. Although the inter-ELM heat flux is much lower than the ELM heat flux, the surface temperature would keep rising after the ELM event if the inter-ELM load would not be swept too. The inter-ELM heat flux can be swept by additional much slower sweeping ~ 4 Hz performed by the external superconductive coils. This additional slow sweeping can be seen in upper right picture along with fast sweeping during each ELM event. Thanks to this slow sweeping, average temperatures of both strike points saturate and stop rising after few ELM events as can be seen in upper left picture. Third picture from the bottom shows surface temperature distribution of the swept and the non swept strike points. It is important, that the swept strike point temperature does not exceed T_{rec} even after multiple ELM events. The non swept strike point temperature exceeds T_{melt} by ~ 1500 K. Second picture from the bottom shows spatial distribution of surface power density and cooling power density for both strike points. It is important to take cooling into account after multiple ELM events, because the heat would otherwise cumulate in target, which has limited heat capacity. From comparison of bottom picture 3.6 with bottom picture 3.7, in 3.6 it can be seen, that cooling has effect on lower part of the target.

3.6 Coil electrical scheme and triggering

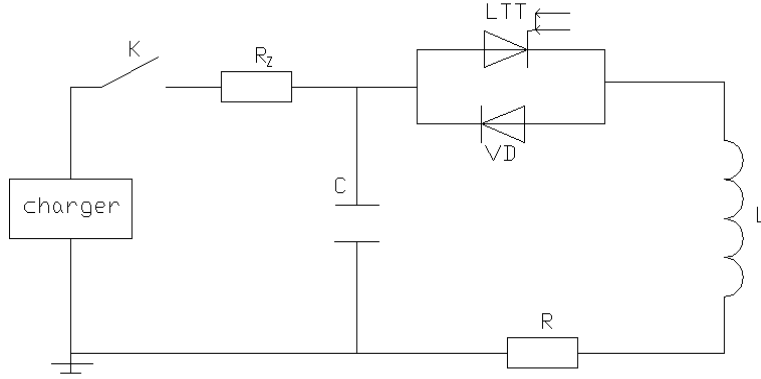


Figure 3.8: Resonant circuit for coil in one divertor cassette.

Fig. 3.8 shows resonant circuit for one coil in the divertor cassette. Coil inductance has value $L \sim 1\mu H$. Frequency used in simulation $f_{sweep} = 2$ kHz. In order to keep circuit in resonance, this yields to capacitors capacitance $C = 6$ mF. Voltage and current pulse shapes in two subsequent ELMs can be seen in fig. 3.9. Current pulse shape also corresponds to the strike point position. Period between two sweep events, which is normally ~ 10 times longer than sweep event, is shortened for better visualization. As discussed in 3.4, continuous sweeping would yield into larger ohmic losses, so each sweep event is only $\tau_{sweep} = 2 \times \tau_{ELM} = 4$ ms long. On the one hand τ_{sweep} is long enough for suppression factor $f_{SUP} = 4$, on the other hand τ_{sweep} is short enough so that ohmic losses are significantly reduced in comparison with continuous sweeping. Another important advantage

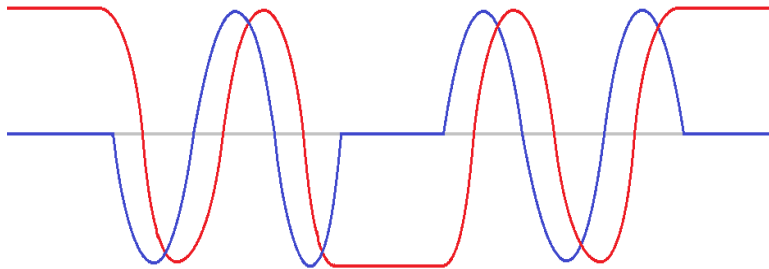


Figure 3.9: Voltage (red) and current (blue) pulse shape in two subsequent ELMs. Current shape also corresponds to the strike point position.

of non-continuous sweeping is that during this inter-ELM period, capacitors are recharged. During 4 ms long sweep event strike point performs $f_{sweep} \times \tau_{sweep} = 8$ sweeps. Because sweeping is not continuous, it is crucial to trigger sweeps at the right moment in order to spread the power load over a larger area effectively. Each

sweep event starts with maximum voltage with sign opposite than in previous event. Maximum voltage yields in maximum sweeping velocity at the start of the sweep. After the ELM time $\tau_{ELM} \sim 390 \mu\text{s}$ target temperature reaches maximum value, so triggering speed need to be shorter than τ_{ELM} . The best way to trigger sweeps is probably use of Langmuir probes for signal detection. Large current generated by ELM crash could be used to trigger ELMs after $\sim 0.1 \text{ ms}$ which is before ELM heat flux reaches maximum.

As electronic switch in each divertors coil RLC circuit can be used *insulated gate bipolar transistor* (IGBT). IGBT transistor provide maximal voltage up to 1.5 kV, which is value needed for suppression factor $f_{SUP} = 4$. Its maximal current has value 3.6 kA with 1 ms repetition rate. In order to achieve coil current $I_c = 130 \text{ kA}$, $130 \text{ kA} / 3.6 \text{ kA} = 36$ IGBT transistors need to be connected in parallel for each divertor cassette.

3.7 Skin effect

Sweeping the divertor target is done in high frequency alternating current regime. Therefore skin effect needs to be taken into account.

$$\delta = \sqrt{\frac{\rho_r}{\pi f \mu_r}} \quad (3.2)$$

Using equation 3.2, for alternating current frequency $f_{sweep} = 2 \text{ kHz}$ in copper conductor, skin effect depth is only $\delta = 1.5 \text{ mm}$. ρ_r and μ_r are copper resistivity and relative permeability. Since δ is so small, it would be useless to use full copper conductor. One option to avoid skin effect is to use hollow coils with thickness $d =$

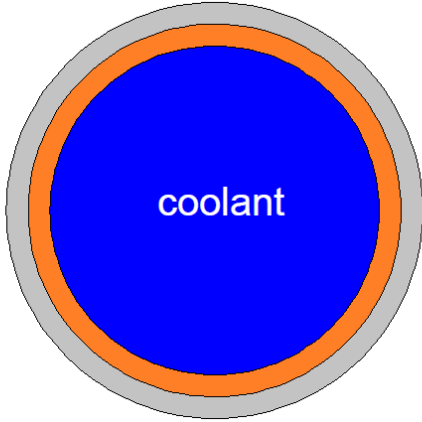


Figure 3.10: Divertor coil cross section. Insulation layer around copper pipe. Inside the pipe is coolant.

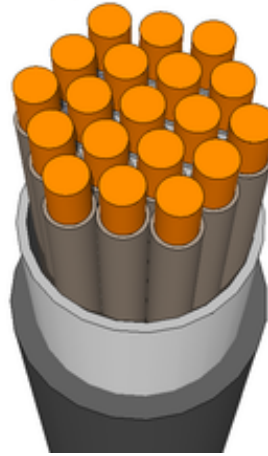


Figure 3.11: Litz wire.

1.5 mm filled with coolant as can be seen in fig. 3.10. As an insulation layer around the pipe could be used few mm teflon layer with dielectric strength 60 kV/mm. Advantage of this approach is a large cooling channel inside the coil, which would effectively cool down the coil. Disadvantage is that in order to have low resistivity, coil would have to be too big. Even with 10 cm radius, coil would have resistivity $R_\Omega = 0.1 \text{ m}\Omega$.

n\D [cm]	5	10	15	20	25
1	48.8	14.0	8.1	5.7	4.4
2	24.4	7.0	4.1	2.9	2.2
3	16.3	4.7	2.7	1.9	1.5
4	12.2	3.5	2.0	1.4	1.1
5	9.8	2.8	1.6	1.1	0.9
10	4.9	1.4	0.8	0.6	0.4
15	3.3	0.9	0.5	0.4	0.3
20	2.4	0.7	0.4	0.3	0.2

Table 3.1: Coil resistivity R_Ω [$\mu\Omega$] with proportional dependence coil diameter D and number of coil turns n . connected in parallel.

Another option to decrease the conductor impedance even more is to use multiple small wires isolated from each other rather than one solid wire. This type of wire is called Litz wire, as can be seen in fig. 3.11. Litz wire has much higher effective conductor surface in comparison with normal wire, since in full conductor, current is conducted only on the surface due to skin effect. For skin depth $\delta = 1.5$ mm, 3 mm diameter of each wire is reasonable. 0.5 mm width of the isolation layer is enough for 3 mm thick wire.

One coil turn has length $l \approx 5.5$ m which is given by divertor segment dimensions. In order to achieve low resistivity of each divertor coil, which is important mainly due to lower current and voltage amplitude dump in time, coil diameter D and number of coil turns n need to be chosen properly. Effective coil thickness $d = 1.5$ mm. Higher thickness is useless for such small skin depth.

Table 3.1 shows resistivity depending on number of coil turns and coil diameter. Resistivity is inversely proportional to number of coil turns connected in parallel n and coil diameter D , but total coil mass and volume occupied by coil are proportional to n and D . Since divertors toroidal dimension is ~ 0.7 m, it is reasonable to pose upper limit on coil total diameter to be 10 cm. This pose some limit to n , D and R_Ω . This will be more discussed in section 3.14.

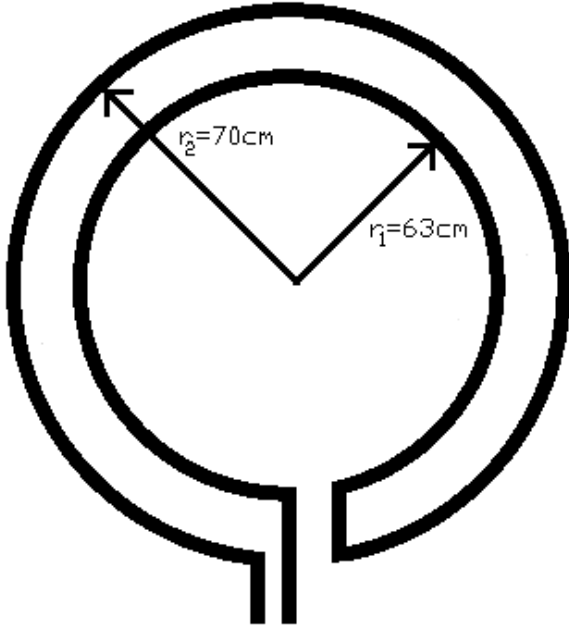


Figure 3.12: Twin coil configuration for measurement of inductance. Inner radius $r_1 = 63$ cm. Outer radius $r_2 = 70$ cm.

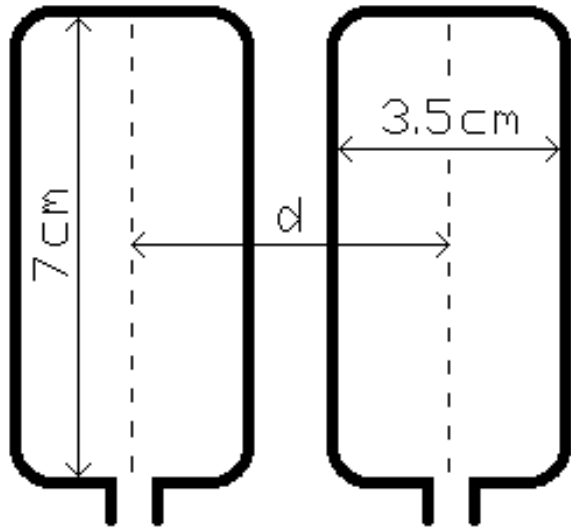


Figure 3.13: Split coil configuration for measuring inductance. Toroidal dimension 3.5 cm, radial dimension 7 cm and distance between two neighboring coils d .

3.8 Coil inductance

Based on FIESTA simulation, twin coil configuration described in section 3.3 and shown in fig. 3.1 has inductance $L = 57.3 \mu\text{H}$. This value is valid if DEMO dimensions, coil location as in fig. 3.4 and copper material with square cross section of 0.1 m^2 are assumed. As discussed in section 3.3, we assume that using split coil configuration shown in fig. 3.2, hence splitting the coil into 54 divertor segments while keeping the same position in space, coil cross section and material would yield into one divertor coil inductance of $\sim 1 \mu\text{H}$. Total inductance of all 54 segments would be changed by two effects. The first is the fact that total coil length of split coil configuration is ~ 2.8 times higher, than in twin coil configuration. The second effect is the fact that inductance of each coil will be affected by mutual inductance with surrounding coils. Currents in neighboring coils run in opposite directions, which will probably lower total inductance. Since FIESTA can calculate only toroidally symmetric configurations, we do not know inductance of split coil configuration. In order to compare FIESTA value with measured value of small twin coil, test change of inductance by splitting the coil and how much is inductance affected by mutual induction, simple experiment to measure inductance of one small twin coil and then multiple small (3.5×7 cm) coils in several setups was done.

3.8.1 Measurement of coil inductance in multiple coil setups

Twin coil configuration

In order to measure how much is inductance changed by splitting the coil into multiple smaller coils, it is reasonable to measure inductance in both configurations. First was measured inductance in twin coil configuration, which can be seen in fig. 3.12.

One copper coil with thickness of 2 mm, total length of 5.5 m, inner radius of $r_1 = 63$ cm and outer radius $r_2 = 70$ was used. Total coil length is 1/14 of length of DEMO divertor twin coil in FIESTA simulation shown in fig. 3.5. Its inductance was measured using multimeter with 1 kHz alternating current frequency. In this measurement, coils inductance is coupled with multimeter inductance, which is non-zero. Multimeter with supply cables has inductance $L_m = 0.3 \mu\text{H}$. Since multimeter is in series with the coil, its inductance can be simply subtracted, assuming small mutual inductance. Total inductance of multimeter and coil has value of $L_t = 4.9 \mu\text{H}$. Subtracting multimeter inductance we get value $L_{twin} = 4.6 \mu\text{H}$.

n [-]	N [-]	d [cm]	current direction	L_t [μH]	L_m [μH]	L [μH]	$L/N^2/n$ [μH]
1	1	-	-	0.4	0.3	0.1	0.10
1	4	-	-	1.9	0.3	1.6	0.10
1	4	-	-	2.7	1.2	1.5	0.09
1	8	-	-	6.6	1.2	5.4	0.08
1	12	-	-	11.7	1.2	10.5	0.07
2	4	4	anti-parallel	4.5	1.6	2.9	0.09
2	4	4	parallel	4.6	1.6	4	0.13
2	4	10	anti-parallel	4.8	1.6	4.2	0.13
2	4	10	parallel	4.7	1.6	4.1	0.13
3	4	4	anti-parallel	5.4	1.2	4.2	0.09
3	4	10	anti-parallel	7.5	1.7	5.8	0.12
3	4	20	anti-parallel	7.8	2.5	5.3	0.11
3	4	4	parallel	7.8	1.6	6.2	0.13

Table 3.2: Number of 7×3.5 cm rectangular coils n , number of each coil turns N , distance between each coil d [cm], direction of current in each neighboring coils, total coils inductance L_t [μH], inductance of multimeter and its supply cables L_m [μH], inductance of coils without multimeter L [μH], inductance of one turn of coil $L/N^2/n$ [μH].

Split coil configuration

Inner circumference of twin coil shown in fig. 3.12 has value ~ 2 m. $1/54$ of 2 m yields ~ 3.7 cm. In order to replace twin coil with 54 coils, each coils toroidal dimension of 3.5 cm is appropriate. For measurement was used only three coils, since mutual induction of distant coils is probably negligible. This assumption is valid according to results. Radial dimension of 7 cm is the same as difference between twin coils outer and inner radius. Coils has rectangular shape as can be seen in fig. 3.13. Distance between two neighboring coils d has value of $d \sim 4$ cm, if coils are right next to each other. Since coil inductance depends quadratically on number of turns, by increasing turns from 1 to 4, 8 and 12, inductance is increased by a factor of 16, 64 and 144. This is useful, since inductance of one turn coil with dimensions of 7×3.5 is lower than inductance of multimeter, which can affect the measurement.

Table 3.2 shows dependence of one turn coil inductance $L/N^2/n$ on number of coils n , number of coil turns N , distance between each coil d , direction of current in each neighboring coils, total inductance L_t of coils and multimeter and inductance of multimeter and its supply cables L_m . Direction of current in each two neighboring

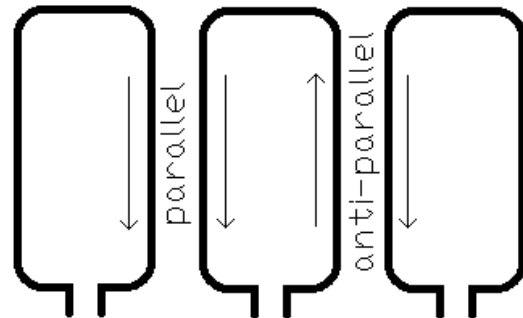


Figure 3.14: Three neighboring coils. Current runs parallel in left and middle coil and anti-parallel in middle and right coil.

coils can be parallel or anti-parallel as can be seen in fig. 3.14. Parallel means that in one coil current runs clockwise and in the other one current runs anti-clockwise. In all cases, multimeter and all coils are connected electrically in series. Multimeter inductance was measured in all setups separately, since it depended on exact position of supply cables and loops created by them.

Effect of mutual induction depends on neighboring coils current direction and distance between coils. Equation 3.3 shows dependence of total inductance of two coils electrically in series and their mutual inductance M .

$$L_T = L_1 + L_2 \pm 2M \quad (3.3)$$

In parallel coil configuration, contribution of mutual induction is positive, in anti-parallel configuration is contribution negative. Mutual inductance is given by equation 3.4. k_M is coupling coefficient with values in interval (0,1), which depends on coils mutual distance and position in space. k_M is zero, when coils are not coupled and current flowing through one coil does not induce current in the other one. k_M is one if magnetic flux generated by one coil flows through the other coil without any leakage.

$$M = k_M \sqrt{L_1 L_2} \quad (3.4)$$

If the distance between the coils is higher than each coil's dimensions, k_M and M is small. In our case, where coils are next to each other, k_M is non-zero. From equation 3.3 it is possible to deduce a formula for computing mutual inductance of two coils.

$$M = (L_p - L_a)/4 \quad (3.5)$$

L_p is inductance of two parallel coils, L_a is inductance of two anti-parallel coils in the same coil setup. Inductance of each coil is then given as $L \pm M$ (plus in parallel, minus in anti-parallel configuration). In case of two coils with mutual distance $d = 10$ or 20 cm, mutual inductance is insignificant as can be seen in table 3.2. In case of two coils next to each other, difference between inductance in parallel configuration $L_p = 4 \mu\text{H}$ and inductance in anti-parallel configuration $L_a = 2.9 \mu\text{H}$ is significant. Mutual inductance given by equation 3.5 has value $0.275 \mu\text{H}$. Without mutual induction, each one of two coils has inductance $L = 1.73 \mu\text{H}$. Total mutual induction is 16 % of sum of both coils inductances.

In case of three coils with mutual distance $d = 4$ cm from each other, equation for mutual inductance is slightly different. If we neglect interaction between the left and the right coil, which is negligible since they are $d = 8$ cm from each other, mutual inductance is given by formula 3.6.

$$M = (L_p - L_a)/8 \quad (3.6)$$

In case of three coils with mutual distance $d = 4$ cm from each other, inductance in parallel configuration $L_p = 6.2 \mu\text{H}$, inductance in anti-parallel configuration $L_a = 4.2 \mu\text{H}$. Mutual inductance given by equation 3.5 has value $0.25 \mu\text{H}$. Inductance of left and right coil is then given as $L \pm M$. Inductance of middle coil is given as $L \pm 2M$ (plus in parallel, minus in anti-parallel configuration). Without mutual induction, each one of three coils has inductance $L = 1.73 \mu\text{H}$. Total mutual induction in three coils configuration is 19 % of sum of three coils inductances.

Inductance measured in twin coil configuration has value $L_{twin} = 4.6 \mu\text{H}$. L_{twin} divided by 54 yields into $L_{twin}/54 = 0.085 \mu\text{H}$. It can be seen, that this value is in good agreement with one turn coil inductance with values in range $0.08\text{--}0.13 \mu\text{H}$ measured in different coil setups. These are only approximate values. However assumption that dividing the twin coil into 54 divertor segments would lead into each segment inductance of $\sim 1/54$ looks to be valid.

3.9 Energy in coils

In order to choose appropriate power supply for divertor coils, it is important to know how much energy will their operation consume. There are several options to calculate total energy in electrical circuit shown in fig. 3.9.

$$E_{total} = \frac{1}{2}CU^2 = \frac{1}{2}LI^2 = \frac{1}{2\mu} \int_V B^2 dV \quad (3.7)$$

Total energy in circuit E_{total} can be calculated using equation 3.7. E_{total} is given by capacitance of the capacitor C and capacitor's voltage U . E_{total} can be also calculated by coil current I and its inductance L if a capacitor is fully discharged. Third option to express E_{total} is using magnetic field B generated by the coil in given volume where B is non zero.

3.9.1 Twin coil configuration

In twin coil configuration, coil has inductance $L = 57.3 \mu\text{H}$ and current amplitude $I = 130 \text{ kA}$. Using equation 3.7, this yield in total energy $E_{total} = 484 \text{ kJ}$. Since voltage has amplitude $U = 80 \text{ kV}$, capacitance needed to store this amount of energy $C = 0.15 \text{ mF}$.

3.9.2 Split coil configuration

In split coil configuration, current amplitude $I = 130 \text{ kA}$ and voltage amplitude $U = 1.5 \text{ kV}$ in each divertor coil. According to section 3.8, each coil has inductance $L \sim 1 \mu\text{H}$. Energy in one divertor coil $E = 8.5 \text{ kJ}$. Total energy in split coil configuration $E_{total} = 456 \text{ kJ}$. Capacitor for one divertor segment storing $E_{total} = 456 \text{ kJ}$ of energy has to have capacitance $C = 7.5 \text{ mF}$. As expected, total energy stored in capacitors is comparable in both concepts.

3.10 Capacitor energy storage

The divertor coils will function in surge-current mode with current amplitudes 130 kA and voltage amplitudes 1.5 kV with sinusoidal pulse shape. As power supply for divertor coils will be used capacitive energy storage (CES) with semiconductor switches.

Stored energy	Capacitance	Maximum voltage	Maximum current
64 kJ	400 μF	18 kV	60 kA

Table 3.3: Parameters of capacitor cell.

As can be seen in section 3.9, energy $E = 8.5 \text{ kJ}$, $U = 1.5 \text{ kV}$ and capacity $C = 7.5 \text{ mF}$ are parameters, which needs to fulfill each divertor coils CES. Capacitors with such parameters are available according to [28]. Such a capacitors parameters can be seen in table 3.3. The CES pulse forming networks could be realized in low-voltage single capacitor cell with resistivity around $1 \mu\Omega$ and inductance below $5 \mu\text{H}$. It is built by a scheme with an intermediate inductive storage L (divertor coil) and reverse diodes VD in opposite-parallel connection to the main discharge switch (Light triggered thyristors, LTT) as can be seen in fig. 3.8. This configuration provides the sinusoidal discharge current shape as well as the reliable control of transient process by LTT triggering.

3.11 Circuit quality

There are two basic types of RLC resonant circuits, parallel and series. In parallel resonant circuit, capacitor and coil are connected in parallel. In series circuit, capacitor and coil are connected in series. Circuit shown in fig. 3.8 is series RLC resonant circuit, since power source is disconnected during the sweeping. In such a circuit, it is useful to know how much of total energy stored in circuit is dissipated per one cycle. Ratio of energy stored in circuit to the power loss in one cycle is defined by circuit quality factor Q . In series RLC circuit, quality factor Q is given by equation 3.8.

$$Q = \frac{2\pi f_0 L}{R_\Omega} \quad (3.8)$$

f_0 is resonant frequency, in our case $f_0 = 2 \text{ kHz}$. L is coils inductance and R_Ω is ohmic resistivity of the circuit. Alternative definition of Q is the number of oscillations needed for a freely oscillating systems energy fall of to $e^{-2\pi}$ of its original energy. Therefore it is desirable to keep Q as high as possible. In order for the sweeping to be effective, sweeping amplitude should not fall after 4 ms of the sweeping below 20 % of its initial amplitude at the beginning of the sweeping. Dumping of the amplitude in time in percents is given by following equation 3.9.

$$A_{dump} = 100 \times (1 - \exp(-\frac{R_\Omega t}{L})) \quad (3.9)$$

3.11.1 Twin coil configuration

In twin coil configuration, total coil resistivity $R_\Omega = 0.6 \text{ m}\Omega$. Coils inductance $L = 57.3 \mu\text{H}$. Using equation 3.8, circuit has quality $Q = 1200$. Using equation 3.9, after 4 ms of sweeping, amplitude is dumped by $A_{dump}(4 \text{ ms}) = 4.1 \%$.

3.11.2 Split coil configuration

In split coil configuration, resistivity of one divertor coil $R_{\Omega} = 40 \mu\Omega$ and inductance $L = 1 \mu\text{H}$. Circuit has quality $Q = 314$. After 4 ms of sweeping, amplitude is dumped by $A_{dump}(4 \text{ ms}) = 15 \%$. In both configurations, amplitude dump is low enough after one 4 ms long sweep event.

3.12 Neutronic analysis

Since ITER and DEMO tokamaks will generate fusion power 500 MW and 2000 MW respectively, high neutron fluxes causing nuclear heating and irradiation damage need to be taken into account. According to [25], 2000 MW of fusion power in DEMO tokamak would correspond to a neutron production rate of $7 \times 10^{20} \text{ n/s}$. 3D neutronic calculations carried out in [25] using MCNP5 code and JEFF 3.2 nuclear data are presented in following subsections 3.12.1 and 3.12.2.

3.12.1 Nuclear heating

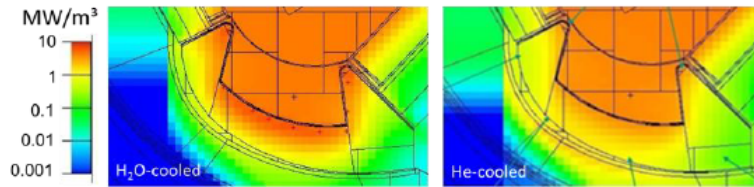


Figure 3.15: The spatial distributions of nuclear heating density in the EUROFER DEMO divertor cassette (left: water-cooled, right: helium-cooled) [25].

High neutron fluxes in DEMO tokamak will significantly heat up the vessel and all components that are not shielded from the neutron flux. In split coil configuration ohmic losses will heat up divertor coils with heating power up to $P_{ohm} \sim 1.5 \text{ MW}$ for all 54 divertor segments altogether and $P_{ohm} \sim 29 \text{ kW}$ for one divertor segment. Therefore it is relevant to compare this heating power with nuclear heating power [25].

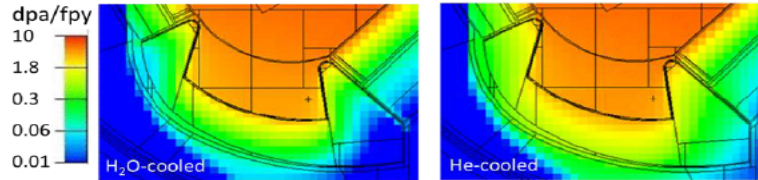


Figure 3.16: The spatial distribution of irradiation damage rate (dpa per fpy) in the DEMO divertor (left: water-cooled, right: helium-cooled) [25].

Fig. 3.15 shows spatial distributions of nuclear heating density in the DEMO divertor. Left figure corresponds to nuclear heating density in water-cooled EUROFER divertor cassette. Right figure corresponds to nuclear heating density in helium-cooled EUROFER divertor cassette. These results are valid for EUROFER steel only. In case of copper, nuclear heating would be probably different, but those data are not available. From fig. 3.15 and coils position in divertor cassette depicted in 3.3 it can be roughly estimated that nuclear heating power density to have value $\sim 5 \text{ MW/m}^3$ in water cooled and $\sim 2 \text{ MW/m}^3$ in helium cooled divertor cassette. In case of one divertor coil with mass $m = 100 \text{ kg}$ and length of 5.5 m with 20 kg of water coolant positioned as in fig. 3.3, ohmic losses have value $P_{\Omega} \sim 29 \text{ kW}$. Radiation input power in such a coil $P_{nuc} \sim 100 \text{ kW}$, which is higher than P_{Ω} . Even if nuclear heating power density was lower than 5 MW/m^3 , radiation input power would be still comparable to ohmic losses [25].

3.12.2 Irradiation damage

Fig. 3.16 shows the spatial distribution of irradiation damage rate (displacement per atom per full power year) in the EUROFER divertor cassette for water-cooled (left) and helium-cooled (right) configurations. These

results are valid for EUROFER steel only. In case of copper, irradiation damage would be probably different, but those data are not available. From fig. 3.15 and coils position in divertor cassette depicted in 3.3 it can be roughly estimated, that coils would be in region with values of dpa ~ 2 in water cooled-case and dpa ~ 4 in helium-cooled case. There is a discussion about usage of copper material locations with high irradiation damage rate due to its activation. However copper is expected to be largely used in DEMO cassettes as the principle heat extraction material [25].

3.13 Electromagnetic force analysis

3.13.1 Mechanical vibrations

In radial parts of each coil, current flow in the direction perpendicular to the toroidal magnetic field. This results in large $I_{sweep} \times B_t$ force. In case of coil current amplitude $I_{sweep} = 130$ kA and toroidal magnetic field $B_t = 6$ T, resulting force $F = 800$ kN. Direction of the force acting on the coil is depicted by arrows in fig. 3.3. Because sweep events are only $\tau_{sweep} = 4$ ms long, the force acting on a 100 kg heavy coil with one turn shifts a coil only by 2 mm in vertical direction for each event. Shift is inversely proportional to the coil mass. In each coils radial part current flow in the opposite direction, as can be seen in fig. 3.2. Currents running in the opposite direction lead into repelling of neighboring coils radial parts from each other. This also means that force acting on the right side of each coil has opposite direction than the force acting on the left side of the same coil. If a coil was not rigidly attached, coil would rotate along its horizontal axis shown in fig. 3.3. Such a

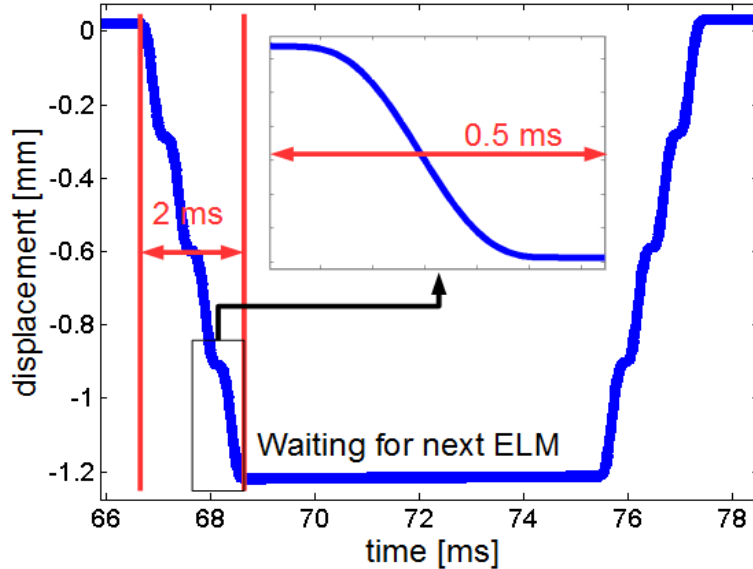


Figure 3.17: Displacement of the coil in time during two subsequent 2 ms long sweeps. Coil current $I = 130$ kA, coil mass $m = 100$ kg, toroidal magnetic field $B_t = 6$ T and resulting force $F = 800$ kN.

coil movement can be avoided by charging the capacitor bank with opposite sign voltage after each subsequent sweep event as shown in fig. 3.9. In this case, coil stays within 2 mm range during two subsequent ELM events. Vertical displacement of the coils radial part in 2 ms long sweeps can be seen in fig. 3.17. In $\tau_{sweep} = 4$ ms long sweep events, this effect would be two times larger than shown in fig. 3.17, which would yield in 2 mm displacement. Between two events, current in a coil is zero and coil do not move.

3.13.2 Vertical displacement events

Global plasma instabilities such as plasma disruptions and vertical displacement events (VDEs) induce large transient electric currents in conductive steel vessel and divertor cassette body. Disruptions induce eddy currents. VDEs create halo currents. These currents create through interaction with the toroidal magnetic field high Lorentz force as an impact load on the divertor cassette body and all of its components including potential divertor swept coil. Fig. 3.18 shows result of finite element method simulation of Lorentz force generated by halo currents in DEMO divertor cassette body. In the most critical case, halo currents are induced in radial

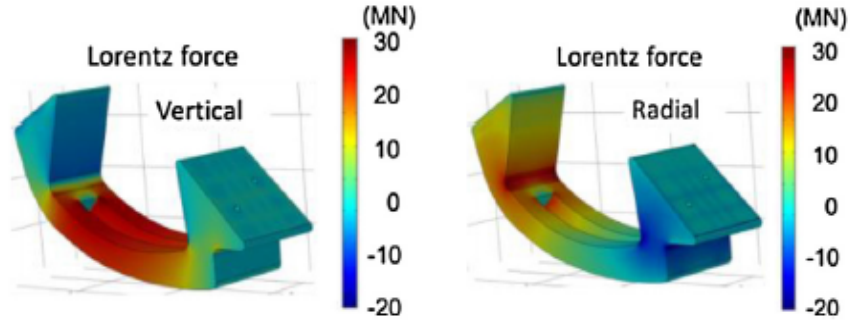


Figure 3.18: Induced Lorentz forces in the divertor cassette shell plate (left: vertical, right: radial component) [25].

direction with maximum current density of 2.2 MA/m^2 . In case of twin coil configuration, halo currents would not flow through the coil. However split coil positioned as in fig. 3.3 with low resistivity $R_\Omega < 0.1 \text{ m}\Omega$ would probably suffer from huge structural loads. This would be the case since its longest part is in the direction where halo current flows, which is perpendicular to the toroidal magnetic field. Structure in the fig. 3.18 is elastically deformed in the middle part up to 1.4 mm. Forces acting on the coil during VDE would be more than order of magnitude higher than forces causing mechanical vibrations discussed in section 3.13.1. Big force gradient between the coil central part and its ends would lead into vertical deformation which means, that coil would need to be rigidly attached to the cassette body.

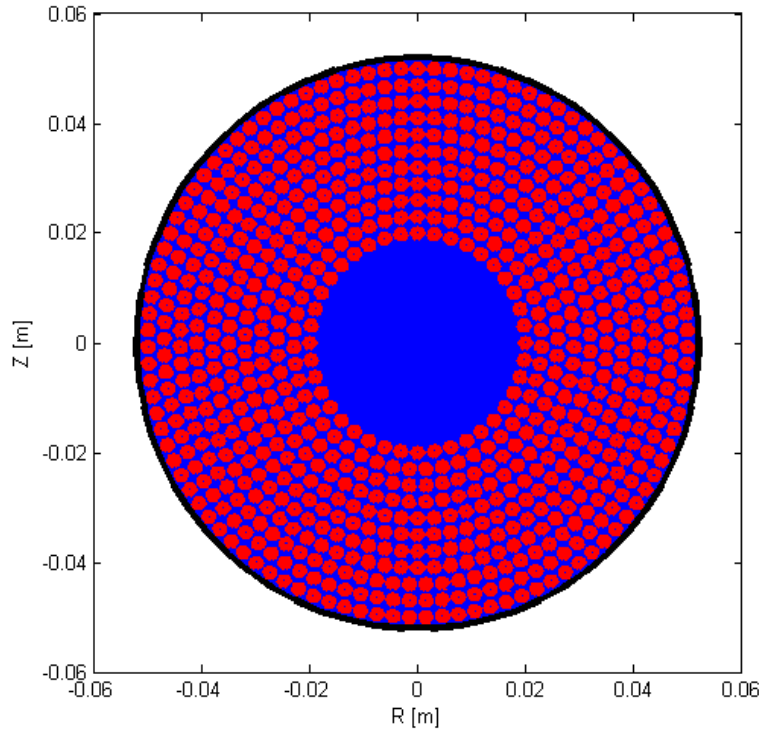


Figure 3.19: Cross section of the divertor coil with 801 wires each 3 mm thick. Coil has 5 cm radius. Inside the coil is cooling channel with 2 cm radius.

3.14 Coil design

There are many physical limitations on divertor coils given by number of coil turns, coil diameter, coil thickness, coil material and coil coolant. The first limit is the amount of space available in the divertor cassette. Second

limit is total mass of the coil. Resistivity limit is due to ohmic losses and circuit quality. If the resistivity is too big, amplitude dump after one 4 ms sweep event is too large. Heat losses are generated by ohmic losses and nuclear heating. These are basic limits posed on coil design. Next subsections describe a few different coil designs and how they fulfill those limits.

3.14.1 One turn Litz wire with cooling channel inside

One way to decrease coil occupied volume and resistivity is to use one turn of Litz wire with hundreds of 3 mm thick wires along with the cooling channel inside as can be seen in fig. 3.19. Table 3.4 shows dependence of cooling channel diameter d and diameter D on coil mass m_{coil} , mass of water m_{H2O} coolant, coil resistivity R_{Ω} , coil ohmic losses P_{Ω} , irradiation input power for coil with water coolant $P_{rad,H2O}$, circuit quality Q and amplitude dump after 4 ms of sweeping. Coils length has value ~ 5.5 m. Because of divertor toroidal dimension

d/D [cm/cm]	m_{coil} [kg]	m_{H2O} [kg]	R_{Ω} [$\mu\Omega$]	P_{Ω} [kW]	$P_{rad,H2O}$ [kW]	Q [-]	A_{dump} (4 ms) [%]
4/10	279	7	16	11	156	775	6
3/7	121	4	37	25.3	68	337	14
2/5	76	2	60	48.5	42	210	21

Table 3.4: Dependence of coil mass m_{coil} , mass of water m_{H2O} coolant, coil resistivity R_{Ω} , coil ohmic losses P_{Ω} , irradiation input power for coil with water coolant $P_{rad,H2O}$, circuit quality Q and amplitude dump after 4 ms of sweeping on cooling channel diameter d and coil diameter D .

has value ~ 70 cm, it is reasonable for coil diameter to not overreach value of ~ 10 cm. Therefore, only coil configurations with coil diameter ≤ 10 cm are taken into account. From table 3.4 it can be seen that mass of the water coolant is negligible in comparison with coil mass m_{coil} for such cooling pipe dimensions. The same is true in case of the helium coolant, which is even few orders of magnitude less heavy in such volumes. Therefore there is no limit on coolant mass. ITER divertor cassette has weight 10 t, so DEMO divertor cassette mass could be comparable. For this reason, one divertor coils mass should not probably exceed 200 kg. Ohmic losses P_{Ω} are comparable to irradiation power P_{rad} in the case of water coolant. As was discussed in the section 3.12.1, P_{rad} is only very rough estimate. However it shows, that decreasing coils resistivity and ohmic losses under some limit has no point since radiation input power would only increase with increasing amount of copper. Amplitude dump after 4 ms of sweeping A_{dump} (4 ms) should not be higher than 25 %. This would be the case if $R_{\Omega} < 70 \mu\Omega$ for $L = 1 \mu\text{H}$ and $f_{sweep} = 2$ kHz.

3.14.2 Four Litz wires each with cooling channel inside

Another way to decrease coil occupied volume and resistivity is to use four turns of Litz wire with hundreds of 3 mm thick wires along with the cooling channel inside each coil. This configuration can be seen in fig. 3.20. In this configuration, dependence of each coils cooling channel diameter d and diameter D on coil mass m_{coil} , mass of helium m_{He} or water m_{H2O} coolant, coil resistivity R_{Ω} , coil ohmic losses P_{Ω} , irradiation input power for coil with water $P_{rad,H2O}$ or helium coolant $P_{rad,He}$ can be seen in table 3.5. Coils length is the same as in previous configuration ~ 5.5 m.

d/D [cm/cm]	m_{coil} [kg]	m_{H2O} [kg]	R_{Ω} [$\mu\Omega$]	P_{Ω} [kW]	$P_{rad,H2O}$ [kW]	Q [-]	A_{dump} (4 ms) [%]
2/5	302	7	15	10.1	169	169	6
1.6/4	201	4	23	15.3	112	557	9
1/3	109	2	42	28.2	61	302	15

Table 3.5: Dependence of coil mass m_{coil} , mass of water m_{H2O} coolant, coil resistivity R_{Ω} , coil ohmic losses P_{Ω} , irradiation input power for coil with water coolant $P_{rad,H2O}$, circuit quality Q and amplitude dump after 4 ms of sweeping on cooling channel diameter d and coil diameter D .

3.14.3 Nine Litz wires each with cooling channel inside

Third option to decrease coil occupied volume and resistivity is to use nine turns of Litz wire with 3 mm thick wires with cooling channel inside each coil. This configuration can be seen in fig. 3.21. In this configuration,

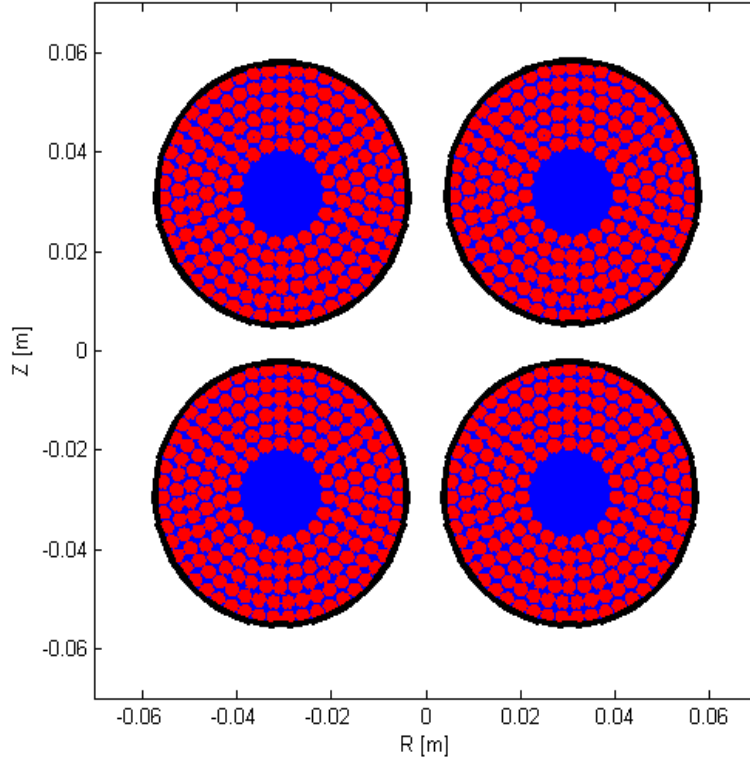


Figure 3.20: Cross section of the divertor coil with four turns, each has 217 wires 3 mm thick. Each coil has 2.5 cm radius. Inside each coil is cooling channel with 1 cm radius.

dependence of each coils cooling channel diameter d and diameter D on coil mass m_{coil} , mass of helium m_{He} or water m_{H2O} coolant, coil resistivity R_{Ω} , coil ohmic losses P_{Ω} , irradiation input power for coil with water $P_{rad,H2O}$ or helium coolant $P_{rad,He}$ can be seen in table 3.6.

d/D [cm/cm]	m_{coil} [kg]	m_{H2O} [kg]	R_{Ω} [$\mu\Omega$]	P_{Ω} [kW]	$P_{rad,H2O}$ [kW]	Q [-]	A_{dump} (4 ms) [%]
1.5/3	201	9	23	15.3	112	557	9
0.8/2.4	132	2	34	23.2	73	366	13
0.6/2.0	113	1	40	27.1	63	313	15

Table 3.6: Dependence of coil mass m_{coil} , mass of water m_{H2O} coolant, coil resistivity R_{Ω} , coil ohmic losses P_{Ω} , irradiation input power for coil with water coolant $P_{rad,H2O}$, circuit quality Q and amplitude dump after 4 ms of sweeping on cooling channel diameter d and coil diameter D .

3.15 Comparison of coil designs

All three coil designs in previous sections differing in the number of coil turns are subset of split coil configuration. Comparison between them can be seen in table 3.7. All three coil designs fulfill two basic conditions. The first is spatial condition, total diameter lower than 10 cm. The second condition is maximum mass to be lower than ~ 200 kg. All three coil designs do not differ in total resistivity R_{Ω} and ohmic losses P_{Ω} . In all three cases, amplitude dump after one 4 ms sweep event A_{dump} (4 ms) ≤ 15 %, which is acceptable. With increasing number of coil turns increase surface of contact of water coolant with the coil, which would probably lead into more effective cooling. However cooling capabilities and requirements are not discussed in this thesis. Based on values in table 3.7, all three coil designs are equivalent.

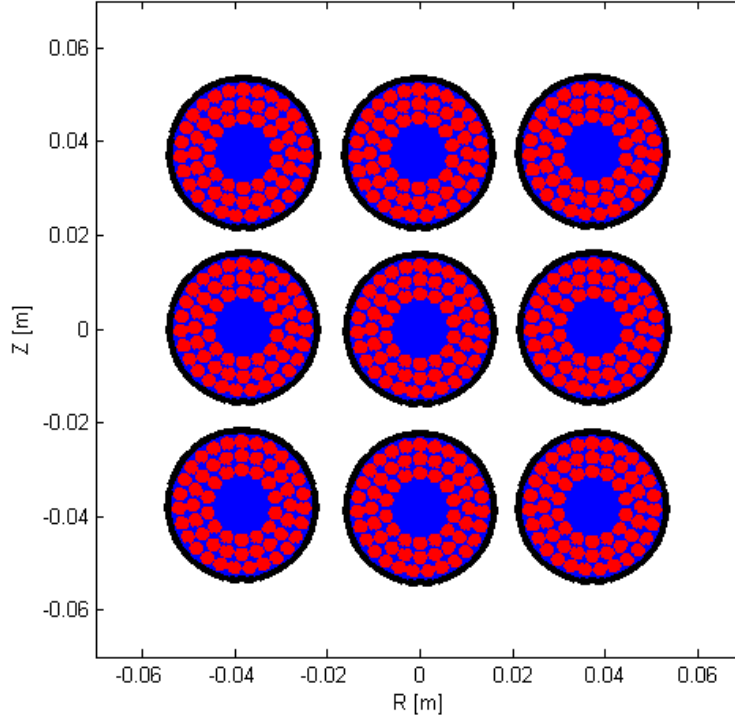


Figure 3.21: Cross section of the divertor coil with 9 turns, each has 64 wires 3 mm thick. Coil has 1.5 cm radius. Inside each coil is cooling channel with 0.75 radius.

n turns	d/D [cm/cm]	m_{coil} [kg]	R [$\mu\Omega$]	P_{Ω} [kW]	$P_{rad,H2O}$ [kW]	Q [k-]	A_{dump} (4 ms) [%]
1	3/7	121	37	25.3	68	337	14
4	1/3	109	42	28.2	61	302	15
9	0.8/2.4	132	40	27.1	63	313	15

Table 3.7: Dependence of coil mass m_{coil} , mass of water m_{H2O} coolant, coil resistivity R_{Ω} , coil ohmic losses P_{Ω} , irradiation input power for coil with water coolant $P_{rad,H2O}$, circuit quality Q and amplitude dump after 4 ms of sweeping on cooling channel diameter d , coil diameter D and number of coil turns for three coil configurations.

3.16 Scaling of suppression factor f_{SUP}

In order to test feasibility of this concept for different size machines and divertor coil parameters, f_{SUP} has been scaled using different scaling functions as can be seen in fig. 3.22. Suppression factor f_{SUP} is the maximum of the ratio of non swept target temperature T to swept target temperature T_{SUP} . f_{SUP} is also key variable defining significance of the whole divertor sweeping concept. The higher is the variable, the higher is the target temperature suppression during the sweeping. Unfortunately, f_{SUP} is limited by following parameters.

1. Maximum sweeping amplitude λ_{sweep} , which is proportional to the limited divertor coil current.
2. Sweeping frequency f_{sweep} , which is proportional to the limited voltage applied to each divertor coil.
3. Other parameters like integral power decay width λ_{int} and ELM time τ_{ELM} are given by main tokamak parameters and can be treated as constants for each machine.

f_{SUP} is proportional to sweeping amplitude λ_S , sweeping frequency f_{sweep} and ELM time τ_{ELM} and inversely proportional to integral power decay width λ_{int} . Following equations shows dependence of several scaling functions F_1 – F_4 on sweeping amplitude λ_S normalized to λ_{int} and sweeping frequency f_{sweep} normalized to τ_{ELM} .

$$R = \sqrt{1 - \frac{\sum_i (f_i - y_i)^2}{\sum_i (f_i - \bar{y})^2}} \quad (3.10)$$

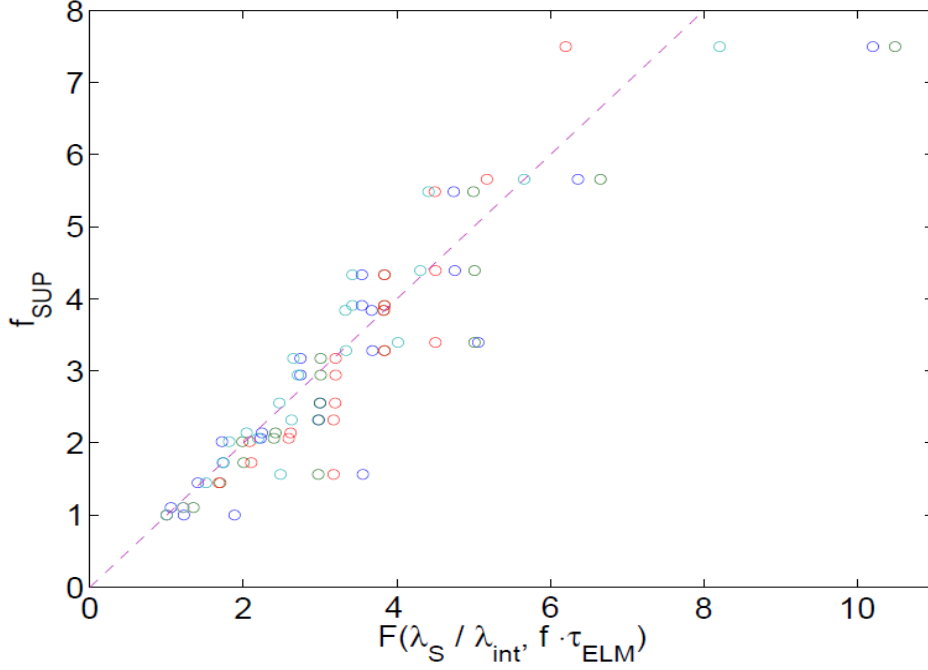


Figure 3.22: Scaling of suppression factor f_{SUP} using five different scaling functions F and f_{SUP} values from FIESTA [34]. F depends on sweeping amplitude λ_S normalized to integral power decay width λ_{int} and sweeping frequency normalized to ELM time τ_{ELM} . F_1 - blue, F_2 - green, F_3 - red, F_4 - cyan

$$F_1 = \sqrt{\left(1 + \frac{\lambda_S}{\lambda_{int}}\right)\left(1 + f_{sweep} \cdot \tau_{ELM}\right)/2} \quad (3.11)$$

$$F_2 = 1 + \sqrt{\frac{\lambda_S}{\lambda_{int}} f_{sweep} \cdot \tau_{ELM}/2} \quad (3.12)$$

$$F_3 = \log\left(\left(1 + \frac{\lambda_S}{\lambda_{int}}\right)\left(1 + f_{sweep} \cdot \tau_{ELM}\right)\right) \quad (3.13)$$

$$F_4 = 1 + 0.75 \log\left(1 + f_{sweep} \cdot \tau_{ELM}\right) \sqrt{\frac{\lambda_S}{\lambda_{int}}} \quad (3.14)$$

As can be seen in fig. 3.22, all four scalings give similar results for sweeping frequencies lower than 4 kHz and sweeping amplitudes in range $\lambda_S = 16$ –131 mm. They start to differ for higher values of f_{sweep} and λ_S . Residual coefficients calculated from equation 3.10 for each scaling are: $R_1 = 0.9015$, $R_2 = 0.9161$, $R_3 = 0.8886$, $R_4 = 0.9611$. y_i is i -th f_{SUP} , \bar{y} is average of all f_{SUP} values and f_i is i -th value of scaling function F . Since R_4 is the closest to 1, scaling equation F_4 seems to be the best scaling f_{SUP} values.

Scaling equations of f_{SUP} were derived, which is useful to test the feasibility of this concept for different machines even without any simulation.

Chapter 4

Feasibility study of ELM suppression and mitigation on COMPASS divertor targets

The COMPASS tokamak is a compact experimental device ($R_0 = 0.56$ m, $a = 0.23$ m, $I_p = 400$ kA, $B_0 = 0.9$ - 2.1 T) operated in a divertor plasma configuration having ITER-like plasma cross-section with 1:10 in linear dimension. It can operate in H-mode with both Type-III and Type-I ELMs. First section contains simple experiment to test RLC circuit. Subsequent sections contains informations about ELMs on COMPASS, suppression factor estimation and discussion about feasibility of the sweeping concept on tokamak COMPASS.

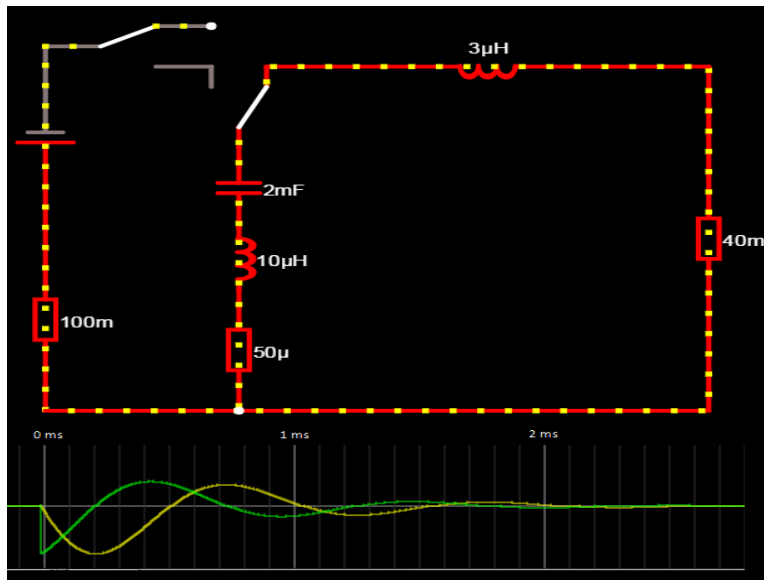


Figure 4.1: RLC circuit simulation done using [31]. Voltage (green) and current (yellow) vs. time.

4.1 RLC circuit

On tokamak COMPASS, swept coil could be installed in twin coil configuration, which means two turns in the opposite direction under the divertor on radial distance $R = 0.4/0.5$ cm respectively. Current and voltage has been measured to test RLC circuit parameters in such a configuration using copper coil with diameter 1.5 mm. RLC circuit scheme can be seen in fig. 4.1. Old CASTOR capacitor with parameters $C = 2$ mF, $L = 10$ μH, $R < 50$ μΩ was used. Coil with such a dimensions has inductance $L \sim 3$ μH. Two different switches were used. Capacitor was first charged by a power source. Than (left) switch connecting power source and capacitor was turned off. Circuit was set to resonance after turning on second (right) switch. Fig. 4.1 also shows simulation of current and voltage vs. time. Circuits resonant frequency $f = 1$ kHz. Capacitor was charged up at two different voltage values $U = -60$ V/-150 V. Higher values could destroy the switch. Current amplitude in simulation has

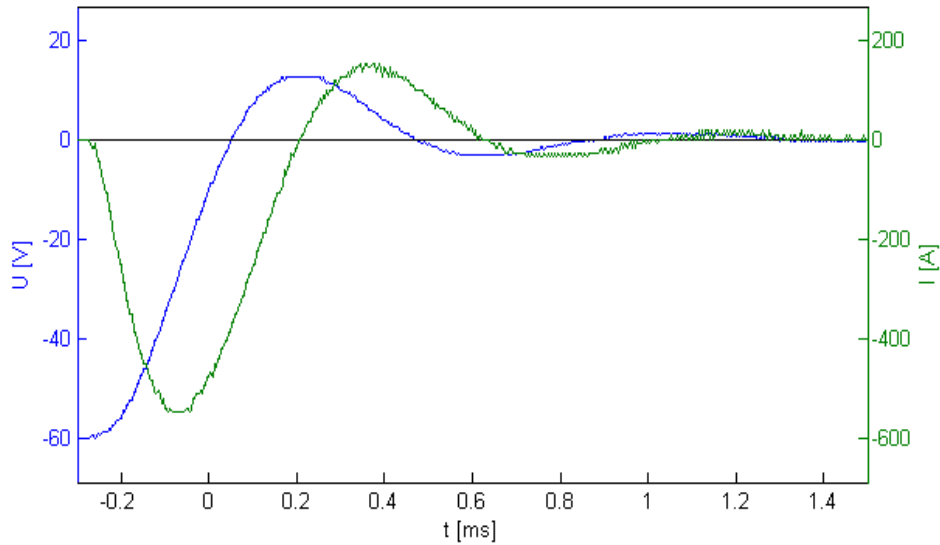


Figure 4.2: Experimental result of the measurement of RLC circuit current and voltage. Voltage (blue) and current (green) vs. time.

value $I_{max} = -530\text{A}$ for $U = -60\text{ V}$ and $I_{max} = -1.32\text{ kA}$ for $U = -150\text{ V}$. Fig. 4.2 shows measured voltage (blue) and current (green) vs. time in RLC circuit with scheme shown in fig. 4.1 for voltage $U = -60\text{ V}$. Current was measured using Rogowski coil. Current amplitude $I_{max} = -550\text{ A}$ for $U = -60\text{ V}$ and $I_{max} = -1.6\text{ kA}$ for $U = -150\text{ V}$. As expected, measured current and voltage evolution in time is similar to the simulated one. In both cases, current and voltage are significantly attenuated after 2 ms. This is due to very poor circuit quality $Q \sim 2$. Circuit quality is so low due to high resistivity of supply cables used in measurement and high resistivity of

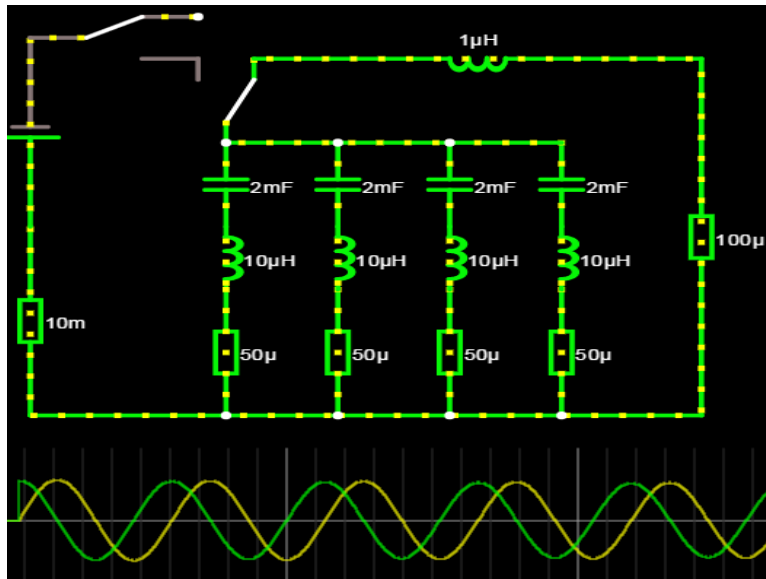


Figure 4.3: RLC circuit of one DEMO divertor cassette simulated using [31]. Voltage (blue) and current (green) vs. time.

the switch used in RLC circuit. Q could be increased either by decreasing total circuit resistivity or increasing coil inductance. In this case, coils inductance is even lower than capacitor inductance.

Fig. 4.3 shows RLC circuit scheme of one DEMO divertor cassette, which is the same as scheme in fig. 4.1, except there are four parallel CASTOR capacitors instead of one. Connecting capacitors in parallel increases their capacitance and decreases inductance by a factor of 4. Coil has inductance $L = 1\ \mu\text{H}$, which is inductance

of one DEMO divertor cassette coil. In this case, power source has voltage 2.5 kV. In case of total circuit resistivity $R = 100 \mu\Omega$, coil has current amplitude $I_{max} = 120$ kA. Coil has voltage amplitude only 700 V, this is because inductance of the coil is lower than inductance of capacitors, where is largest decrease of voltage. This circuit has high quality $Q \sim 220$. Current amplitude is dumped by 25 % after 10 ms.

The measurement of COMPASS twin coil RLC circuit was done in order to check its behavior and compare it with the simulation results. This simulation of DEMO RLC circuit was done in order to show that it is possible to create such an RLC circuit with available capacitors, if we had 2.5 kV switch with resistivity lower than $R \sim 100 \mu\Omega$.

4.2 COMPASS ELM parameters

H-mode on tokamak COMPASS is achieved either in ohmic regime if plasma current exceeds 200 kA at $B_T = 1.2$ T or by heating the plasma by the NBI system. The L–H transition is usually followed by an ELM-free period or Type-III ELMs with frequencies in the range of 400–1500 Hz. Type-I ELMs with frequencies in the range of 80–400 Hz are generated at high plasma currents or in case of NBI-heated plasma. According to multi-machine scaling, an inter-ELM decay length on LFS midplane is in the range of 1.7–2.7 mm.

$$L_{\parallel} \approx 2\pi Rq \quad (4.1)$$

Connection length is given by equation 4.1. For safety factor value $q = 2.5$ at plasma current $I_p = 340$ kA, connection length $L_{\parallel} \approx 8.8$ m. In H-mode, typical pedestal electron temperature $T_e \sim 200$ eV. Using equation 3.1, ELM time has value $\tau_{ELM} \sim 63 \mu\text{s}$. ELM time $\tau_{ELM} \sim 100 \mu\text{s}$ in case of $q_{95} = 3$ and $T_e = 100$ eV.

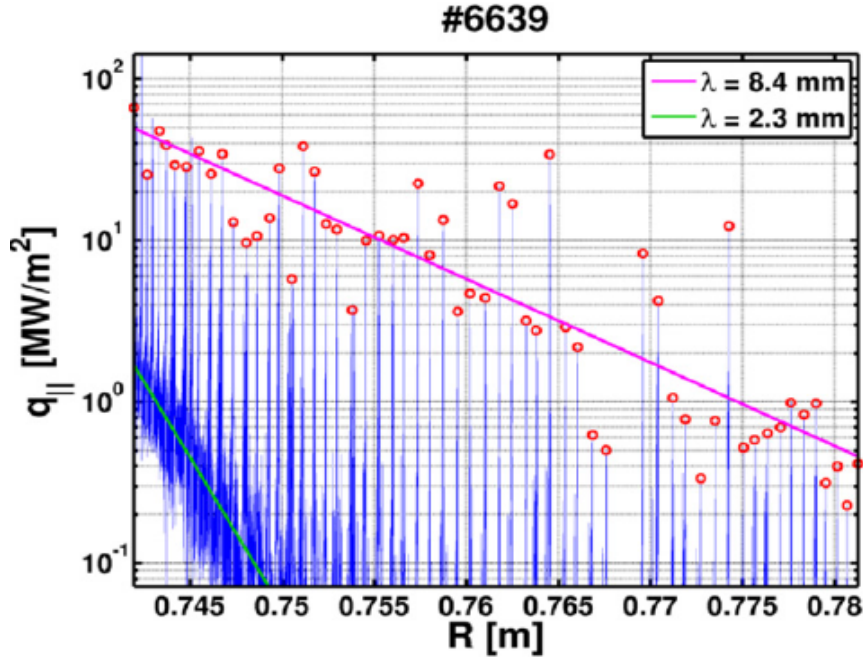


Figure 4.4: Parallel heat flux q_{\parallel} measured by the horizontal reciprocating probe at LFS midplane in shot 6639. Magenta line represents a fit of radial decay length of the peak ELM values, green line shows a fit of the power width in the inter-ELM periods [29].

In shot number 6639, parallel heat flux q_{\parallel} was measured by the horizontal reciprocating probe at the LFS midplane. Fitting measured parallel heat flux q_{\parallel} using exponential decay function 1.4, inter-ELM decay length has value ~ 2.3 mm and ELM decay length has value $\lambda_q \sim 8.4$ mm both on LFS midplane. Both fits with measured data can be seen in fig. 4.4. Magenta line represents a fit of radial decay length and green line shows a fit of inter-ELM decay length. In shot 6639, plasma current during the measurement had value $I_p \sim 280$ kA [29].

4.3 Suppression factor estimation

Using scaling equations for the suppression factor f_{SUP} from section 3.16 and COMPASS ELM parameters from section 4.2 can be estimated f_{SUP} for COMPASS tokamak. The power decay length on LFS midplane $\lambda_q \sim 8.4$ mm for $I_p = 280$ kA. A flux expansion on COMPASS between the LFS midplane and the divertor has value $f_x \sim 6-7$. Therefore the power decay length on the divertor has value $\lambda_q \sim 45$ mm. Suppression factor has positive dependence on the sweeping amplitude λ_S , the sweeping frequency f_{sweep} and the ELM time τ_{ELM} and a negative dependence on the integral power decay length λ_{int} . In order to estimate the maximum possible suppression factor, lets suppose $\tau_{ELM} = 100 \mu s$ and $f_{sweep} = 2$ kHz. According to the equation 1.9 for λ_q scaling, λ_q can be smaller for higher currents. However $\lambda_q = 8.4$ mm was measured at the LFS midplane in the discharge with $I_p = 280$ kA. Plasma current I_p can be only slightly higher than $I_p = 280$ kA in order to preserve an H-mode. As can be seen in equation 1.5, λ_{int} is proportional to the λ_q and is always higher than the λ_q . Minimal possible COMPASS divertor λ_{int} can be then estimated as $\lambda_{int} = 40$ mm. Sweeping amplitude has positive dependence on the machine size. Lets suppose $\lambda_S = 60$ mm as in simulation of DEMO swept divertor despite such a value is unrealistic in the tokamak of COMPASS size. Using these parameters and scaling of f_{SUP} in section 3.16, all four scaling functions yield value of f_{SUP} lower than 1.5. The main reason for such low f_{SUP} is that the natural Type-I ELM decay length is too high and the ELM time τ_{ELM} is low. Type-I ELMs naturally cover nearly all the divertor surface without any mitigation. Real suppression factor would be probably even lower, since this is higher estimate of f_{SUP} . Therefore decreasing the divertor heat flux density significantly by sweeping the strike point on COMPASS tokamak is not realistic. Situation is slightly different on COMPASS-Upgrade, which is discussed in the next chapter. One useful think that could be demonstrated on COMPASS tokamak is the strike point movement.

Chapter 5

Feasibility study of ELM suppression and mitigation on COMPASS-Upgrade divertor targets

COMPASS-Upgrade will be a high magnetic field device ($R_0 = 0.84$ m, $a = 0.28$ m, $I_p = 2$ MA, $B_0 = 5$ T, $n = 10^{20}\text{m}^{-3}$) whose purpose is to enlarge the COMPASS operational space and improve its performance. The start of the operation is planned at the end of 2021. As was discussed in the previous chapter, suppression factor on the COMPASS tokamak is too low for the swept coil concept to have significant results, which can be different on COMPASS-Upgrade. In order to compare results of the strike-point sweeping on DEMO tokamak with the results of the strike-point sweeping on different machine and study feasibility of this concept on smaller tokamak, simulation of the swept strike point on COMPASS-Upgrade tokamak is presented.

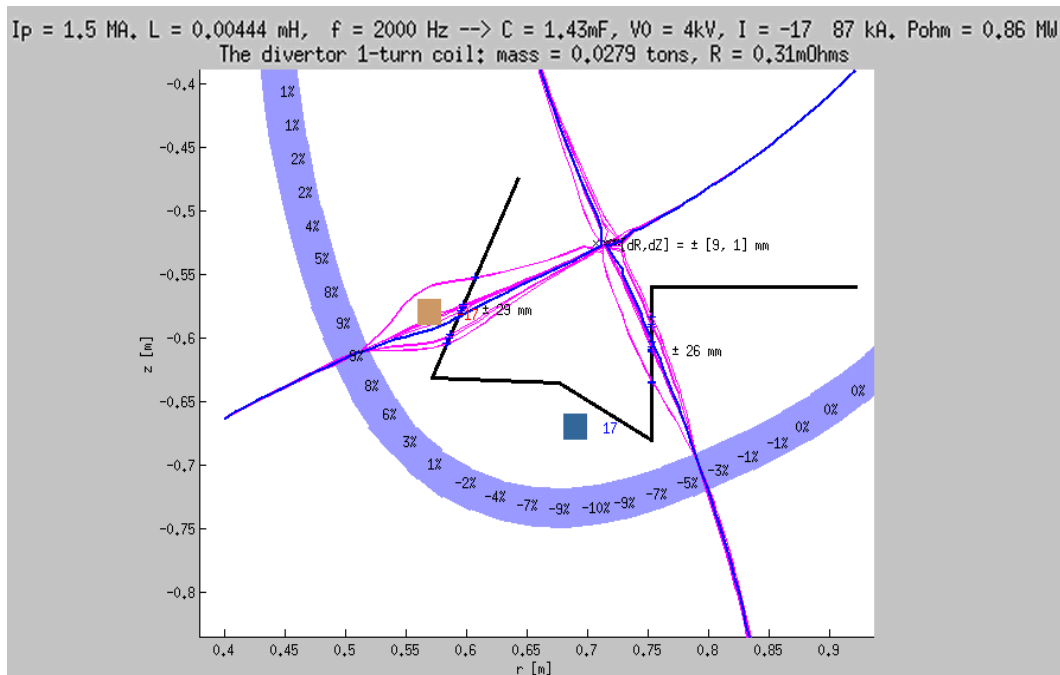


Figure 5.1: Dynamic fiesta simulation of swept strike point of COMPASS-Upgrade divertor including vessel currents.

5.1 Simulation of the strike-point sweeping in COMPASS-Upgrade tokamak

Result of dynamic FIESTA swept strike point simulation is shown in fig. 5.1. The vessel used in the simulation has shape of the COMPASS vessel ($R = 0.56$ m) rescaled for the COMPASS-Upgrade ($R = 0.84$ m). The divertor shown has the shape of the divertor that will be built in the COMPASS-Upgrade. Simulation uses toroidally symmetric twin coil configuration shown in fig. 3.1. Toroidal plasma current $I_p = 1.5$ MA, coil inductance $L = 4.44$ μ H, alternating current frequency $f_{sweep} = 2$ kHz, coil voltage $V_{sweep} = 4$ kV, coil current amplitude $I_{sweep} = 87$ kA are parameters used in simulation. Positions of the divertor sweeping coils turns are on major radius $R = 0.57$ and 0.69 m each, as is shown by two squares in the divertor cassette in fig. 5.1. Coil has square cross section with surface of 2 cm \times 2 cm. One twin coil with given dimensions has mass $m = 28$ kg, coil resistivity $R = 0.31$ m Ω and ohmic losses $P_{ohm} = 0.86$ MW. For maximal discharge length of 5 s, coil would heat up by ~ 300 $^{\circ}$ C. Not only that active cooling of the coil is not necessary, sweeping can be continuous during the discharge. Currents that are generated by the coil in vessel are shown by percents in fig. 5.1. Their

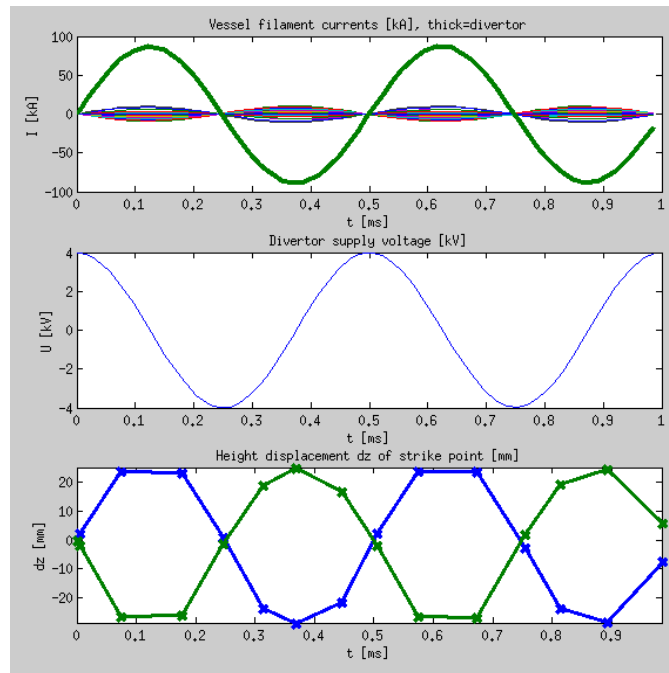


Figure 5.2: Result of the simulation of COMPASS-Upgrade divertor in FIESTA. Top: Twin coil current I_c (green) and vessel filament currents in vs. time t . Middle: Divertor supply voltage V vs. time t . Bottom: Height displacement dz of both strike points vs. time t .

values mean percents of actual current running in divertor coil. Currents generated in the vessel including twin coil current (green) can be seen in upper picture in fig. 5.2. Alternating divertor supply voltage can be seen in middle picture of fig. 5.2. Strike point position varies in time with spatial displacement $[dr, dz] = \pm [9, 1]$ mm. Sweeping amplitude has value $\lambda_S = 29$ mm for inner divertor target and $\lambda_S = 26$ mm for outer target. Periodic height displacement dz of both strike points in mm can be seen in bottom figure 5.2.

5.2 RLC circuit

Simulation of COMPASS-Upgrade swept coils RCL circuit is shown in fig. 5.3. Swept coil has inductance $L \sim 4.4$ μ H and resistivity $R_{\Omega} \sim 0.3$ m Ω . Capacitor used has parameters $C = 2$ mF, $L = 1$ μ H, $R = 50$ $\mu\Omega$, which is similar capacitor as that used in CASTOR, but inductance is 10 times lower. This is the case because if capacitor has capacitance of 10 μ F, voltage drop is too big. In order to obtain sweep current amplitude $I_{sweep} = 87$ kA and voltage amplitude $V_{sweep} = 4$ kV, capacitor with lower inductance would have to be used. In case of $L = 1$ μ H, current and voltage amplitudes in simulation have values $I_{sweep} = 76.5$ kA and $V_{sweep} = 3$ kV. Such parameters pose high requirements on the power source and transistors.

5.3 COMPASS-Upgrade ELM parameters

Using equation 4.1, connection length has value $L_{\parallel} \approx 16$ m for safety factor $q = 3$. Average electron density is expected to have values up to $\langle T_e \rangle \sim 2.5$ keV. This would correspond to pedestal electron temperature up to $T_e \sim 500$ eV. Using equation 3.1, COMPASS-Upgrade ELM time τ_{ELM} would have similar values as COMPASS ELM time $\tau_{ELM} \sim 100 \mu\text{s}$, which is rough estimate. Inter-ELM power decay length on LFS midplane is expected to have values $\lambda_q \sim 1$ mm.

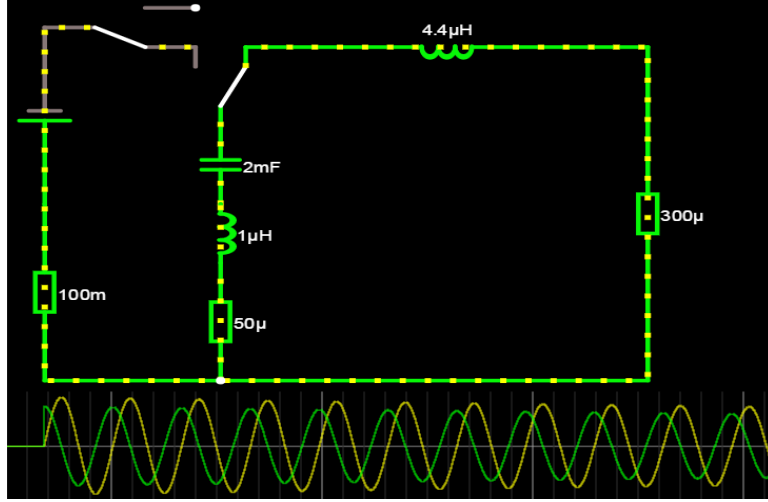


Figure 5.3: COMPASS-Upgrade RLC circuit simulation done using [31]. Voltage (green) and current (yellow) vs. time.

5.4 Suppression factor estimation

Dynamic simulation of the swept strike point of COMPASS-Upgrade divertor has been presented in section 5.1. As can be seen in fig. 5.1, sweep amplitudes has value $\lambda_S = 29/26$ mm for inner/outer target. Sweep frequency has value $f_{sweep} = 2$ kHz. Flux expansion on COMPASS tokamak between LFS midplane and divertor target $f_x \sim 6-7$. Integral power decay length λ_{int} given by equation 1.5 is usually tens of percents higher than λ_q . Since $\lambda_q \sim 1$ mm on LFS midplane, λ_{int} could have values $\lambda_{int} \sim 10$ mm on the divertor. This is only rough estimate, especially since λ_q and λ_{int} depend strongly on poloidal magnetic field, which can vary in different plasma scenarios. Using these parameters and scaling of f_{SUP} in section 3.16, all four scaling functions yield value of f_{SUP} lower than 2. On COMPASS tokamak, the reason for f_{SUP} being too low is mainly that ELMs naturally cover nearly whole divertor surface, as was discussed in section 4.3. This is not the case on COMPASS-Upgrade. However both tokamaks have in common small divertor legs. As can be seen in the simulation result on COMPASS-Upgrade in fig. 5.1, inner targets divertor leg is $\sim 15-20$ cm long and outer targets divertor leg is ~ 10 cm long. In comparison, both divertor legs on DEMO tokamak are more than 1 m long, as can be seen in fig. 3.4. This is the main reason for suppression factor being higher on DEMO ($f_{SUP} \sim 4$) than on COMPASS or COMPASS-Upgrade, where f_{SUP} lower than 2 in both. f_{SUP} depends on the length of the divertor leg, since λ_S depends also on the length of the divertor leg. This leads into the conclusion, that this technique is not feasible for small size machines.

Chapter 6

Alternative concept of ELM suppression and mitigation by toroidally localized fast swept C-shaped coil

In chapter 3, the concept of ELM suppression and mitigation by fast swept magnetic coil on DEMO divertor targets has been introduced and studied. So far, two divertor coil configurations were analyzed. The first one is toroidally symmetric twin coil configuration shown in fig. 3.1. The second one is split coil configuration shown in fig. 3.2. Split coil configuration differs from the twin coil configuration by being split into 54 divertor cassettes, while keeping its toroidal symmetry. Comparing these two configurations, split coil configuration is much more feasible as has been discussed in chapter 3. Due to toroidal symmetry of this concept, it is easier to simulate the swept strike point movement in time using FIESTA code than it would be without the symmetry. Disadvantage is that to confirm performance of the strike point movement experimentally would be too expensive. Alternative concept using only two toroidally localized C-shaped coils in one divertor segment only instead of one coil in each divertor segment is presented. One coil is used for the sweeping of the outer target and one coil for the inner target sweeping. Visualization of such coils in poloidal cut can be seen in fig. 6.1. Advantage of this concept is that it would be much easier to be tested experimentally in comparison with other concepts, since only one divertor segment would need to be rebuilt. Disadvantage is that due to the loss of toroidal symmetry it could have some unforeseen effects and would be hard to be simulated. It is a question if one coil could generate magnetic field strong enough to replace 54 divertor coils and if the effect on strike point would be the same. Following sections analyses suppression factor, dimensions and other parameters of such coil for DEMO.

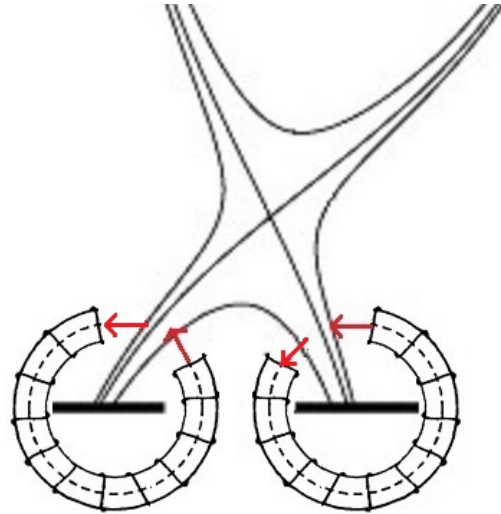


Figure 6.1: Two toroidally localized C-shaped coils in poloidal cut, one for each divertor target leg. Red arrows shows its magnetic field.

6.1 DEMO C-coil suppression factor estimation

In order to compare two different sweeping concepts, it is reasonable to compare parameters of both concepts for the same suppression factor f_{SUP} . In twin coil and split coil configurations, $f_{SUP} = 4$ for sweeping amplitude $\lambda_S = 64$ mm and sweeping frequency $f_{sweep} = 2$ kHz. We do not have simulation of toroidally localized coil concept. Although we can estimate the suppression factor from coil parameters. If C-coils magnetic field has the same magnitude as toroidal magnetic field in the divertor and they are perpendicular to each other, sweeping amplitude λ_S could be equal to coil minor diameter. This could be the case if following assumption

is valid. Toroidal magnetic field lines would be curved by 45° in front of the C-coil, since its magnetic field is perpendicular to the toroidal magnetic field. Particles would be then shifted perpendicularly to their original direction. The length of the shift is given by the length of the coil minor diameter. If this assumption is valid, it sets the condition on C-coil magnetic field strength to be ideally $B_c = 6$ T on the spot where it crosses divertor leg. C-coils magnetic field decreases with the distance from the coil rapidly, therefore B_c should be probably higher inside the coil in order to obtain $B_c = 6$ T on the spot of the intersection with the divertor leg. The longer is the length of the intersection, the higher is the suppression factor f_{SUP} . Optimal direction of the magnetic field is perpendicular to the magnetic field of the divertor leg.

6.2 DEMO C-coil parameters

In order to keep the circuit in resonance with sweeping frequency $f_{sweep} = 2$ kHz, it is best to keep coils inductance at value $L_c = 54 \mu\text{H}$, which is the same as in split coil configuration. Coil material is copper. Since this parameters are set, in order to achieve the same coil inductance, coil dimensions need to be chosen properly. Needed coil current amplitude is given by coil magnetic field strength at the intersection with the divertor leg. Coil dimensions will determine impedance and ohmic losses. Toroidal coil inductance can be calculated using equation 6.1. μ_0 is vacuum permeability, N_c is number of turns, A_c is cross section of the coil, l_c is coils circumference (in case of solenoid, l_c is coils length) and R_c is coils major radius. Solenoid and toroid have almost the same inductance if solenoids length is equal to toroids circumference.

$$L_c \approx \frac{\mu_0 N_c^2 A_c}{l_c} \approx \frac{\mu_0 N_c^2 A_c}{2\pi R_c} \quad (6.1)$$

Basic parameters of the toroidal coil can be seen in fig. 6.2. Core inside the coil is shown just for an illustration. For coil dimensions chosen as following: major radius $R_c = 1$ m, minor radius $r_c = 3.3$ cm and number of coil turns $N_c = 280$, toroidal coil has inductance $L_c = 54 \mu\text{H}$. Alternating current running through such coil would have current amplitude $I_c = 107$ kA and voltage amplitude $U_c = 72$ kV. Coils ohmic resistivity $R_\Omega = 2.1$ m Ω . For alternating current with frequency of $f_{sweep} = 2$ kHz, skin depth is only $\delta = 1.5$ mm. In order to maximize coils effective cross section, which is part of the cross section A_c conducting alternating current with $f_{sweep} = 2$ kHz, litz wire is used. Thickness d_c is set to be 80% of the distance between two turns D_c . Ohmic power has value $P_c = 1.8$ MW. Such a coil would weight 132 kg and without active cooling would heat up by 170 K after 60 s discharge with 4 ms long sweeps and 50 ms waiting time between each sweep. Using equation 3.7, total energy in such a circuit would have value $E_{total} = 309$ kJ, which is $\sim 30\%$ less than total energy stored in twin coil or split coil configurations. Capacitor in such a circuit would have capacitance $C_c = 118 \mu\text{F}$.

In order to use toroidal coil for sweeping, 20–40 % of the coil needs to be cut out yielding into C-shaped coil. By cutting part of the coil, coils inductance would drop. Such a drop of inductance can be compensated by increasing the number of coil turns. Coil angle ϕ_c [°] given by equation 6.2 characterizes shape of the coil. α [°] is part of the coil which is cut out.

$$\phi_c = 360^\circ - \alpha \quad (6.2)$$

Electrical circuit with parameters described above would have quality $Q_c = 172$. After 4 ms of sweeping, current amplitude would be dumped by $A_{dump}(4ms) = 25\%$, which is still acceptable.

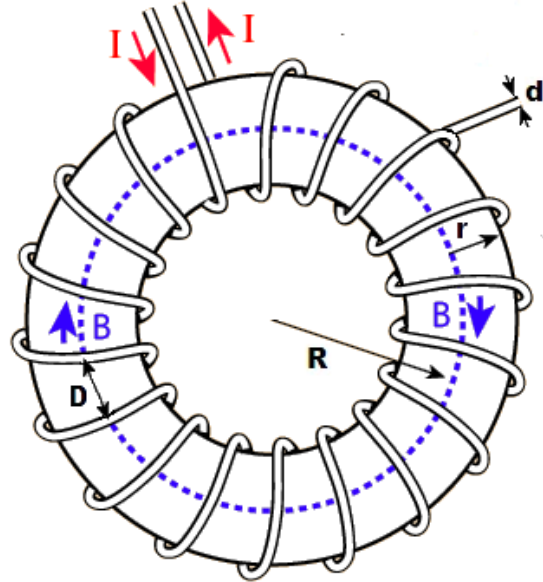


Figure 6.2: Toroidal coil, major radius R_c , minor radius r_c , distance between two turns D_c , coil thickness d_c are shown by black arrows. Magnetic field of the coil is shown by blue arrows and coil current by red arrows.

6.2.1 Optimizing DEMO C-coil parameters

Parameters of DEMO C-coils electrical circuit described in previous section 6.2 are $I_c = 107$ kA and $U_c = 72$ kV. These are quite unrealistic requirements for the power source. The same problem with too high voltage was analyzed in section 3.3. It was the main reason to use split coil configuration instead of twin coil configuration, since voltage applied to each divertor segment coil is $1/4$ of voltage used in twin coil configuration while keeping the same coil current. In C-coil configuration, we suppose that suppression factor f_{SUP} is the same for one pair of coils with $B_c = 6$ T as for N_p pairs of coils with $B_c = 6/N_p$ T each. This assumption can be used to avoid high voltages by using multiple pairs of toroidally localized C-shaped coils with lower magnetic field B_c instead of one with $B_c = 6$ T.

Dependence of the number of DEMO C-coil pairs N_p on each C-coils voltage U_c , current I_c , magnetic field B_c and ohmic power P_c can be seen in table 6.1. Each coil has inductance $L_c = 84$ μ H, resistivity $R_\Omega = 4$ m Ω ,

N_p	U_c [kV]	I_c [kA]	B_c [T]	P_c [kW]
1	72	68.5	6	731
2	36	34.2	3	183
3	24	22.8	2	81
4	18	17.1	1.5	46
5	14.4	13.7	1.2	29

Table 6.1: Number of pairs of toroidally localized DEMO C-shaped coils N_p . Voltage and current amplitudes U_c and I_c , magnetic field B_c and ohmic losses P_c for each C-coil.

mass $m_c = 133$ kg, major radius $R_c = 1$ m, minor radius $r_c = 3.3$ cm and coil angle $\phi_c = 230^\circ$. Number of coil turns $N_c = 280$ and their thickness $d_c = 1.5$ cm. Capacity of capacitor in each coils circuit $C_c = 75$ μ F, circuit quality $Q_c = 270$ and amplitude dump after 4 ms of sweeping $A_{dump}(4\text{ms}) = 17$ %.

One way how to improve DEMO C-coil configuration is to lower the major radius while keeping other dimensions constant. Parameters of C-coil with major radius $R_c = 0.5$ m, minor radius $r_c = 3.3$ cm, number of turns $N_c = 280$ and coil thickness $d_c = 1$ cm are shown in table 6.2. Each coil has inductance $L_c = 168$

N_p	U_c [kV]	I_c [kA]	B_c [T]	P_c [kW]
1	72	34.2	6	590
2	36	17.1	3	147
3	24	11.4	2	65
4	18	8.6	1.5	37
5	14.4	6.8	1.2	24

Table 6.2: Number of pairs of toroidally localized DEMO C-shaped coils N_p . Voltage and current amplitudes U_c and I_c , magnetic field B_c and ohmic losses P_c for each C-coil.

μ H, resistivity $R_\Omega = 12.6$ m Ω , mass $m_c = 41$ kg and coil angle $\phi_c = 230^\circ$. Capacity of capacitor in each coils circuit $C_c = 38$ μ F, circuit quality $Q = 168$ and amplitude dump after 4 ms of sweeping $A_{dump}(4\text{ ms}) = 26$ %. Configuration with $R_c = 0.5$ m has ~ 2 times higher inductance than configuration with $R_c = 1$ m. Coil current, mass and capacitance are lower. Circuit quality is lower.

As can be seen in table 6.2, even in case of number of DEMO C-coil pairs $N_p = 5$, coil voltage is still high. This could be avoided by increasing N_p even higher, but then more divertor segments would have to be rebuild. In order to achieve coil voltage and current $U_c = 14.4$ kV and $I_c = 6.8$ kA, two parallel rows each consisting of ten IGBT transistors connected in series would have to be used. One IGBT transistor has maximum current $I_{max} = 3.6$ kA at voltage $V_{max} = 1.5$ kV.

C-coils with parameters described above seem to be feasible. Upper estimate for the suppression factor of such coils is $f_{SUP} = 4$. The problem is that this would be the case only if the assumption in section 6.1 is valid and also if the assumption that suppression factor f_{SUP} is the same for one pair of coils with $B_c = 6$ T as for N_p pairs of coils with $B_c = 6/N_p$ T each is valid. According to magnetic field lines tracking on COMPASS in subsection 6.3.2, it looks like using C-coil with comparable magnetic field amplitude as toroidal magnetic field at the magnetic axis (1 T on COMPASS) leads to similar suppression factor as would be achieved using twin coil configuration. This suggests that estimates about C-coil suppression factor could be all right. In order to test these estimates, magnetic field lines tracking for DEMO is needed.

6.3 Magnetic field lines tracking on COMPASS tokamak

DEMO divertor C-shaped coils with parameters described in previous section are feasible. The main question is how large would be the suppression factor if such coils were used. Their usage could lead into some unforeseen effects. One way to get some insight into the effect of the C-coil on the strike point is the tracking of magnetic field lines from the LFS midplane to the divertor. This is done for COMPASS tokamak in this section.

6.3.1 C-coils magnetic field

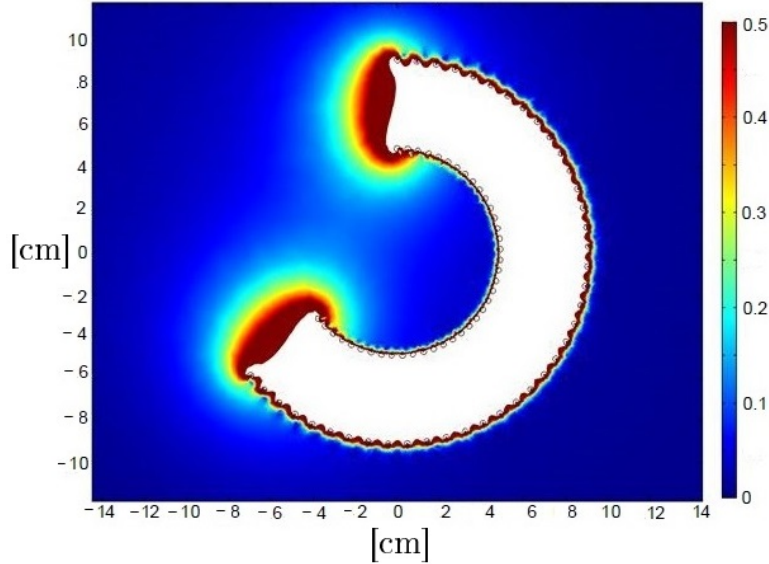


Figure 6.3: Contour plot [cm] of the magnetic field [T] of 230° COMPASS C-coil with major radius $R_c = 7$ cm, minor radius $r_c = 2$ cm, number of turns $N_c = 100$, inductance $L_c = 39 \mu\text{H}$, voltage $V_c = 240$ V and current $I_c = 4$ kA calculated in COMSOL Multiphysics.

Magnetic field of COMPASS C-coil with major radius $R_c = 7$ cm, minor radius $r_c = 2$ cm, number of turns $N_c = 100$, inductance $L_c = 39 \mu\text{H}$, voltage $V_c = 240$ V and current $I_c = 4$ kA can be seen in fig. 6.3. It can be seen that magnetic field is rapidly decreasing outside the coil. This was computed in COMSOL Multiphysics. Output of the simulation is 3D matrix of C-coils magnetic field, which is used for the interaction of magnetic field lines with C-coils magnetic field in the following section.

6.3.2 Magnetic field lines tracking

3D visualization of COMPASS C-coil, its magnetic field and multiple magnetic field lines running from the LFS midplane to the divertor are shown in fig. 6.5. All calculations in this section are done for COMPASS tokamak. The same as in fig. 6.5 is shown in poloidal cut in fig. 6.4. Field lines with the same color lead from the same radial position on the LFS midplane, but each has different toroidal position. This is the case for all figures in this section. Dark blue shows separatrix position. It can be seen, that some magnetic field lines are curved by C-coils magnetic field, some are not. Those magnetic field lines, which are far from the separatrix miss the C-coil vicinity because of high poloidal magnetic field.

Dependence of the resulting shift on the divertor target on the non-perturbed divertor target position is shown in fig. 6.6. Coil with parameters described in 6.3.1 shifts magnetic field lines 5–15 mm near the strike point and 0–15 away (20–80 mm) from the strike point. Some magnetic field lines are not shifted as can be seen in fig. 6.4 and 6.6. Dependence of the toroidal angle on the divertor target position is shown in fig. 6.7. From 6.7 it can be seen that the shift is not toroidally equally distributed. In order to avoid this, multiple C-coils would have to be used to equally distribute the shift of magnetic field lines in the toroidal direction. Such shift is comparable with the sweeping amplitude, which could be achieved on COMPASS. Despite the fact that it would lead into small suppression factor as was discussed in section 4.3, it could be enough for the demonstration of the strike point movement. Design of C-coil for COMPASS tokamak is described in the following section.

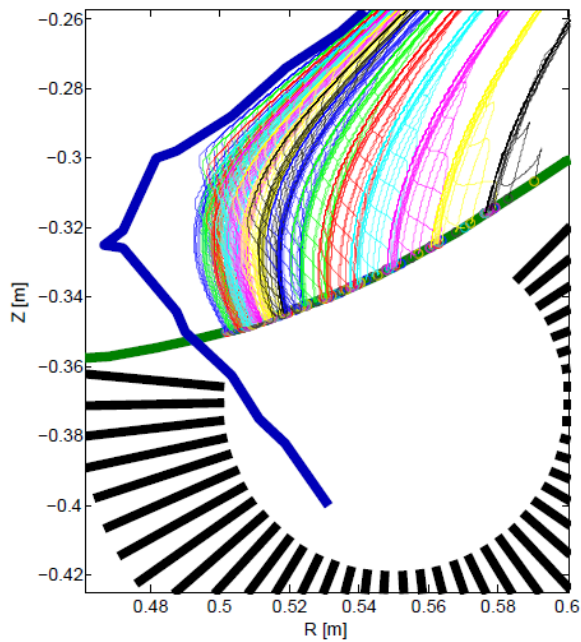


Figure 6.4: C-coil, magnetic field lines ending on the divertor and separatrix (dark blue) in poloidal cut calculated in MATLAB. Field lines with the same color lead from the same radial position on LFS midplane, but each has different toroidal position.

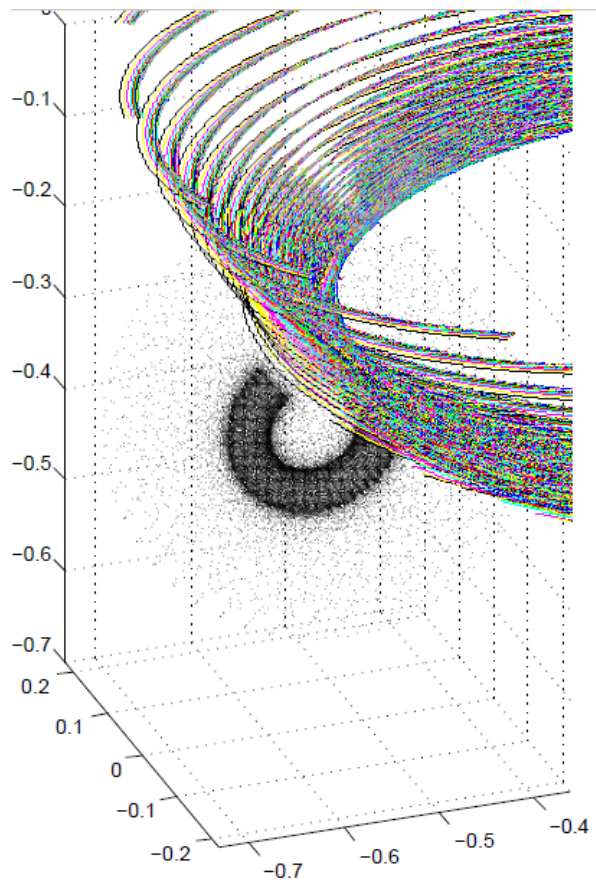


Figure 6.5: 3D visualization of the C-coil, its magnetic field and magnetic field lines running from LFS midplane to the divertor calculated in MATLAB.

6.4 Design of C-shaped swept magnetic coil on COMPASS tokamak

As was discussed in the sections 4.3 and 5.4, suppression factor in small size tokamaks is too low ($f_{SUP} < 1.5$). Therefore the whole concept of the strike point sweeping on COMPASS or COMPASS-Upgrade tokamaks is not feasible. However the demonstration of the strike point movement is important for feasibility of this concept for larger size machines. This section describes a technical design of the C-shaped coil dedicated for the strike point sweeping on COMPASS tokamak.

One C-shaped coil would sweep only the outer target. One divertor segment would have to be rebuilt in order to make space for the coil. Fig. 6.8 shows RLC resonant circuit of one C-shaped coil. One of the most limiting features of this concept is switch, which can switch only voltages up to 200 V. Such a switch could be made of ~ 200 transistors, which are available now on COMPASS tokamak. It could have resistivity $R_{\Omega} \sim 4$ m Ω . In order to obtain such a low voltage, sweeping frequency was set to $f_{sweep} = 200$ Hz. The sweeping would be too slow for ELM mitigation, but since only the demonstration of the strike point movement is important in this concept, $f_{sweep} = 200$ Hz is enough. In order to decrease resonant frequency to 200 Hz, 8 CASTOR capacitors with $C = 2$ mF each need to be connected in parallel leading into overall circuit capacity $C = 16$ mF. Advantage is also that parallel capacitor connection decreases total capacitor inductance, which has value $C \sim 1.2$ μ H, since one capacitor has inductance $L = 10$ μ H. Coils inductance also need to be set as high as possible. Coil showed in 6.8 has inductance $L = 62$ μ H and resistivity $R_{\Omega} = 18$ m Ω . Obtaining higher inductance is not possible in our configuration, since space for the coil is limited. C-shaped copper coil with such inductance would have major radius $R = 7$ cm, minor radius $r = 2.1$ cm, thickness $d = 0.4$ cm and $N = 100$ turns. Such a coil would weight 3 kg. Coil would probably have to be wound around some horseshoe-shaped structure. In case of current amplitude $I = 2.5$ kA, magnetic field $B = 1.1$ T would be generated inside the C-coil.

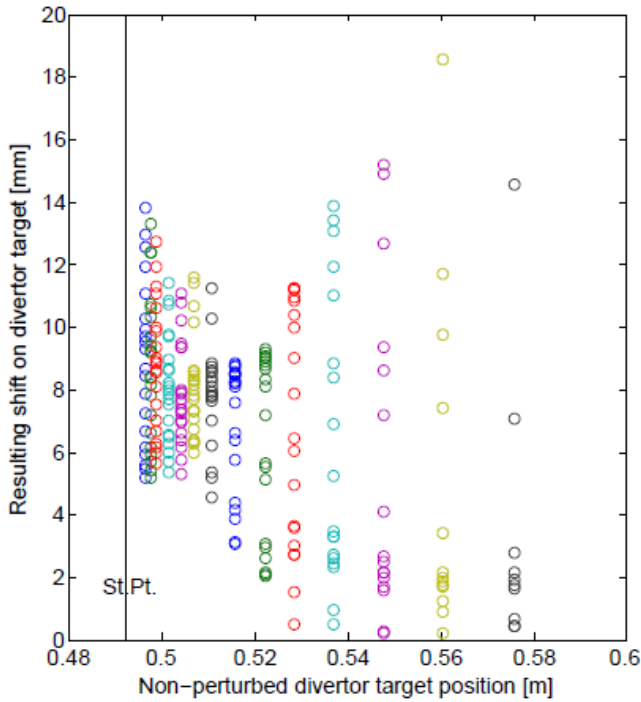


Figure 6.6: Dependence of the the resulting shift on the divertor target [mm] on the non-perturbed divertor target position [m] calculated in MATLAB. Separatrix position is shown by black vertical line.

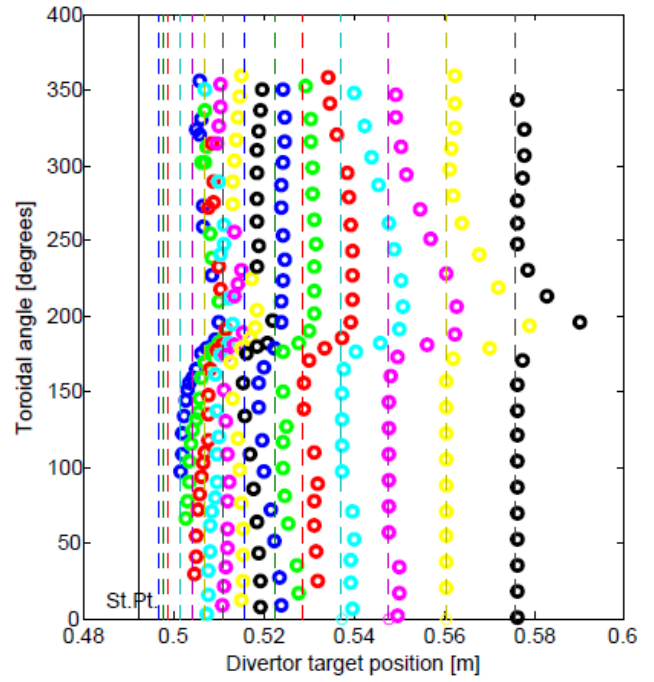


Figure 6.7: Dependence of the toroidal angle [°] on the divertor target position [m] calculated in MATLAB. Original position of each line is depicted by the dashed line with the same color. Separatrix position is shown by black vertical line.

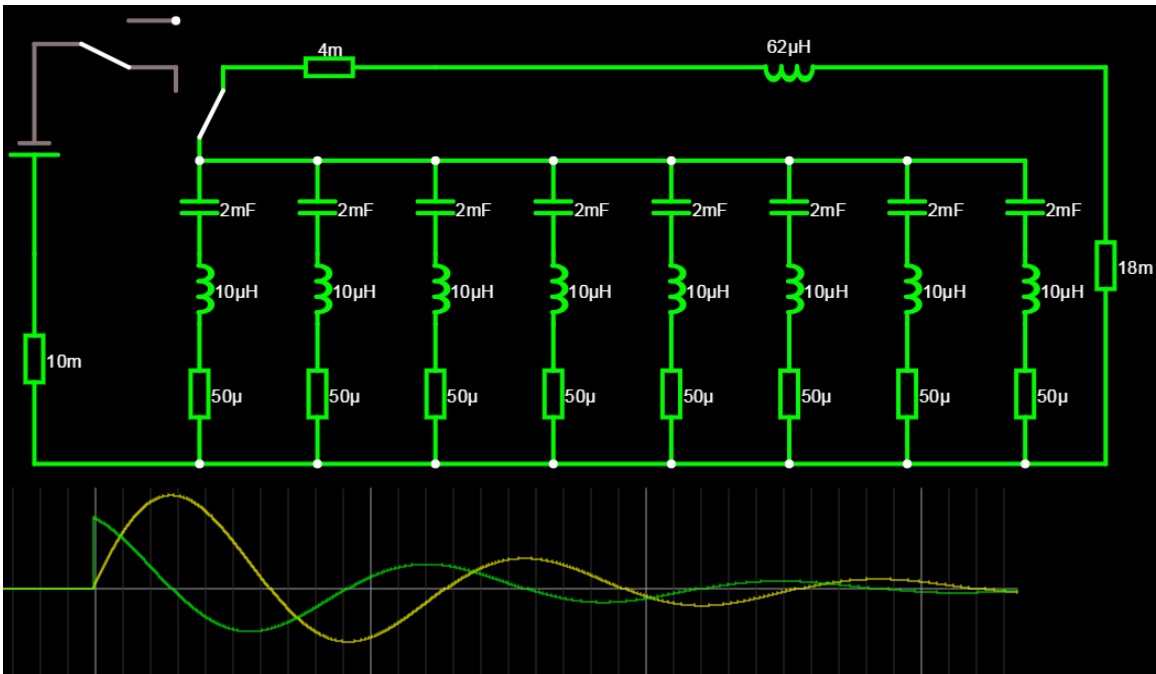


Figure 6.8: RLC circuit of COMPASS C-coil simulated in [31]. Voltage (blue) with amplitude $V_{sweep} = 196$ V and current (green) with amplitude $I_{sweep} = 2.5$ kA vs. time.

According to simulation in fig. 6.8, voltage amplitude $V_{sweep} = 196$ V and current amplitude $I_{sweep} = 2.5$ kA are parameters in such circuit. Coil would heat up negligibly during 1 ms discharge. Coils inductance is calculated using equation 6.1. Inductance of the coil with the same parameters calculated in COMSOL

Multiphysics has value $L \sim 39 \mu\text{H}$. Inductance of similar 40 cm long solenoid with major radius $R = 7$ cm, minor radius $r = 2.1$ cm, thickness $d = 0.55$ cm and 87 turns measured using multimeter has value $L \sim 34 \mu\text{H}$. Inductance of the same 40 cm solenoid calculated using equation 6.1 has value $L \sim 33 \mu\text{H}$. Therefore it seems that equation 6.1 is accurate. Problem of circuit shown in fig. 6.8 is poor circuit quality $Q = 6$. Amplitude dump after 1 ms $A_{dump}(1 \text{ ms}) = 25 \%$ and $A_{dump}(10 \text{ ms}) = 94 \%$. The main reason for such a low circuit quality is maximum switch voltage limit and coils inductance. However in order to demonstrate strike point movement, circuit quality could still be enough.

The concept of COMPASS C-coil with parameters described above seems to be feasible. According to magnetic field lines tracking, it should be possible to observe the strike point movement using such coil on COMPASS tokamak.

Conclusion

In order to avoid metal surface melting of divertor targets of big tokamak fusion reactors by localized ELM heat loads, a new technique of spreading the heat flux was studied. Suppression of the heat flux is done by fast harmonic divertor strike point sweeping using 54 copper coils, one in each divertor segment. Each coil has rectangular shape with 100 kg of mass and 29 kW of ohmic power. Results of 2D dynamic heat conduction simulation of DEMO divertor targets in MATLAB are presented. The simulation uses real infra-red data of large ELM heat fluxes on JET divertor target, rescaled for EU DEMO reactor ($B = 6$ T, $I_p = 21$ MA, $R = 9$ m). In order to obtain the surface temperature suppression factor $f_{SUP} = 4$, sweeping with amplitude \times frequency = 7 cm \times 2 kHz is needed. Sweeping frequency of 2 kHz is chosen in order to mitigate each single ELM. Sweeping would be triggered by analog divertor heat flux signal detected by Langmuir probes. Dynamic FIESTA simulation of the strike point sweeping on DEMO divertor targets is presented. The simulation scenario requires 54 capacitive energy storages with capacitance 7.5 mF charged at 1.5 kV in each Coils RLC circuit. Each RLC circuit requires AC current with 130 kA amplitude for each ELM event for 4 ms of sweeping, with waiting time 50 ms at the ELM frequency of 20 Hz. The $I \times B_t$ forces would yield into coil vibrations along coils radial axis with amplitude ~ 1 mm at the same ELM frequency. Coils are partially shielded from large neutron flow suffering a few DPA per full power year. Dynamic FIESTA simulation of the strike point sweeping on COMPASS-Upgrade is presented. Based on this result and the scaling of suppression factor for tokamak COMPASS and COMPASS-Upgrade, this technique seems to be feasible for big tokamaks only, since suppression factor on small size tokamaks $f_{SUP} < 2$. An alternative technique for the strike point sweeping is also presented. This technique uses one pair (instead of 54) of C-shaped coils, each for one strike point, therefore it is simpler from an engineering point of view. This technique could be adopted on COMPASS tokamak. In order to see the effect of the strike point movement, which should be possible according to magnetic field lines tracking, design of the C-shaped swept coil for COMPASS tokamak is presented.

Bibliography

- [1] K. Kamiya et al., *Edge localized modes: recent experimental findings and related issues*, Plasma Physics and Controlled Fusion, vol. 49 (2007) S43–S62.
- [2] Evans, T.E. *ELM mitigation techniques*, Journal of Nuclear Materials, vol. 438 (2013) S11–S18.
- [3] E. Bertolini, *Impact of JET experimental results and engineering development on the definition of the ITER design concept*, Fusion Engineering and Design, vol. 27 (1995) 27–38.
- [4] R. Albanese, *implementation and test of the XSC extreme shape controller in JET*, Fusion Engineering and Design, vol. 74 (2005) 627–632.
- [5] G. Ambrosino et al. *Plasma strike-point sweeping on JET tokamak with the extremeshape controller*, IEEE Trans. Plasma Sci., vol. 36 (2008) 834–840.
- [6] Muyuan Li, Francesco Maviglia, Gianfranco Federici, Jeong-Ha You, *Sweeping heat flux loads on divertor targets: Thermal benefits and structural impacts*, Fusion Engineering and Design, vol. 102 (2016) 50–58.
- [7] T. Eich et al., *Scaling of the tokamak near the scrape-off layer H-mode power width and implications for ITER*, Nuclear Fusion, vol. 53 (2013) 093031.
- [8] G. Federici et al., Plasma Physics and Controlled Fusion, vol. 45 (2003) 1523.
- [9] A. Zhitlukhin et al., Journal of Nuclear Materials, vol. 363–365 (2007) 301.
- [10] N. Klimov et al., Journal of Nuclear Materials, vol. 390–391 (2009) 721.
- [11] A. Loarte, et al., Proc. 24th IAEA Fusion Energy Conference (San Diego, 2012) ITR/1-2.
- [12] P.T. Lang et al., Nuclear Fusion, vol. 43 (2003) 1110.
- [13] A. Herrmann et al., Plasma Physics and Controlled Fusion, vol. 44 (2002) 883.
- [14] P.T. Lang et al., Nuclear Fusion, vol. 45 (2005) 502.
- [15] L.R. Baylor, et al., Proc. 37th EPS Conference on Plasma Physics (Dublin) (2010) P2.117.
- [16] P.T. Lang et al., Nuclear Fusion, vol. 51 (2011) 033010.
- [17] G.T.A. Huysmans, in: Proc. 37th EPS Conference on Plasma Physics Dublin, 2010, p. P4.132.
- [18] D.H. McNeill et al., Physical Fluids B 3 (1991) 1994.
- [19] T.E. Evans et al., Nature Physics, vol. 2 (2006) 419.
- [20] E.N. Sieder, G.E. Tate, *Heat transfer and pressure drop of liquids in tubes*, Ind. Eng. Chem., vol. 28 (1936) 1429–1435.
- [21] J. Thom, W. Walker, T. Fallon, G. Reising, *Boiling in sub-cooled water during flow up heated tubes or annuli*, in: Proceedings of the Institution of Mechanical Engineers (London), vol. 180(Pt. 3C), 1965–66, pp. 226–246.
- [22] A. Scarabosio, T. Eich, A. Herrmann, B. Sieglin, the ASDEX Upgrade Team and JET-EFDA contributors, *Outer target heat fluxes and power decay length scaling in L-mode plasmas at JET and AUG*, Journal of Nuclear Materials, vol. 438 (2013) S426–S430.

- [23] J. Adamek et al., *Fast measurements of parallel heat flux and the power decay length in ELMy H-mode on the COMPASS tokamak*, 22nd International conference on plasma surface interactions in controlled fusion devices, May 30 - June 3, 2016, Rome.
- [24] Zohm H., *Plasma Physics and Controlled Fusion*, vol. (1996) 38 105.
- [25] J.H. You et al., *Progress in the initial design activities for the European DEMO divertor: Subproject 'Cassette'*, Fusion engineering and design, (2016).
- [26] T. Eich et al., *Inter-ELM Power Decay Length for JET and ASDEX Upgrade: Measurement and Comparison with Heuristic Drift-Based Model*, Physical Review Letters, vol. 107 215001 (2011).
- [27] T. Eich et al., *On the asymmetries of ELM divertor power deposition in JET and ASDEX Upgrade*, Journal of Nuclear Materials, vol. 390–391 (2009) 760–763.
- [28] B.E. Fridman et al., *Energy Storage Capacitor Cell with Semiconductor Switches*, 1-4244-0914-4/2007 IEEE.
- [29] R. Panek et al., *Status of the COMPASS tokamak and the characterization of the first H-mode*, Plasma Physics Controlled Fusion, vol. 58 (2016) 014015 (9pp).
- [30] T. Eich et al., *ELM divertor heat load scaling to ITER with data from JET, MAST and ASDEX Upgrade*, Nuclear Materials and Energy, 2017, DOI: 10.1016/j.nme.2017.04.014
- [31] *Analog Circuit Simulator Applet*, <http://www.falstad.com/circuit>, April 2017.
- [32] V. Thompson et al., *Analysis and design of the beryllium tiles for the JET ITER-like wall project*, Fusion Engineering and Design, vol. 82 (2007) 1706–1712.
- [33] Yu. Igitkhanov, B. Bazylev, R. Fetzler, *The quantification of the key physics parameters for the DEMO fusion power reactor and analysis of the reactor relevant physics issues*, DOI: 10.5445/KSP/1000038935.
- [34] G. Cunningham, Fiesta manual